IDEA League

Master of Science in Applied Geophysics

Research Thesis

Rescaling of incorrect source strength using Marchenko Redatuming

Using the Marchenko equation to determine correction factors

Joeri Brackenhoff

August 19, 2016

Rescaling of incorrect source strength using Marchenko Redatuming

Using the Marchenko equation to determine correction factors

Master of Science Thesis

for the degree of Master of Science in Applied Geophysics at
Delft University of Technology
by

Joeri Brackenhoff

August 19, 2016

Department of Geoscience & Engineering · Delft University of Technology

Delft University of Technology

Delft University of Technology

Printed in The Netherlands

IDEA LEAGUE
JOINT MASTER'S IN APPLIED GEOPHYSICS

Delft University of Technology, The Netherlands
ETH Zürich, Switzerland
RWTH Aachen, Germany

Dated: *August 19, 2016*

Supervisors:

Dr. Ir. J.R. van der Neut

Prof. Dr. Ir. C.P.A. Wapenaar

Committee Members:

Dr. Ir. J.R. van der Neut

Prof. Dr. Ir. C.P.A. Wapenaar

Dr. Ir. J.W. Thorbecke

Prof. Dr. F. Wellmann

Abstract

The iterative Marchenko scheme is a recent development in the field of Geophysics and a way to retrieve Green's functions at any point in the subsurface, called a focal point. To achieve this, only the reflection response measured at the Earth's surface and an estimation of the first arrival at the focal point are required. If the amplitude of the reflection response is scaled incorrectly, the method will suffer from artifacts in the estimation of the Green's function. The amplitudes of the reflection response are unknown when the source strength of the recording is unknown. To correct for source strength, a correction factor is used. The correction factor can be retrieved by using a function that has its minimum at the required correction factor, a so-called cost function. Additionally a scaling factor can be determined, which is used to ensure that the final Green's function has the correct amplitudes. Three cost functions are proposed. The first cost function minimizes the upgoing Green's function and only works if no reflectors are present below the focal point. The second cost function minimizes the reflection of a truncated medium that has no reflectors above the focal point. The second cost function can handle a focal point with reflectors below it. However, it is very computationally expensive, especially in 2D and 3D. Therefore the third cost function is introduced. The third cost function is more efficient than the second one and is based on the minimization of the upgoing Green's function, with a source and receiver at the focal point. It is less accurate, retrieving only very close approximations of the required correction factor in case reflectors are present below the focal point. The minimization of the cost functions fails if there is an overlap in time of physical events and artifacts. In case physical events overlap with each other, none of the cost functions works perfectly.

Acknowledgements

First and foremost, I would like to thank my supervisors Joost van der Neut and Kees Wapenaar. You have both been very supportive of my work and were helpful whenever I was stuck. Without your help my thesis would not have been realized and I thank you dearly. I also owe many thanks to Jan Thorbecke, who not only allowed me to use his code, but was also prepared to help me when I decided to add my own extension. In the same way I am thankful to Kees Weemstra, Deyan Draganov, Richard Bakker and Sian Jones, who allowed me to work in their workspace and with all of whom I had many intelligent and stimulating conversations. I want to thank Myrna Staring whose research overlapped with mine and along with the Marchenko group in our section stimulated the conversation in the research group about the Marchenko method. Aside from Myrna, I would like to thank all the PHD students from the section Applied Geophysics and Petrophysics at the TU Delft. They made me feel very welcome and I had many interesting lunch breaks together with them, especially with Max Holicki. Going a bit further back I would again like to thank Guy Drijkoningen and Andreas Schaller, who were the supervisors on my Bachelor Thesis. They guided me through me first foray into Geophysics and made me realize that this is where my passion lies. And finally I would like to thank my family and friends, who were very supportive of my work and ambitions. But I am also grateful that they reminded me that it is a good idea to kick back and relax once in a while. And I like to especially thank my mother, who has been there for me throughout my entire life and helped me make a lot of important decisions. I sincerely hope she is proud of what I have achieved.
And I am also grateful to you, whoever is reading this. Even if this is the only part of my thesis that you are reading, I want you to know that I put a lot of time and effort in this thesis and I am very proud of it. But I am also proud that there were so many great people prepared to help me with my research. Writing this thesis was truly a fulfilling experience.

Delft University of Technology
August 19, 2016

Joeri Brackenhoff

Table of Contents

Abstract vii

Acknowledgements ix

Nomenclature xxi

1 Introduction 1

2 Theory 5

2-1 Marchenko scheme . . . 8
2-2 Construction of Green's functions . . . 15
2-3 Correction factor in 1D . . . 21
2-3-1 Scaling of first arrival . . . 23
2-3-2 Scaling with single-sided redatuming . . . 26
2-3-3 Scaling with double-sided redatuming . . . 27
2-3-4 Alternative scaling with double-sided redatuming . . . 29
2-4 Correction factor in 2D/3D . . . 32
2-4-1 Scaling the first arrival . . . 32
2-4-2 Cost functions . . . 33

3 Cost function results in 1D 35

3-1 Scaling of the first arrival . . . 35
3-2 Single-sided redatuming cost function . . . 38
3-3 Double-sided redatuming cost function . . . 45
3-4 Alternative double-sided redatuming cost function . . . 48

4 Conclusion and Discussion 59

Bibliography 61

A Models 63

List of Figures

1-1 Green's function retrieved at a focal depth of 2000 meter for a simple model using a source strength that was (a) unscaled, (b) scaled with a factor of 1.5 and (c) scaled with a factor of 2.0. First arrivals are indicated in red and artifacts due to incorrect scaling are indicated in green 2

2-1 Visual clarification of Green's function and the two type of focusing functions. (a) Green's function $G(\mathbf{x}, \mathbf{x}'_0, t)$ which describes the wavefield response at any location $\mathbf{x}$ due to a source at $\mathbf{x}'_0$. (b) First type of focusing function $f_1(\mathbf{x}, \mathbf{x}'_i, t)$ that focuses to the focal point at $\mathbf{x}'_i$ from above and continues after that as the downgoing function $f_1^+(\mathbf{x}, \mathbf{x}'_i, t)$. (c) Second type of focusing function $f_2(\mathbf{x}, \mathbf{x}'_0, t)$ that focuses to the focal point at $\mathbf{x}'_0$ from below and continues after that as the upgoing function $f_2^-(\mathbf{x}, \mathbf{x}'_0, t)$. Modified after Wapenaar et al. (2014a). 7

2-2 Two different states that can be used in the reciprocity theorems Eq. (2-4a) and (2-4b). (a) Complete model with Green's functions at a depth z_i along with the complete reflection series. Both models have no free surface but a homogeneous half-space above depth z_0. (b) Truncated model with no reflection coming in from below depth z_i, such that there is only a transmission at the lower boundary. Modified after van der Neut et al. (2015a). 9

2-3 Green's and focusing functions retrieved at a focal depth of 2000 meters for the model in Table A-1 separated in the upgoing(dotted-red) and downgoing parts (solid-blue). The time gate limits are indicated in dashed-black. (a) Green's function, (b) focusing function of the first type and (c) focusing function of the second type 16

2-4 (a) Reflection series and (b) first arrival of the downgoing focusing function of the first type for the model in Table A-1 at a focal depth of 2000 meters. The events are both convolved with a 30 Hz Ricker wavelet. The black dashed lines are the time gate truncation times. 17

2-5 (a) Initial estimation of the upgoing Green's function obtained by convolving $\mathbf{f}_{1d}^{+}$ with the reflection series and muting all events before the first arrival. (b) Convolution of $\mathbf{f}_{1d}^{+}$ with the reflection series with no muting applied. (c) Convolution of the time-reversed reflection series with the events in between the time gate truncation times from (b). (d) Convolution of the reflection series with the events in between the time gate truncation times from (c). In (d) the events below the lower time gate truncation time and above the upper one are the first update to the upgoing Green's function and need to be added to the events in (a). All events are based on the model found inTable A-1 and have been convolved with a 30 Hz Ricker wavelet with a focal depth of 2000 m. 19

2-6 (a) Initial estimation of the upgoing Green's function, (b) updates of the upgoing Green's function and (c) final upgoing Green's function after 8 iterations. All events are based on the model found inTable A-1 and have been convolved with a 30 Hz Ricker wavelet with a focal depth of 2000 m. 20

2-7 Schematic overview of reflection events with an internal first-order multiple in the medium of Table A-1 with a focal depth of 2000 meters and (a) a direct path from the focal depth to the receiver and (b) an indirect path from the focal depth to the receiver. The path of the wavefield is given in red, the focal depth in dashed dark blue and the redatuming from the receiver side in dashed green. 20

2-8 Schematic overview of reflection events with an internal second-order multiple in the medium of Table A-1 with a focal depth of 2000 meters and (a) a direct path from the focal depth to the receiver and (b) an indirect path from the focal depth to the receiver. (c) indicates the wavepath of a first order multiple that also overlaps in time with the events in (a) and (b). The path of the wavefield is given in red, the focal depth in dashed dark blue and the redatuming from the receiver side in dashed green. 21

2-9 (a) Initial estimation of the downgoing Green's function obtained by time-reversing $\mathbf{f}_{1d}^{+}$. (b) Time-reversed convolution of $\mathbf{f}_{1d}^{+}$ with the reflection series with no muting applied. This result is the time-reversed version of the one found in Figure 2-5 (b). (c) Time-reversed convolution of the reflection series with the events in between the time gate truncation times from (b). In (c) the events below the lower time gate truncation time and above the upper one are the first update to the downgoing Green's function and need to be subtracted from the events in (a). All events are based on the model found inTable A-1 and have been convolved with a 30 Hz Ricker wavelet with a focal depth of 2000 m. All the events are time-reversed in order to get a causal downgoing Green's function 22

2-10 (a) Initial estimation of the downgoing Green's function, (b) updates of the downgoing Green's function and (c) final downgoing Green's function after 8 iterations. All events are based on the model found inTable A-1 and have been convolved with a 30 Hz Ricker wavelet with a focal depth of 2000 m. 22

2-11 Schematic overview of reflection events with an internal multiple in a medium with a focal depth above the deepest reflector and (a) a direct path from the focal depth to the receiver and (b) an indirect path from the focal depth to the receiver. The path of the wavefield is given in red, the focal depth in dashed dark blue and the redatuming from the receiver side and source side in dashed green. 27

2-12 Two different states that can be used in the reciprocity theorems Eq. (2-4a) and (2-4b) (a) Physical medium containing all the reflections due to a simulated source at the focal depth z_i. (b) Truncated model with no reflection coming in from below depth z_i with a focal point at $\mathbf{x}'_F$. Modified after Wapenaar et al. (2014a). 30

3-1 Reflection series without surface multiples retrieved at the surface for (a) the simple model in Table A-1, (b) the weak model in Table A-2 and (c) the artifact model in Table A-3. All of these series have been generated with a 30 Hz Ricker wavelet. . . . 36

3-2 Scaling factor $a(z_f)$ for the transmission losses at every 1 meter depth for (a) the simple model in Table A-1, (b) the weak model in Table A-2 and (c) the artifact model in Table A-3. The locations of the layer contrasts have been indicated in dashed green. . . . 37

3-3 (a) Modeled first arrival of the downgoing focusing function of the first type. (b) Convolution of the reflection series and the trace in (a). (c) Convolution of the time-reversed reflection series with the events in (b) after the muting window Θ has been applied. All of these events were generated using the simple model in Table A-1 at a focal depth of 1520 meters using a 30 Hz Ricker wavelet. The time gate truncation times are indicated in dashed black. Note that the time gate truncation time is overlying part of an event in (b) and that the events in (c) are distorted. . . . 37

3-4 Scaling factor $a(z_f)$ for the transmission losses at every 1 meter depth for (a) the simple model in Table A-1, (b) the weak model in Table A-2 and (c) the artifact model in Table A-3. The transition over layer contrasts is smoothed using a cosine function. The locations of the layer contrasts have been indicated in dashed green. 38

3-5 Cost function j_I using Eq. (2-60) for the simple model in Table A-1 at a focal depth of 2700 meters with a source strength q of (black) $\frac{2}{3}$, (blue) 1 and (red) 2. The location of the correct value of b is indicated by the close-dashed vertical lines. The y-axis is logarithmic. . . . 39

3-6 (a) Initial estimation of the upgoing Green's function, (b) updates of the upgoing Green's function and (c) final upgoing Green's function after 8 iterations for a correction factor b of (solid blue) 1, (dashed red) 0.5 and (dotted black) 1.5. All events are based on the model found inTable A-1 and have been convolved with a 30 Hz Ricker wavelet with a focal depth of 2700 m and have been normalized with $|G_0^{-,+}|_2$ of the relevant reflection series. . . . 40

3-7 Cost function j_I using Eq. (2-60) for the weak model in Table A-2 at a focal depth of 2700 meters with a source strength q of (black) $\frac{2}{3}$, (blue) 1 and (red) 2. The location of the correct value of b is indicated by the close-dashed vertical lines. The y-axis is logarithmic. . . . 40

3-8 Cost function j_I using Eq. (2-60) for the artifact model in Table A-3 at a focal depth of 2700 meters with a source strength q of (black) $\frac{2}{3}$, (blue) 1 and (red) 2. The location of the correct value of b is indicated by the close-dashed vertical lines. The y-axis is logarithmic. . . . 41

3-9 Cost function j_I using Eq. (2-60) for the simple model in Table A-1 at a focal depth of 2200 meters with a source strength q of (black) $\frac{2}{3}$, (blue) 1 and (red) 2. The location of the correct value of b is indicated by the close-dashed vertical lines. The y-axis is logarithmic. . . . 42

3-10 (a) Initial estimation of the upgoing Green's function, (b) updates of the upgoing Green's function and (c) final upgoing Green's function after 8 iterations for a correction factor b of (solid blue) 1.2, (dashed red) 1.0 and (dotted black) 1.4. All events are based on the model found inTable A-1 and have been convolved with a 30 Hz Ricker wavelet with a focal depth of 2200 m and have been normalized with $|G_0^{-,+}|_2$ of the relevant reflection series. . . . 43

3-11 Cost function j_I using Eq. (2-60) for the weak model in Table A-2 at a focal depth of 2200 meters with a source strength q of (black) $\frac{2}{3}$, (blue) 1 and (red) 2. The location of the correct value of b is indicated by the close-dashed vertical lines. The y-axis is logarithmic. 43

3-12 (a) Initial estimation of the upgoing Green's function, (b) updates of the upgoing Green's function and (c) final upgoing Green's function after 8 iterations for a correction factor b of (solid blue) 1.0, (dashed red) 0.5 and (dotted black) 1.5. All events are based on the model found inTable A-2 and have been convolved with a 30 Hz Ricker wavelet with a focal depth of 2200 m and have been normalized with $|G_0^{-,+}|_2$ of the relevant reflection series. 44

3-13 Cost function j_I using Eq. (2-60) for the artifact model in Table A-3 at a focal depth of 2200 meters with a source strength q of (black) $\frac{2}{3}$, (blue) 1 and (red) 2. The location of the correct value of b is indicated by the close-dashed vertical lines. The y-axis is logarithmic. 44

3-14 Cost function j_{II} using Eq. (2-66) for the simple model in Table A-1 at a focal depth of 2700 meters with a source strength q of (black) $\frac{2}{3}$, (blue) 1 and (red) 2. The location of the correct value of b is indicated by the close-dashed vertical lines. The y-axis is logarithmic. 46

3-15 (a) Initial estimation of the truncated reflection series, (b) updates of the truncated reflection series and (c) final truncated reflection series after 8 iterations for a correction factor b of (solid blue) 1, (dashed red) 0.5 and (dotted black) 1.5. All events are based on the model found inTable A-1 and have been convolved with a 30 Hz Ricker wavelet with a focal depth of 2700 m and have been normalized with $|R_{0,0}|_2$ of the relevant reflection series. 46

3-16 Cost function j_{II} using Eq. (2-66) for the weak model in Table A-2 at a focal depth of 2700 meters with a source strength q of (black) $\frac{2}{3}$, (blue) 1 and (red) 2. The location of the correct value of b is indicated by the close-dashed vertical lines. The y-axis is logarithmic. 47

3-17 Cost function j_{II} using Eq. (2-66) for the artifact model in Table A-3 at a focal depth of 2700 meters with a source strength q of (black) $\frac{2}{3}$, (blue) 1 and (red) 2. The location of the correct value of b is indicated by the close-dashed vertical lines. The y-axis is logarithmic. 47

3-18 Cost function j_{II} using Eq. (2-66) for the simple model in Table A-1 at a focal depth of 2200 meters with a source strength q of (black) $\frac{2}{3}$, (blue) 1 and (red) 2. The location of the correct value of b is indicated by the close-dashed vertical lines. The y-axis is logarithmic. 48

3-19 (a) Initial estimation of the truncated reflection series, (b) updates of the truncated reflection series and (c) final truncated reflection series after 8 iterations for a correction factor b of (solid blue) 1, (dashed red) 0.5 and (dotted black) 1.5. All events are based on the model found inTable A-1 and have been convolved with a 30 Hz Ricker wavelet with a focal depth of 2200 m and have been normalized with $|R_{0,0}|_2$ of the relevant reflection series. 49

3-20 Cost function j_{II} using Eq. (2-66) for the weak model in Table A-2 at a focal depth of 2200 meters with a source strength q of (black) $\frac{2}{3}$, (blue) 1 and (red) 2. The location of the correct value of b is indicated by the close-dashed vertical lines. The y-axis is logarithmic. 49

3-21 Cost function j_{II} using Eq. (2-66) for the artifact model in Table A-3 at a focal depth of 2200 meters with a source strength q of (black) $\frac{2}{3}$, (blue) 1 and (red) 2. The location of the correct value of b is indicated by the close-dashed vertical lines. The y-axis is logarithmic. 50

3-22 (a) Initial estimation of the truncated reflection series, (b) updates of the truncated reflection series and (c) final truncated reflection series after 8 iterations for a correction factor b of (solid blue) 1, (dashed red) 0.5 and (dotted black) 1.5. All events are based on the model found inTable A-3 and have been convolved with a 30 Hz Ricker wavelet with a focal depth of 2200 m and have been normalized with $|R_{0,0}|_2$ of the relevant reflection series. 50

3-23 Cost function j_{III} using Eq. (2-75) for the simple model in Table A-1 at a focal depth of 2700 meters with a source strength q of (black) $\frac{2}{3}$, (blue) 1 and (red) 2. The location of the correct value of b is indicated by the close-dashed vertical lines. The y-axis is logarithmic. 51

3-24 Cost function j_{III} using Eq. (2-75) for the weak model in Table A-2 at a focal depth of 2700 meters with a source strength q of (black) $\frac{2}{3}$, (blue) 1 and (red) 2. The location of the correct value of b is indicated by the close-dashed vertical lines. The y-axis is logarithmic. 52

3-25 Cost function j_{III} using Eq. (2-75) for the artifact model in Table A-3 at a focal depth of 2700 meters with a source strength q of (black) $\frac{2}{3}$, (blue) 1 and (red) 2. The location of the correct value of b is indicated by the close-dashed vertical lines. The y-axis is logarithmic. 52

3-26 (a) Initial estimation of the physical response, (b) updates of the physical response and (c) final physical response after 8 iterations for a correction factor b of (solid blue) 1, (dashed red) 0.5 and (dotted black) 1.5. All events are based on the model found inTable A-1 and have been convolved with a 30 Hz Ricker wavelet with a focal depth of 2700 m and have been normalized with $|G_0^{-,+}|_2$ of the relevant reflection series. 53

3-27 Cost function j_{III} using Eq. (2-75) for the simple model in Table A-1 at a focal depth of 2200 meters with a source strength q of (black) $\frac{2}{3}$, (blue) 1 and (red) 2. The location of the correct value of b is indicated by the close-dashed vertical lines. The y-axis is logarithmic. 54

3-28 (a) Green's functions using the correct source strength of $q = 1$ and correction factor $b = 1$, (b) Green's functions using the incorrect source strength of $q = 2$ and correction factor $b = 0.49$ and (c) difference between the events in (b) and (a). All events are based on the model found inTable A-1 and have been convolved with a 30 Hz Ricker wavelet with a focal depth of 2200 m . Notice that the amplitudes of (c) are much weaker than the events in (a) and (b) 55

3-29 (a) Initial estimation of the physical response, (b) updates of the physical response and (c) final physical response after 8 iterations for a correction factor b of (solid blue) 1, (dashed red) 0.5 and (dotted black) 1.5. All events are based on the model found inTable A-1 and have been convolved with a 30 Hz Ricker wavelet with a focal depth of 2200 m and have been normalized with $|G_0^{-,+}|_2$ of the relevant reflection series. 56

3-30 Cost function j_{III} using Eq. (2-75) for the weak model in Table A-2 at a focal depth of 2200 meters with a source strength q of (black) $\frac{2}{3}$, (blue) 1 and (red) 2. The location of the correct value of b is indicated by the close-dashed vertical lines. The y-axis is logarithmic. 56

3-31 (a) Initial estimation of the physical response, (b) updates of the physical response and (c) final physical response after 8 iterations for a correction factor b of (solid blue) 1, (dashed red) 0.5 and (dotted black) 1.5. All events are based on the model found inTable A-2 and have been convolved with a 30 Hz Ricker wavelet with a focal depth of 2200 m and have been normalized with $|G_0^{-,+}|_2$ of the relevant reflection series. 57

3-32 Cost function j_{III} using Eq. (2-75) for the artifact model in Table A-3 at a focal depth of 2200 meters with a source strength q of (black) $\frac{2}{3}$, (blue) 1 and (red) 2. The location of the correct value of b is indicated by the close-dashed vertical lines. The y-axis is logarithmic. 57

3-33 (a) Initial estimation of the physical response, (b) updates of the physical response and (c) final physical response after 8 iterations for a correction factor b of (solid blue) 1, (dashed red) 0.5 and (dotted black) 1.5. All events are based on the model found inTable A-3 and have been convolved with a 30 Hz Ricker wavelet with a focal depth of 2200 m and have been normalized with $|G_0^{-,+}|_2$ of the relevant reflection series. 58

List of Tables

A-1 Velocity and density distribution for the simple model 63
A-2 Velocity and density distribution for the weak model 63
A-3 Velocity and density distribution for the artifact model 63

Nomenclature

Latin Symbols

a	Scaling factor
b	Correction factor
D	First arrival wave in 2D/3D
$\mathbb{D}$	Medium
$\partial\mathbb{D}$	Medium boundary
f	Focusing function
$\mathbf{f}$	Vector containing all focusing functions
G	Green's function
$\mathbf{g}$	Vector containing all Green's function
j	Imaginary number
j_I	First cost function in 1D
j_{II}	Second cost function in 1D
j_{III}	Third cost function in 1D
J_I	First cost function in 2D/3D
J_{III}	Third cost function in 2D/3D
$\mathcal{L}$	Operator to transfrom flux- to pressure-normalized fields
p	General wavefield
q	Source strength
R, $\mathcal{R}$	Reflection series
$\tilde{R}$	Reflection series with incorrect source strength
$\hat{R}$	Reflection series with wavelet applied
$\mathbf{R}$	Matrix which applies a convolution with the reflection series R
$\mathbf{R}^*$	Matrix which applies a convolution with the time-reversed reflection series R
t	Time

t_L	Transmission losses in 2D/3D
T	Transmission response
U	Updates of the Green's functions
W	Wavelet
$\mathbf{x}$	Location vector
$\mathbf{x}_0$	Depth vector
$\mathbf{x}'_F$	Point location vector

Greek Symbols

δ_H	2D horizontal delta function
ϵ	Half of the wavelet thickness of W
Θ	Time gate that removes all events after the direct arrival including the direct arrival
ξ	Direct part of the downgoing wavefield
Ψ	Time gate that removes all events before the direct arrival
Ψ_m	Time gate that removes all events before the direct arrival including the direct arrival
Ψ_d	Time gate that removes all events except the direct arrival
Ω	Operator that applies the equivalent of $\mathbf{\Theta R}^*\mathbf{\Theta R}$
Ω^*	Operator that applies the equivalent of $\mathbf{\Theta R \Theta R}^*$

Chapter 1

Introduction

An important subject in the field of geophysics is the practice of seismic imaging. Seismic imaging uses seismic data that was recorded at the surface of a medium to generate an image of the reflectivity of this medium. An example of imaging is the boundary value migration method from McMechan (1983) which uses the primary reflections that are measured on the surface of the medium. This requires a boundary on which receivers are located and reflection data that does not contain any multiples. In more recent years methods have been developed which not only use the primary reflection data but also the multiply scattered components (Oristaglio, 1989), (Fleury, 2012). The problem with these methods is that they require closed-boundary integrals. In other words they require receivers around the medium in order to accurately function, especially in media with strong scatterers (Wapenaar et al., 2016). In practice, receivers are only located on the surface of the Earth and not on a closed boundary. It is possible to have receivers in boreholes, but this still does not create a closed boundary and is expensive and difficult. Alternatively Green's functions can be used at every image point due to sources at the surface of the Earth to create an image. A Green's function describes the response of a medium to an impulsive unit source (Stakgold and Holst, 2011). Green's functions can be decomposed in an upgoing and downgoing part and by deconvolving the upgoing Green's function with the downgoing Green's function, a seismic image can be created (Wapenaar et al., 2016). This requires the Green's function to be known at every location in the subsurface. These Green's functions can be retrieved using seismic interferometry (Wapenaar and Fokkema, 2006), but this method also requires a closed boundary with receivers placed on this boundary. Recently a new method has been developed to retrieve these Green's functions at depth using only a reflection response recorded at the surface, requiring no closed boundary and no receivers in the medium. This method is based on the Marchenko equation and was first proposed in 1D by Broggini and Snieder (2012) and further extended to also be functioning in 2D and 3D by Wapenaar et al. (2014b). The method requires a reflection response recorded at the surface and an accurate estimate for the arrival of the first event at a location in the medium, the so-called focal point. The deconvolution of the retrieved upgoing and downgoing Green's functions will then describe the response of the medium at this focal point. The first arrival can be obtained from a smooth velocity model which is a necessity in seismic processing (Yilmaz, 2001). By using iterative substitution of the events in the

Marchenko equation, the events after the direct arrivals i.e. the coda can also be recovered. van der Neut et al. (2015a) gives a very nice overview of the implication of the method as well as a more intuitive method to interpret the equations. In Figure 1-1 (a) the Green's function has been retrieved for a simple model in 1D described in Table A-1 at a depth of 2000 meters which will be called the focal depth. It shows a strong first arrival and a weaker coda after the first arrival. The first arrival is not located a zero time due to the fact that the focal point is located at depth and not at the surface. There are problems with the method however, which prevents its widespread application on real data as of this thesis. The first arrival that can be modeled needs to be accurate and the source signature needs to be known. An error in the first arrival results only in an incorrect focal position. Using the incorrect source signature can have much stronger effects. The phase and amplitude determine the signature of the source. In Figure 1-1 the effect of correct phase and incorrect source amplitude (or strength as it will be referred to) is shown. The reflection series is scaled with an incorrect source strength q of 1.5 in Figure 1-1 (b) and a q of 2.0 in (c). When compared with the correction solution in Figure 1-1 (a) it can be seen that the incorrect source strength causes wrong amplitudes for correct events and introduces artifacts, which can have a stronger amplitude than the first arrival. The problem is that the correct reflection series $\mathcal{R}$ is scaled by an incorrect scaling factor q such that:

$$\tilde{\mathcal{R}} = q \cdot \mathcal{R}, \tag{1-1}$$

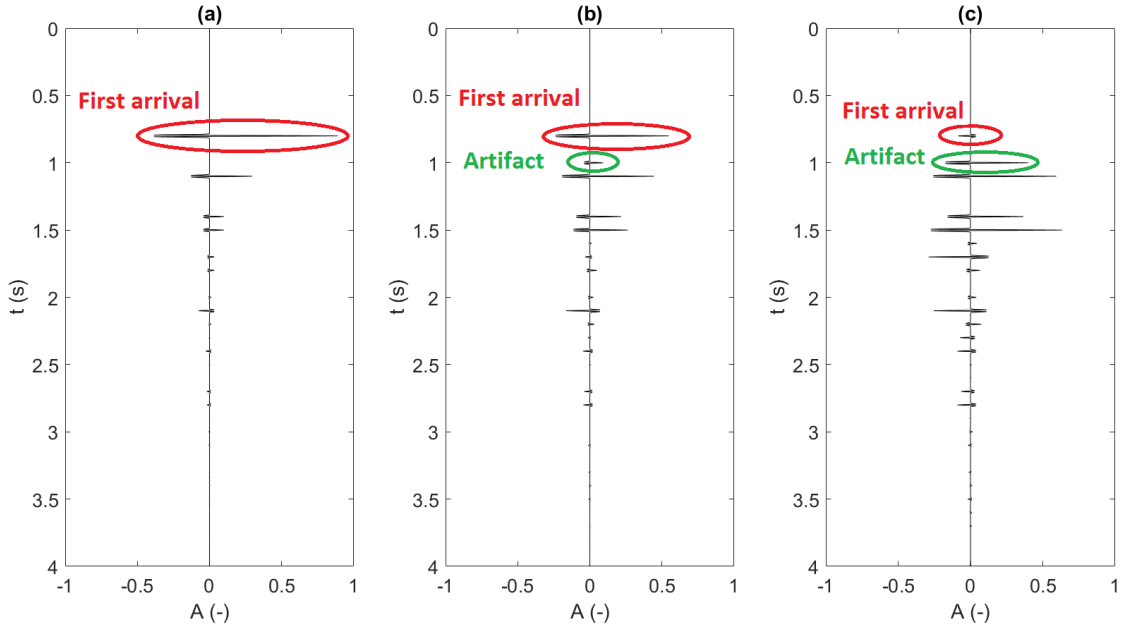

Figure 1-1: Green's function retrieved at a focal depth of 2000 meter for a simple model using a source strength that was (a) unscaled, (b) scaled with a factor of 1.5 and (c) scaled with a factor of 2.0. First arrivals are indicated in red and artifacts due to incorrect scaling are indicated in green

where $\tilde{\mathcal{R}}$ indicates that the reflection series $\mathcal{R}$ has been scaled incorrectly with q. In this thesis the goal is to find a correction factor b such that:

$$\mathcal{R} = b \cdot \tilde{\mathcal{R}} \tag{1-2}$$

To this extent, a cost function is used, based on the Green's functions that can be retrieved with the Marchenko scheme, in order to find b. A cost function depends on one or more parameters and has a minimum for these parameters. If implemented correctly, this minimum is located at the desired value of the parameters. In this thesis, the only parameter is the factor b. van der Neut et al. (2015b) proposed a cost function based on the minimization of the upgoing Green's function. This method only functions if the area of interest is located above very weak reflectors when compared to strong reflectors in the overburden. In case there are strong reflectors located below the focal point, the cost function fails. In this thesis, an improved cost function that is capable of handling a focal point above the deepest reflector will be presented. To this end, in chapter 2 the basic theory of the Marchenko scheme will be used to derive the old and the new cost function in order to find correction factor b. Furthermore, a scaling factor $a(\mathbf{x}'_f)$ will be determined as well, where $\mathbf{x}'_f = (x_f, y_f, z_f)$ is the location of the focal point. This is done because the first arrivals are often modeled in smoothed velocity models that do not produce the correct amplitudes for these first arrivals and could yield incorrect results when the retrieved Green's functions are used. In chapter 3, the results will show that the new cost function is more robust than the old cost function and is able to handle reflectors below the focal point. After this, an outlook will be given as this is only the first step in the development of adaptive measures that could make the application of the Marchenko scheme to real data easier.

Chapter 2

Theory

In this chapter, the derivation of the equations used for the Marchenko scheme will be shown as well as the theoretical idea behind it. The structure of these equations is similar to the one found in van der Neut et al. (2015a) and Wapenaar et al. (2014b). An example of imaging is the Reverse Time Migration (RTM) method (Amundsen and Robertsson, 2014), (McMechan, 1983). This method requires that the response of a source in the medium is recorded on the surface around the medium. This recorded response is then backpropagated through the medium, which can be done using Green's functions (Zhan et al., 2014). By cross-correlating these events with the source wavefield, the image is obtained. A problem with this approach is that in real media the sources and receivers are not present around the target of interest, but only at the surface of the Earth. The required Green's functions are usually computed in a smooth velocity model, which is often not accurate enough to correctly represent the actual medium and Green's functions. This leads to the emergence of artifacts (Wapenaar et al., 2014b). This is due to the fact that the Green's functions retrieved by the back propagation from the receiver side contain events that can only be canceled by the injection of the wavefields from all boundaries of the medium. Because there are only receivers at the surface of the Earth this is not the case and this will lead to the development of artifacts. In order to prevent this kind of artifacts, Wapenaar et al. (2014b) suggested so called focusing functions. A Green's function describes how the wavefield propagates from the source through the medium and time-reversing it describes how the wavefield back-propagates through the medium to the source position. This again requires that the Green's function describes a wavefield that is injected from all sides of the medium. The focusing function is defined such that when it is injected from only one side into the medium, it focuses to a specific location in the subsurface called the focal point. This is because the focusing function is defined by a specific focusing condition in a truncated medium, which is identical to the real physical medium until the focal point, but after this point the medium is replaced with a reflection-free half-space. An important property of both the focusing functions and Green's functions is that the functions can be separated in an upgoing and downgoing part at any depth. According to Wapenaar et al. (2014a), a Green's function can then be expressed as the sum of its upgoing and downgoing part:

$$G(\mathbf{x}, \mathbf{x}'_0, t) = \mathcal{L}(z_i)\mathcal{L}(z_0)\left[G^{+,+}(\mathbf{x}, \mathbf{x}'_0, t) + G^{-,+}(\mathbf{x}, \mathbf{x}'_0, t)\right] \tag{2-1}$$

In this thesis, a general wavefield in time is expressed as $p(\mathbf{x}, t)$, where $\mathbf{x} = (x, y, z)$ is the location in space and t is the time. If a location is fixed in depth, it is defined with a subscript such as $\mathbf{x}_0 = (x, y, z_0)$, where x and y can be variable. In case of a $'$ the exact location is intended such that $\mathbf{x}'_0 = (x_0, y_0, z_0)$. In Eq. (2-1) $G(\mathbf{x}, \mathbf{x}'_0, t)$ describes the wavefield response at any general location $\mathbf{x} = (x, y, z)$ at time t due to a source at specific point location $\mathbf{x}'_0 = (x_0, y_0, z_0)$. The function $G^{+,+}(\mathbf{x}, \mathbf{x}'_0, t)$ describes only the downgoing wavefield response and $G^{-,+}(\mathbf{x}, \mathbf{x}'_0, t)$ describes the upgoing wavefield response, both due to a downgoing source. In Geophysics, it is convention to take the third axis z as pointing downward and positive with increasing depth. As such, the positive is pointing downwards and the negative upwards. For Green's functions the first superscript indicates the orientation of the wavefield and the second supercript the orientation of the source. The operator $\mathcal{L}$ gives a relation between the pressure-normalized and flux-normalized wavefields, dependent on depth (Wapenaar and Grimbergen, 1996). In this thesis, the flux-normalized wavefields are used because the derivation is more straight-forward. Eq. (2-1) shows how the full Green's function can be computed using its flux-normalized components. A visual clarification of the Green's function is given in Figure 2-1 (a). A source at $\mathbf{x}'_0$ causes a wavefield which then propagates throughout the medium to different locations in this medium. It can be separated into an upgoing and downgoing part. The source is located on the boundary $\partial\mathbb{D}_0$ that separates the inhomogeneous medium from the homogeneous half-space above it. No upgoing waves reflect above the boundary $\partial\mathbb{D}_0$ so only the downgoing waves from the source can cause the Green's functions at depth, as indicated by their superscripts. Note that in this setup there is no free-surface present. In the Marchenko scheme that will be derived here, the free-surface multiples are not considered. In case of data that does contain these multiples, the free-surface multiples need to be removed by free-surface multiple elimination. Examples of this process can be found in Verschuur et al. (1992) and Amundsen (2001). Two types of focusing function can be distinguished, indicated by the subscripts 1 and 2. Each of these types can be written as the summation of the upgoing and downgoing components:

$$f_1(\mathbf{x}, \mathbf{x}'_i, t) = f_1^+(\mathbf{x}, \mathbf{x}'_i, t) + f_1^-(\mathbf{x}, \mathbf{x}'_i, t) \tag{2-2a}$$
$$f_2(\mathbf{x}, \mathbf{x}'_0, t) = f_2^+(\mathbf{x}, \mathbf{x}'_0, t) + f_2^-(\mathbf{x}, \mathbf{x}'_0, t) \tag{2-2b}$$

The two types of focusing functions are different in the way they focus. The focusing function $f_1(\mathbf{x}, \mathbf{x}'_i, t)$ focuses from above to a focal point $\mathbf{x}'_i = (x_i, y_i, z_i)$ after which it travels further to deeper depths as only a downgoing function $f_1^+(\mathbf{x}, \mathbf{x}'_i, t)$. Below the focal depth z_i, there are no reflections present. This is due to the choice of medium. As can be seen in Figure 2-1 (b), the medium is chosen such that there is a reflection-free half-space below the focal depth z_i. In the same way the focusing function of the second type $f_2(\mathbf{x}, \mathbf{x}'_0, t)$ focuses to the focal point from below and then continues above the focal point as the upgoing focusing function $f_2^-(\mathbf{x}, \mathbf{x}'_0, t)$. For the second type of focusing function the medium is a reflection-free half-space above the focal point as can be seen Figure 2-1 (c). These focusing functions can be used to derive a scheme to recover the Green's function at the focal point.

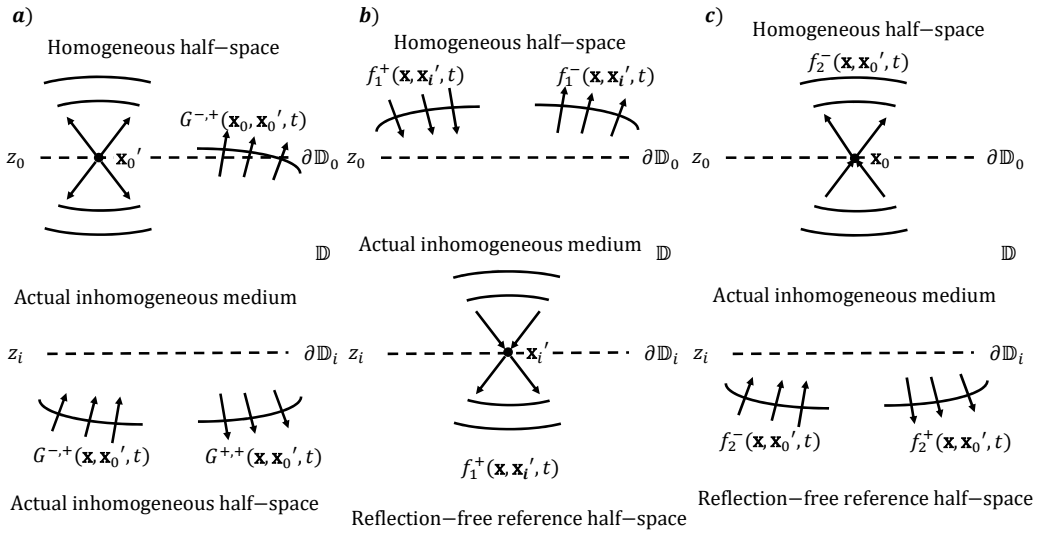

Figure 2-1: Visual clarification of Green's function and the two type of focusing functions. (a) Green's function $G(\mathbf{x},\mathbf{x}_0',t)$ which describes the wavefield response at any location $\mathbf{x}$ due to a source at $\mathbf{x}_0'$. (b) First type of focusing function $f_1(\mathbf{x},\mathbf{x}_i',t)$ that focuses to the focal point at $\mathbf{x}_i'$ from above and continues after that as the downgoing function $f_1^+(\mathbf{x},\mathbf{x}_i',t)$. (c) Second type of focusing function $f_2(\mathbf{x},\mathbf{x}_0',t)$ that focuses to the focal point at $\mathbf{x}_0'$ from below and continues after that as the upgoing function $f_2^-(\mathbf{x},\mathbf{x}_0',t)$. Modified after Wapenaar et al. (2014a).

2-1 Marchenko scheme

The derivation that will be shown closely follows the ones that can be found in Wapenaar et al. (2014b) and van der Neut et al. (2015a). The Fourier transform is used to transform the wavefield to the frequency domain. This transform along with its inverse to transform back to the time domain is:

$$p(\mathbf{x},\omega) = \int_{-\infty}^{+\infty} exp(-j\omega t)p(\mathbf{x},t)dt \tag{2-3a}$$

$$p(\mathbf{x},t) = \frac{1}{2\pi}\int_{-\infty}^{+\infty} exp(j\omega t)p(\mathbf{x},\omega)d\omega, \tag{2-3b}$$

where $p(\mathbf{x},\omega)$ is the wavefield in the frequency domain, j is the imaginary number and ω the angular frequency. In order to derive the scheme, two reciprocity theorems for flux-normalized fields are used which can be found in Wapenaar and Grimbergen (1996):

$$\int_{\partial\mathbb{D}_0}(p_A^+p_B^- - p_A^-p_B^+)d^2\mathbf{x} = \int_{\partial\mathbb{D}_i}(p_A^+p_B^- - p_A^-p_B^+)d^2\mathbf{x} \tag{2-4a}$$

$$\int_{\partial\mathbb{D}_0}(p_A^+p_B^{+*} - p_A^-p_B^{-*})d^2\mathbf{x} = \int_{\partial\mathbb{D}_i}(p_A^+p_B^{+*} - p_A^-p_B^{-*})d^2\mathbf{x} \tag{2-4b}$$

Eq. (2-4a) is a reciprocity theorem of the convolution type for two wavefields that are propagating forward in time. It states that the two different integrals carried out over the boundaries $\partial\mathbb{D}_0$ and $\partial\mathbb{D}_i$ are equal for the wavefields from two different media as long as there are no sources present between the boundaries and the media are identical in between the boundaries. Eq. (2-4b) is a reciprocity theorem of the correlation type, where one wavefield is propagating forward in time and the other wavefield backward in time. A wavefield propagating backwards in the time domain is complex conjugated in the frequency domain, which is denoted with a *. A limitation that this theorem imposes is that the medium between $\partial\mathbb{D}_0$ and $\partial\mathbb{D}_i$ needs to be lossless. Another limitation is that evanescent wave modes are ignored at the boundaries. In order to use these theorems, a model is defined for a realistic situation as shown in Figure 2-2. Different medium parameters are used depending on the states. The first state, shown in Figure 2-2 (a), is for the complete model, where the Green's functions at depth z_i need to be recovered. The upgoing and downgoing Green's functions $G^{-,+}(\mathbf{x}_i,\mathbf{x}'_a,t)$ and $G^{+,+}(\mathbf{x}_i,\mathbf{x}'_a,t)$ can be seen. At the boundary $\partial\mathbb{D}_0$, a reflection response can be recorded due to the downward oriented source at $\mathbf{x}'_a$. This reflection series is located just above the boundary and can be written as $R(\mathbf{x}_0,\mathbf{x}'_a,t)$. The medium in Figure 2-2 (b) is identical to the one in (a) with the exception that the model is truncated with a reflection-free half-space below the boundary $\partial\mathbb{D}_i$. Thus there are no reflections coming from below the boundary $\partial\mathbb{D}_i$. There is only a reflection series at the surface, which will be different from $R(\mathbf{x}_0,\mathbf{x}'_a,t)$ and will be expressed as $R_B(\mathbf{x}_0,\mathbf{x}'_b,t)$. There is also a transmission series propagating from the boundary $\partial\mathbb{D}_0$ to $\partial\mathbb{D}_i$ denoted as $T_B(\mathbf{x}_i,\mathbf{x}'_b,t)$. The sources at $\mathbf{x}'_a$ and $\mathbf{x}'_b$ can be at the same position but do not have to be. The only thing they always have in common is their depth, just above the boundary $\partial\mathbb{D}_0$. The medium in Figure 2-2 (a) is defined as state A and the

medium in Figure 2-2 (b) as state B. The subscripts $\mathbf{x}'_a$ and $\mathbf{x}'_b$ indicate whether a source is located in the medium associated with state A or state B. These subscripts are arbitrary and only indicate a random source position.

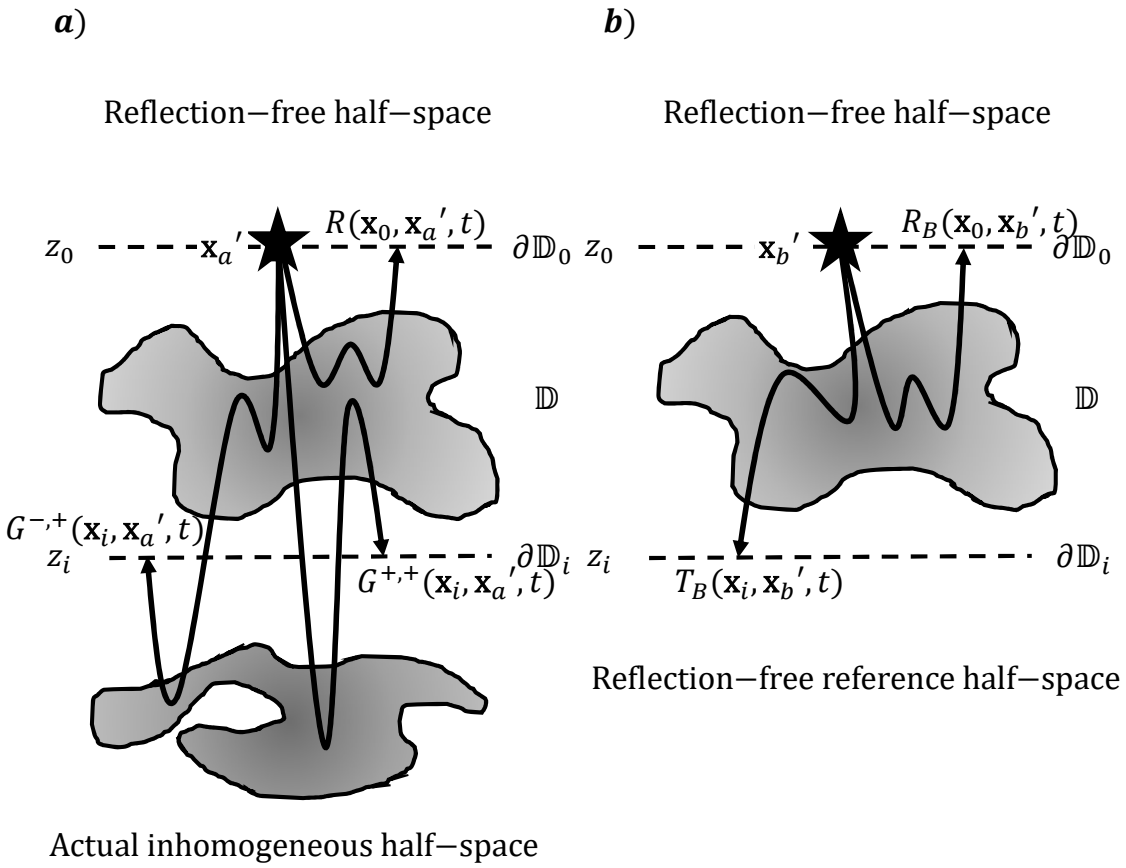

Figure 2-2: Two different states that can be used in the reciprocity theorems Eq. (2-4a) and (2-4b). (a) Complete model with Green's functions at a depth z_i along with the complete reflection series. Both models have no free surface but a homogeneous half-space above depth z_0. (b) Truncated model with no reflection coming in from below depth z_i, such that there is only a transmission at the lower boundary. Modified after van der Neut et al. (2015a).

The wavefields in these two states can now be substituted into Eq. (2-4a) and (2-4b). First the wavefields are defined. The sources at $\mathbf{x}'_a$ and $\mathbf{x}'_b$ are defined as two 2D delta functions such that the downgoing wavefields at boundary $\partial\mathbb{D}_0$ are both the direct result of these delta functions. This results in $p^+_A(\mathbf{x}_0,\omega) = \delta_H(\mathbf{x}_0 - \mathbf{x}'_a)$ and $p^+_B(\mathbf{x}_0,\omega) = \delta_H(\mathbf{x}_0 - \mathbf{x}'_b)$. The sources are indicated with an δ_H, where the H-subscript indicates that these are horizontal sources. They have a fixed depth and only vary in horizontal directions. Furthermore, the upgoing wavefields at this boundary are in both cases the reflection response and therefore it follows that $p^-_A(\mathbf{x}_0,\omega) = R(\mathbf{x}_0,\mathbf{x}'_a,\omega)$ and $p^-_B(\mathbf{x}_0,\omega) = R_B(\mathbf{x}_0,\mathbf{x}'_b,\omega)$. At the lower boundary $\partial\mathbb{D}_i$, there is a clear difference between the two states. In state A, the wavefields are the Green's functions such that $p^\pm_A(\mathbf{x}_i,\omega) = G^{\pm,+}(\mathbf{x}_i,\mathbf{x}'_a,\omega)$. In state B, there is no upgoing field such that $p^-_B(\mathbf{x}_i,\omega) = 0$. The downgoing field consists of the transmission series at this depth: $p^+_B(\mathbf{x}_i,\omega) = T_B(\mathbf{x}_i,\mathbf{x}'_b,\omega)$. If all these expression are inserted into Eq. (2-4a) and (2-4b) and

the integrals are evaluated where possible, the result is:

$$R(\mathbf{x}'_b, \mathbf{x}'_a, t) - R_B(\mathbf{x}'_a, \mathbf{x}'_b, \omega) = \int_{\partial\mathbb{D}_i} T_B(\mathbf{x}_i, \mathbf{x}'_b, \omega) G^{-,+}(\mathbf{x}_i, \mathbf{x}'_a, \omega) d^2\mathbf{x}_i \tag{2-5}$$

$$-\int_{\partial\mathbb{D}_i} R^*(\mathbf{x}'_b, \mathbf{x}'_a, \omega) R_B(\mathbf{x}'_a, \mathbf{x}'_b, \omega) d^2\mathbf{x} + \delta_H(\mathbf{x}'_b - \mathbf{x}'_a) = \int_{\partial\mathbb{D}_i} T_B(\mathbf{x}_i, \mathbf{x}'_b, \omega) G^{+,+*}(\mathbf{x}_i, \mathbf{x}'_a, \omega) d^2\mathbf{x}_i \tag{2-6}$$

To evaluate these equations further, the focusing functions that were defined before are examined. These focusing functions work in a truncated medium exactly the same as the state B that was defined earlier. As a way to define the focusing function, the transmission response is used. Similarly to van der Neut et al. (2015a) and Wapenaar et al. (2014b), the downgoing part of the focusing function of the first type is defined as the inverse of the transmission response such that:

$$\delta_H(\mathbf{x}_i - \mathbf{x}'_F) = \int_{\partial\mathbb{D}_0} T_B(\mathbf{x}_i, \mathbf{x}'_b, \omega) f_1^+(\mathbf{x}'_b, \mathbf{x}'_F, \omega) d^2\mathbf{x}'_b, \tag{2-7}$$

where $\delta_H(\mathbf{x}_i - \mathbf{x}'_F)$ is a spatially band-limited delta pulse at a location $\mathbf{x}'_F$ on the lower boundary $\partial\mathbb{D}_i$, which is defined as the focusing location. Using this focusing function, the transmission response can be eliminated from Eq. (2-5) and (2-6) by applying f_1^+ to both sides of the equations. Then the integrals can be evaluated over the boundary $\partial\mathbb{D}_0$ and by using Eq. (2-7):

$$G^{-,+}(\mathbf{x}'_F, \mathbf{x}'_a, \omega) = \int_{\partial\mathbb{D}_0} [R(\mathbf{x}'_b, \mathbf{x}'_a, \omega) - R_B(\mathbf{x}'_a, \mathbf{x}'_b, \omega)] f_1^+(\mathbf{x}'_b, \mathbf{x}'_F, \omega) d^2\mathbf{x}'_b \tag{2-8}$$

$$G^{+,+*}(\mathbf{x}'_F, \mathbf{x}'_a, \omega) = -\int_{\partial\mathbb{D}_0} [R^*(\mathbf{x}'_b, \mathbf{x}'_a, \omega) R_B(\mathbf{x}'_a, \mathbf{x}'_b, \omega) + \delta_H(\mathbf{x}'_b - \mathbf{x}'_a)] f_1^+(\mathbf{x}'_b, \mathbf{x}'_F, \omega) d^2\mathbf{x}'_b \tag{2-9}$$

In order to further simplify these equations, a substitution is made. At the lower boundary, there is an upgoing part of the focusing function present. This is the result of the reflection series of the truncated medium interacting with the downgoing focusing function:

$$f_1^-(\mathbf{x}'_a, \mathbf{x}'_F, \omega) = \int_{\partial\mathbb{D}_i} R_B(\mathbf{x}'_a, \mathbf{x}'_b, \omega) f_1^+(\mathbf{x}'_b, \mathbf{x}'_F, \omega) d^2\mathbf{x}'_b \tag{2-10}$$

Substituting Eq. (2-10) into Eq. (2-8) and (2-9) yields:

$$G^{-,+}(\mathbf{x}'_F, \mathbf{x}'_a, \omega) = \int_{\partial\mathbb{D}_0} R(\mathbf{x}'_b, \mathbf{x}'_a, \omega) f_1^+(\mathbf{x}'_b, \mathbf{x}'_F, \omega) d^2\mathbf{x}'_b - f_1^-(\mathbf{x}'_a, \mathbf{x}'_F, \omega) \tag{2-11}$$

$$G^{+,+*}(\mathbf{x}'_F, \mathbf{x}'_a, \omega) = -\int_{\partial\mathbb{D}_0} R^*(\mathbf{x}'_b, \mathbf{x}'_a, \omega) f_1^-(\mathbf{x}'_b, \mathbf{x}'_F, \omega) d^2\mathbf{x}'_b + f_1^+(\mathbf{x}'_a, \mathbf{x}'_F, \omega) \tag{2-12}$$

These equations state that in order to retrieve the Green's functions at the focal point, all one needs are the first type of focusing function and a reflection series recorded at the surface. These two equations will be used to derive an iterative scheme to recover the Green's functions. For this purpose, the transmission response that arrives at $\partial\mathbb{D}_0$ from $\partial\mathbb{D}_i$ is used and it is defined as the inverse of the upgoing focusing function of the second type, which results in a similar equation to Eq. (2-7)

$$\delta_H(\mathbf{x}_0 - \mathbf{x}'_G) = \int_{\partial\mathbb{D}_i} T_B(\mathbf{x}_0, \mathbf{x}'_i, \omega) f_2^-(\mathbf{x}'_i, \mathbf{x}'_G, \omega) d^2\mathbf{x}'_i \tag{2-13}$$

In this case, there is a focal point $\mathbf{x}'_G$ at the boundary $\partial\mathbb{D}_0$. The upgoing focusing function of the second type reflects at deeper depths, which can be expressed as a convolution with the reflection response from below. Using this, the downgoing focusing function of the second type can be written as:

$$f_2^+(\mathbf{x}_i, \mathbf{x}'_G, \omega) = \int_{\partial\mathbb{D}_i} R_B^{\cap}(\mathbf{x}_i, \mathbf{x}'_i, \omega) f_2^-(\mathbf{x}'_i, \mathbf{x}'_G, \omega) d^2\mathbf{x}'_b, \tag{2-14}$$

where $R_B^{\cap}(\mathbf{x}_i, \mathbf{x}'_i, \omega)$ is a reflection series recorded at the lower boundary and contains reflections from the medium above. Furthermore, Wapenaar et al. (2014b) proved the relations

$$f_1^+(\mathbf{x}'_G, \mathbf{x}'_i, \omega) = f_2^-(\mathbf{x}'_i, \mathbf{x}'_G, \omega) \tag{2-15}$$

$$-f_1^{+*}(\mathbf{x}'_G, \mathbf{x}'_i, \omega) = f_2^-(\mathbf{x}'_i, \mathbf{x}'_G, \omega) \tag{2-16}$$

These relations will be important later on. First, Eq. (2-11) and (2-12) are transformed to the time domain:

$$f_1^-(\mathbf{x}'_a, \mathbf{x}'_F, t) + G^{-,+}(\mathbf{x}'_F, \mathbf{x}'_a, t) = \int_{-\infty}^{\infty}\int_{\partial\mathbb{D}_0} R(\mathbf{x}'_b, \mathbf{x}'_a, \tau) f_1^+(\mathbf{x}'_b, \mathbf{x}'_F, t-\tau) d^2\mathbf{x}'_b d\tau \tag{2-17}$$

$$f_1^-(\mathbf{x}'_a, \mathbf{x}'_F, t) - G^{+,+}(\mathbf{x}'_F, \mathbf{x}'_a, -t) = \int_{-\infty}^{\infty}\int_{\partial\mathbb{D}_0} R(\mathbf{x}'_b, \mathbf{x}'_a, \tau) f_1^-(\mathbf{x}'_b, \mathbf{x}'_F, t+\tau) d^2\mathbf{x}'_b d\tau, \tag{2-18}$$

In Eq. (2-17) the reflection series is convolved with the downgoing focusing function of the first type. In Eq. (2-18) the reflection series is cross-correlated with the upgoing focusing function of the first type. To simplify these equations even further, van der Neut et al. (2015a) proposed a discrete notation, where the focusing functions are stored in the vector $\mathbf{f}_1^{\pm}$, the Green's functions are stored in the vector $\mathbf{g}^{\pm,+}$, the convolution with the reflection responses is described by the matrix $\mathbf{R}$ and the cross-correlation with the reflection series is stored in the matrix $\mathbf{R}^*$. Using this discretization Eq. (2-17) and (2-18) can be rewritten as:

$$\mathbf{f}_1^- + \mathbf{g}^{-,+} = \mathbf{R}\mathbf{f}_1^+ \tag{2-19}$$

$$\mathbf{f}_1^+ + \mathbf{g}^{+,+*} = \mathbf{R}^* \mathbf{f}_1^-, \tag{2-20}$$

where $\mathbf{g}^{+,+*}$ indicates that the downgoing Green's function is the time-reversed version of $\mathbf{g}^{+,+}$ in the time domain. Now there are two equations with four unknowns , $\mathbf{g}^{-,+}, \mathbf{g}^{+,+*}, \mathbf{f}_1^-$ and $\mathbf{f}_1^+$. The reflection matrix $\mathbf{R}$ is acquired at the surface and therefore known. For $\mathbf{R}^*$ the reflection series only need to be time-reversed so this matrix is also known. At this moment, the system is underdetermined and therefore some adjustments have to be made. In order to do this, the downgoing Green's function is considered to consist of a direct arrival, $\mathbf{g}_d^{+,+}$, and a coda, $\mathbf{g}_m^{+,+}$, arriving after the direct arrival. The Marchenko theory proposes a matrix window $\mathbf{\Theta}$ that removes the direct wave and the coda. Every event that arrives before this direct arrival in time is preserved however. $\mathbf{\Theta}$ is applied to Eq. (2-19) and (2-20). Some of the terms can have events that arrive before the direct arrival of the downgoing Green's functions. The direct arrival arrives at a time t_d so a time gate just before this time is chosen. The data that is recorded is band-limited however and as such a wavelet needs to be applied to the data. Assuming that this wavelet is zero-phase, the thickness of the wavelet requires the limit of $\mathbf{\Theta}$ to be shifted half the wavelet thickness to avoid muting part of the events. This means that the truncation time of $\mathbf{\Theta}$ is located at $t_d - \epsilon$, where ϵ is at least half the wavelet thickness. The time window is symmetrical in time and therefore acausal events that arrive in negative time before the time of the time-reversed direct arrival are also muted. In this case, the window limit is located at time $-t_d + \epsilon$. This window effectively mutes the entire downgoing Green's function. The upgoing Green's function's first arrival can never arrive earlier than the downgoing Green's function. Thus $\mathbf{\Theta}$ also completely mutes both the downgoing and upgoing Green's function:

$$\mathbf{\Theta} \mathbf{g}^{-,+} = 0 \tag{2-21}$$

$$\mathbf{\Theta} \mathbf{g}^{+,+*} = 0 \tag{2-22}$$

The question is what happens if this window is applied to the focusing function. The downgoing focusing function is the inverse of the transmission response as stated in Eq. (2-7). $\mathbf{T}_B$ is defined as a matrix that applies a convolution with the transmission response. By transforming Eq. (2-7) to the time domain and using discrete notation, the result is:

$$\mathbf{i} = \mathbf{T}_B \mathbf{f}_1^+, \tag{2-23}$$

where $\mathbf{i}$ is a delta pulse at the location of the focal point $\mathbf{x}'_F$ at zero time. Just like the downgoing Green's function $\mathbf{T}_B$, can be split up in a matrix for a convolution with the direct arrival, $\mathbf{T}_{Bd}$, and a matrix for a convolution with the coda, $\mathbf{T}_{Bm}$. A focusing function is defined as the direct arrival of $\mathbf{f}_1^+$ and is called $\mathbf{f}_{1d}^+$. It can be separated from its coda, $\mathbf{f}_{1m}^+$. van der Neut et al. (2015a) defined that the inverse of the direct arrival of the transmission response is equal to the direct arrival of the focusing function:

$$\mathbf{i} = \mathbf{T}_{Bd} \mathbf{f}_{1d}^+ \tag{2-24}$$

Then Eq. (2-23) can be substituted in Eq. (2-24):

$$\mathbf{T}_B\mathbf{f}_1^+ = \mathbf{T}_{Bd}\mathbf{f}_{1d}^+ \tag{2-25a}$$
$$(\mathbf{T}_{Bd} + \mathbf{T}_{Bm})(\mathbf{f}_{1d}^+ + \mathbf{f}_{1m}^+) = \mathbf{T}_{Bd}\mathbf{f}_{1d}^+ \tag{2-25b}$$
$$\mathbf{T}_{Bm}\mathbf{f}_{1d}^+ = -(\mathbf{T}_{Bd} + \mathbf{T}_{Bm})\mathbf{f}_{1m}^+ \tag{2-25c}$$

Some important properties of the focusing functions can be derived from this result. Eq. (2-24) states that the first arrival of the focusing function is the inverse of the first arrival of the transmission response. The entire right side of Eq. (2-24) has to be causal as the left side is causal. The coda of the transmission response arrives later than the direct arrival, so if $\mathbf{T}_{Bm}$ is convolved with $\mathbf{f}_{1d}^+$ the result will be completely causal. As such, both the left and right side of Eq. (2-25c) have to be causal. Therefore the convolution of $\mathbf{T}_B$ with the coda of the focusing function is causal. Consequently both the direct part and the coda of the focusing function convolved with the transmission response are causal and the coda of the focusing function cannot arrive earlier than the time-reversed direct arrival of the transmission response. $\mathbf{f}_{1d}^+$ is also the time-reversed direct arrival of the downgoing Green's function. Using the fact that $\mathbf{f}_{1d}^+$ arrives at the time of the time-reversed direct arrival, it follows from Eq. (2-15) that the first arrival in $\mathbf{f}_2^-$ is also arriving at the time of the time-reversed direct arrival. According to Eq. (2-14) $\mathbf{f}_2^+$ is related to $\mathbf{f}_2^-$ by convolving it with a causal reflection response. This means that the events in $\mathbf{f}_2^+$ are also all arriving after the time-reversed direct arrival. Then Eq. (2-16) can be used to determine that $\mathbf{f}_1^-$ arrives completely before the direct arrival. Using these relations, it can be determined how the focusing functions react to the time window. The direct arrival of $\mathbf{f}_1^+$ arrives at the same time (but time-reversed) as the direct arrival of the downgoing Green's function and will therefore be removed. The coda arrives later than the time-reversed direct arrival and will be unaffected just like all of the events in $\mathbf{f}_1^-$. Therefore

$$\mathbf{\Theta}\mathbf{f}_1^+ = \mathbf{\Theta}(\mathbf{f}_{1d}^+ + \mathbf{f}_{1m}^+) = \mathbf{f}_{1m}^+ \tag{2-26}$$

$$\mathbf{\Theta}\mathbf{f}_1^- = \mathbf{f}_1^- \tag{2-27}$$

Using these results and by applying $\mathbf{\Theta}$ to Eq. (2-19) and (2-20):

$$\mathbf{\Theta}\mathbf{f}_1^- + \mathbf{\Theta}\mathbf{g}^{-,+} = \mathbf{\Theta}\mathbf{R}\mathbf{f}_1^+ \tag{2-28a}$$
$$\mathbf{f}_1^- = \mathbf{\Theta}\mathbf{R}(\mathbf{f}_{1d}^+ + \mathbf{f}_{1m}^+) \tag{2-28b}$$
$$\mathbf{f}_1^- = \mathbf{\Theta}\mathbf{R}\mathbf{f}_{1d}^+ + \mathbf{\Theta}\mathbf{R}\mathbf{f}_{1m}^+ \tag{2-28c}$$

$$\mathbf{\Theta}\mathbf{f}_1^+ - \mathbf{\Theta}\mathbf{g}^{+,+*} = \mathbf{\Theta}\mathbf{R}^*\mathbf{f}_1^- \tag{2-29a}$$
$$\mathbf{\Theta}(\mathbf{f}_{1d}^+ + \mathbf{f}_{1m}^+) = \mathbf{\Theta}\mathbf{R}^*\mathbf{f}_1^- \tag{2-29b}$$
$$\mathbf{f}_{1m}^+ = \mathbf{\Theta}\mathbf{R}^*\mathbf{f}_1^- \tag{2-29c}$$

Eq. (2-28c) and (2-29c) are the Marchenko equations, which can be used to derive the Green's functions. In order to do this, two things are required, the reflection series that was recorded at the upper boundary and $\mathbf{f}_{1d}^{+}$, which can be inserted into both equations. As stated before, $\mathbf{f}_{1d}^{+}$ is the inverse of the direct arrival of the transmission response and can be approximated by time-reversal as there is only one event in this response. This direct arrival can be recorded with a receiver at depth or alternatively it can be estimated from a smooth velocity model. A velocity model is necessary for seismic processing and therefore does not require extra effort (Yilmaz, 2001). Assuming that $\mathbf{f}_{1d}^{+}$ is known and the coda $\mathbf{f}_{1m}^{+}$ needs to be recovered, Eq. (2-28c) can be combined with Eq. (2-29c), yielding:

$$\mathbf{f}_{1m}^{+} = \boldsymbol{\Theta}\mathbf{R}^{*}(\boldsymbol{\Theta}\mathbf{R}\mathbf{f}_{1d}^{+} + \boldsymbol{\Theta}\mathbf{R}\mathbf{f}_{1m}^{+}) \tag{2-30a}$$

$$\mathbf{f}_{1m}^{+} - \boldsymbol{\Theta}\mathbf{R}^{*}\boldsymbol{\Theta}\mathbf{R}\mathbf{f}_{1m}^{+} = \boldsymbol{\Theta}\mathbf{R}^{*}\boldsymbol{\Theta}\mathbf{R}\mathbf{f}_{1d}^{+} \tag{2-30b}$$

$$[\mathbf{I} - \boldsymbol{\Theta}\mathbf{R}^{*}\boldsymbol{\Theta}\mathbf{R}]\mathbf{f}_{1m}^{+} = \boldsymbol{\Theta}\mathbf{R}^{*}\boldsymbol{\Theta}\mathbf{R}\mathbf{f}_{1d}^{+} \tag{2-30c}$$

This is a Fredholm equation of the second kind and can be written as a Neumann series (van der Neut et al., 2015a):

$$\mathbf{f}_{1}^{+(K)} = \sum_{k=0}^{K} \boldsymbol{\Omega}^{k}\mathbf{f}_{1d}^{+} \tag{2-31}$$

In this equation, $\boldsymbol{\Theta}\mathbf{R}^{*}\boldsymbol{\Theta}\mathbf{R}$ has been replaced by $\boldsymbol{\Omega}$. This equation can be inserted into Eq. (2-28c), yielding:

$$\mathbf{f}_{1}^{-(K)} = \boldsymbol{\Theta}\mathbf{R}\sum_{k=0}^{K} \boldsymbol{\Omega}^{k}\mathbf{f}_{1d}^{+} \tag{2-32}$$

These two equations can be used to recover the complete focusing functions if the direct arrival and the reflection response are known. Using these results, it is also possible to determine the Green's functions by using a different filter. For this purpose, the time gate $\boldsymbol{\Psi}$ is defined. This gate filters the complement of $\boldsymbol{\Theta}$. Hence $\boldsymbol{\Psi}$ filters out the focusing functions except for $\mathbf{f}_{1d}^{+}$ and does not filter out the events of the Green's functions. Thus $\boldsymbol{\Psi} = \mathbf{I} - \boldsymbol{\Theta}$ and this filter can be applied to Eq. (2-19) and (2-20)

$$\boldsymbol{\Psi}\mathbf{f}_{1}^{-} + \boldsymbol{\Psi}\mathbf{g}^{-,+} = \boldsymbol{\Psi}\mathbf{R}\mathbf{f}_{1}^{+} \tag{2-33a}$$

$$\mathbf{g}^{-,+} = \boldsymbol{\Psi}\mathbf{R}(\mathbf{f}_{1d}^{+} + \mathbf{f}_{1m}^{+}) \tag{2-33b}$$

$$\mathbf{g}^{-,+} = \boldsymbol{\Psi}\mathbf{R}\mathbf{f}_{1d}^{+} + \boldsymbol{\Psi}\mathbf{R}\mathbf{f}_{1m}^{+} \tag{2-33c}$$

$$\boldsymbol{\Psi}\mathbf{f}_{1}^{+} - \boldsymbol{\Psi}\mathbf{g}^{+,+*} = \boldsymbol{\Psi}\mathbf{R}^{*}\mathbf{f}_{1}^{-} \tag{2-34a}$$

$$\boldsymbol{\Psi}(\mathbf{f}_{1d}^{+} + \mathbf{f}_{1m}^{+}) - \mathbf{g}^{+,+*} = \boldsymbol{\Psi}\mathbf{R}^{*}\mathbf{f}_{1}^{-} \tag{2-34b}$$

$$\mathbf{g}^{+,+*} = \mathbf{f}_{1d}^{+} - \boldsymbol{\Psi}\mathbf{R}^{*}\mathbf{f}_{1}^{-} \tag{2-34c}$$

Combining these results with Eq. (2-31) and (2-32) gives

$$\mathbf{g}^{-,+(K)} = \mathbf{\Psi R} \sum_{k=0}^{K} \mathbf{\Omega}^k \mathbf{f}_{1d}^{+} \tag{2-35}$$

$$\mathbf{g}^{+,+*(K)} = [\mathbf{I} - \mathbf{\Psi R}^{*} \mathbf{\Theta R} \sum_{k=0}^{K-1} \mathbf{\Omega}^k] \mathbf{f}_{1d}^{+} \tag{2-36}$$

These equations are valid for any $K > 0$, and the base values are defined as $\mathbf{g}^{-,+(0)} = \mathbf{\Psi R f}_{1d}^{+}$ and $\mathbf{g}^{*+,+(0)} = \mathbf{f}_{1d}^{+}$. These equations can be used instead of Eq. (2-31) and (2-32) to directly calculate the Green's functions. It should be pointed out that this configuration assumes that there is no free surface present at the surface of the Earth. Extra terms can be included to take a free surface into account (Singh et al., 2015), but that is not considered in the scope of this investigation.

2-2 Construction of Green's functions

The cost functions that will be derived are based on the way the Green's functions are constructed and updated from direct arrival of the focusing function and the reflection response, when the Marchenko scheme is utilized. An overview of the construction of the Green's and focusing functions is shown here. For a more detailed description it is advised to read van der Neut et al. (2015a). In Figure 2-3 the Green's function and focusing functions are plotted for a focal depth of 2000 meters for the model in Table A-1. In this case the reflection series is correct. The results were retrieved using a modeled delta pulse with an amplitude of 1 for the initial focusing function. The absolute amplitudes of the Green's functions retrieved here are therefore not correct, but the relative amplitudes are correct. The scaling of the first arrival can be corrected for afterwards to retrieve the correct absolute amplitudes. Figure 2-3 demonstrates properties of the Marchenko scheme. First of all the Green's function in Figure 2-3 (a) is located completely after the time gate that is used to compute the operator Θ and is completely causal. From this figure, it is easy to see that the time gate would mute the entire Green's function as seen in Eq. (2-21) and (2-22). The first event is the direct arrival of the Green's function that is downgoing and all the other events arrive at later times. This first event should arrive at the focal depth divided by the velocity of the model, resulting in $\frac{2000}{2500} = 0.8s$. As can be seen in Figure 2-3 (a), this event does indeed have its peak at this time. Here the effect of the wavelet on the time gate is shown. The time gate has been shifted by half the wavelet thickness i.e. ϵ to avoid overlapping with any part of the first event. Furthermore, when studying the downgoing focusing function of the first type in Figure 2-3 (b), it can be seen that the first arrival is the same as the first arrival of the Green's function, but time-reversed with a different amplitude. The focusing function is almost completely residing inside of the time gate Θ, meaning that the events are arriving in between the negative and positive truncation times of Θ. Outside the time gate would mean that the events are arriving before the negative truncation time and after the positive truncation time of Θ. The direct arrival of the downgoing focusing function is not inside Θ, which is the condition in Eq.

(2-26). The focusing function has both acausal and causal parts. The second type of focusing function in Figure 2-3 (c) also only has the direct event located outside Θ. It should be easy to see that the downgoing focusing function of the first type is exactly the same as the upgoing focusing function of the second type as stated by Eq. (2-15). If the upgoing focusing function of the first type is time-reversed and its polarity is reversed, the downgoing focusing function of the second type is recovered as stated by Eq. (2-16). The events in the Green's function are recovered by using the Marchenko method and are arriving at the correct times, but the amplitudes are not accurate, as the first arrival has not yet been scaled.

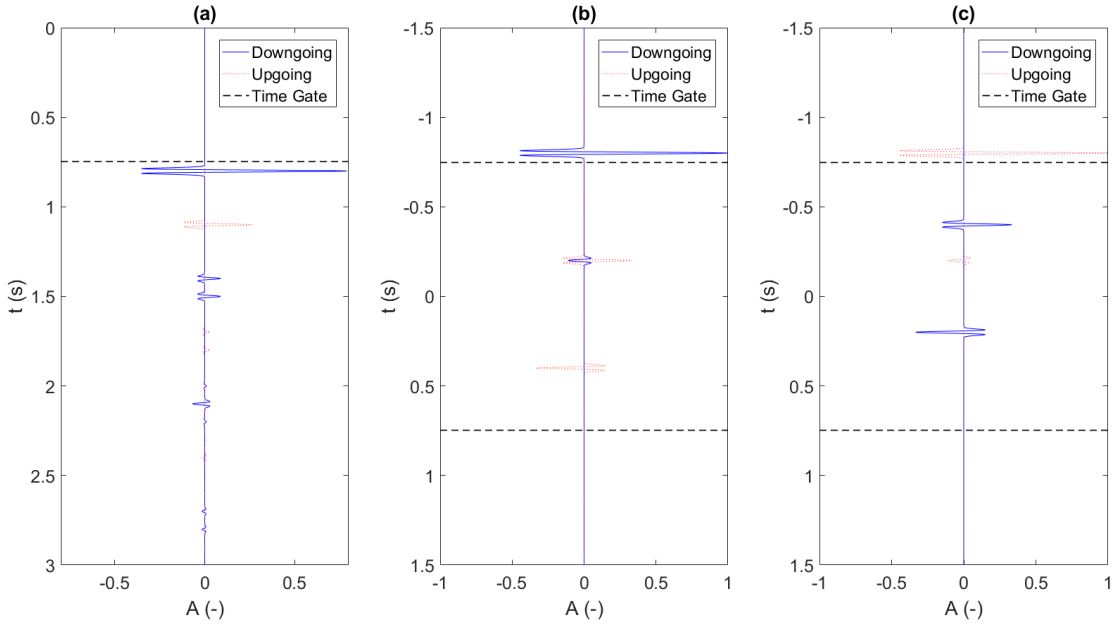

Figure 2-3: Green's and focusing functions retrieved at a focal depth of 2000 meters for the model in Table A-1 separated in the upgoing(dotted-red) and downgoing parts (solid-blue). The time gate limits are indicated in dashed-black. (a) Green's function, (b) focusing function of the first type and (c) focusing function of the second type

The results of the Marchenko scheme have been demonstrated. Now the construction of the Green's functions and focusing function are considered in greater detail. In order to do this, the reflection series and a first arrival are needed, which are modeled and shown in Figure 2-4. The first arrival was modeled using the velocity model by generating a delta pulse with an amplitude of 1 at the correct time and convolving it with a Ricker wavelet with a peak frequency of 30 Hz. The reflection series was generated using an analytical code and does not contain any noise. An important property that can be seen from the figure is that no reflection events are overlying each other. If this were the case, it could cause problems for the cost functions that will be derived later.

In Figure 2-5 the steps for the first update of the upgoing Green's function are outlined. This is done according to Eq. (2-35). The first estimation of the Green's function is shown in Figure 2-5 (a). It is obtained by convolving the estimation of the first arrival from Figure 2-4 (b) with the reflection series in Figure 2-4 (a) and then muting all events arriving before the estimated first arrival, which would be all the events inside Θ. This leads to a trace with several events on it. There is a very weak first event, which is an artifact that arrives before a

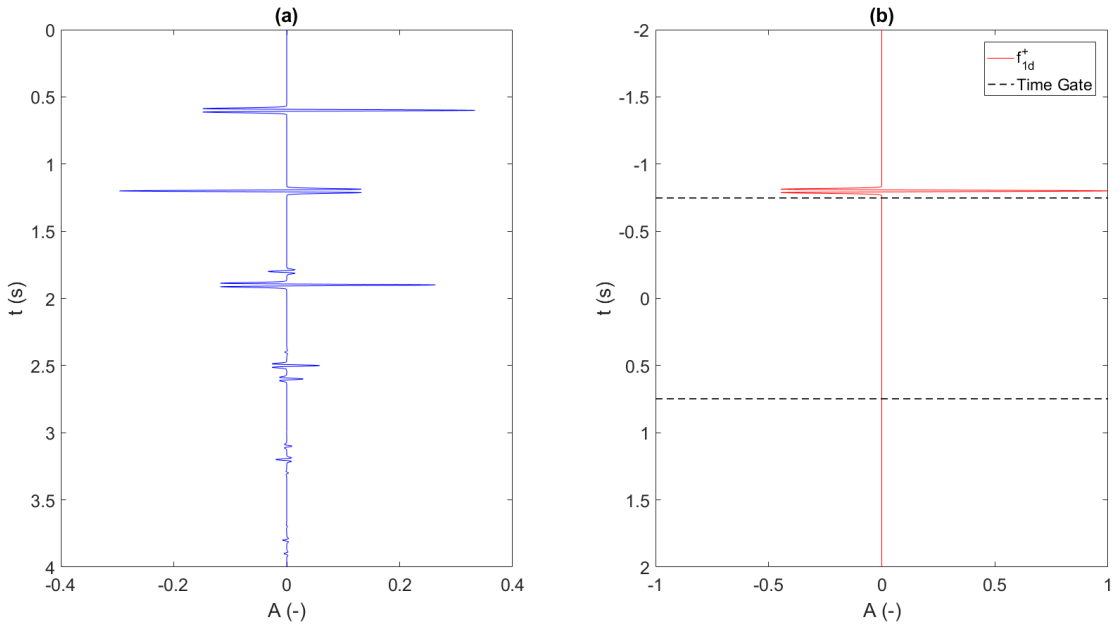

Figure 2-4: (a) Reflection series and (b) first arrival of the downgoing focusing function of the first type for the model in Table A-1 at a focal depth of 2000 meters. The events are both convolved with a 30 Hz Ricker wavelet. The black dashed lines are the time gate truncation times.

stronger event which is the true first arrival. This can be confirmed by considering the model in Table A-1 and the focal depth which leads to the conclusion that the first event should arrive at $1.1s$. Hence the earliest event needs to be removed. In Figure 2-5 (b) the result from Figure 2-5 (a) is shown before Θ was applied. Essentially the events from the reflection response are shifted by the arrival time of the first arrival to construct this trace. Because the first arrival is acausal, it shifts all the events from the reflection series backward in time. Some of them are shifted so much that they become acausal. Since the first arrival has an amplitude of 1, the shifted events do maintain their amplitudes. The events arriving after the positive time gate truncation time and before the negative time gate truncation time are identical to the ones in Figure 2-5 (a). Maintaining these events and muting the other events is the equivalent of applying Ψ. In case the filter Θ is applied, the events in between the truncation times are preserved and all the other events are removed. If this filter is applied, the result is the first estimation of the upgoing focusing function of the first type, as can be understood from Eq. (2-32). The focusing functions can be retrieved first from the iterative scheme and be used to compute the Green's functions as shown by Eq. (2-33c) and (2-34c). The filter Θ is applied to the trace in Figure 2-5 (b) and the result is convolved with the time-reversed reflection series which results in the trace shown in Figure 2-5 (c). The events are shifted further backwards in time because the entire reflection series is acausal. The amplitudes are also changed because the events all have different amplitudes than 1. In this case, the events in between the truncation times are the first update for the downgoing focusing function of the first type, as described by Eq. (2-31). Θ is applied to the trace and the result is convolved with the reflection series, which results in the trace seen in Figure 2-5 (d). The events on this trace are very weak. If Θ were to be applied, the remaining events would be the first update to the upgoing focusing function of the first type. If Ψ is applied, the remaining events are the first

update to the upgoing Green's function. If the events after the positive time gate truncation time are added to the trace in Figure 2-5 (a), the weak first event will be largely removed, although not completely. The event at $1.7s$ is also updated. This does not remove the event but rather adjusts it amplitude to the correct value. This first update improves the estimation of the Green's function significantly, however not all errors are completely removed. Further updates are required. In Figure 2-6 (a) the initial upgoing Green's function is shown which is identical to the one in Figure 2-5 (a). Figure 2-6 (c) shows the upgoing Green's function after 8 iterations, the updates of which are shown Figure 2-6 (b). This trace is very similar to the one in Figure 2-5 (d) after Ψ was applied, which contains only the first update of the upgoing Green's function. There are some amplitude differences and a few additional events with very weak amplitudes, which are due to further updates and were not present in the first update in Figure 2-5 (d). An important property of the upgoing Green's function is seen here. The updates only affect non-physical events that were present in the first estimation. No new events are introduced. The upgoing Green's function can be assumed to have a minimum energy after the updates have been applied. This is the basis on which all of the proposed cost functions are based in this thesis. Most events are dampened by the updates, however in this case there is one event at $2.4s$ which is strengthened by the updates. The cause for this effect lies in the overlap of the arrival times of physical events and artifacts and is explained by Figure 2-7. The red line in Figure 2-7 (a) indicates the wavepath of the wavefield if the source and receiver are located at the surface. This corresponds to an event in the reflection series. By convolving the time-reversed first arrival, which is indicated in green, the final part of this wavepath is essentially removed. This is because this part of the path is subtracted by the time-reversed direct arrival. In essence applying this operation is redatuming the receiver from the surface to the focal depth which is indicated in blue. Only the events that have propagated directly from the focal depth to the physical receiver on the surface are correctly redatumed by this operation. This is because this path coincides with the time-reversed direct arrival. Any event that is not coming directly from the focal depth, such as the one in Figure 2-7 (b), would be redatumed incorrectly to the focal depth and is therefore an artifact. When considering the physical first-order multiple in Figure 2-7 (a) and the artifact in Figure 2-7 (b), it can be confirmed that their traveltimes are exactly the same. The medium is from Table A-1 and in 1D but visualized in 2D to indicate the wavepath and reflections more clearly. The event has a total travelpath of 4250 meters. For the physical multiple, this is because from the surface it is 1500 meters down to the second reflector, then 750 meters up to the first reflector, then 1625 down to the third reflector and finally 2375 meters up to the surface. 2000 meters need to be subtracted because of the redatuming. For the artifact it is 2375 meters down to the third reflector, then 1625 meters up to the first reflector, then 750 meters down to the second reflector and finally 1500 meters back to the surface. In this case too, 2000 meters need to be subtracted because of the redatuming. This means that in both cases the arrival time is $\frac{4250}{2500} = 1.7s$. Looking back at the event arriving at $1.7s$ in Figure 2-6 it can be seen that this event was present in the initial estimation and was updated to have a weaker amplitude than its initial estimate. It is not removed completely however. This means that the adjustment in the amplitude is due to the removal of the artifact that is shown in Figure 2-7 (b), but the physical multiple shown in Figure 2-7 (a) remains. The travelpath of the event in Figure 2-6 that arrives at $2.4s$ is shown in Figure 2-8. Again this is a multiple but this time it reflects twice in between the layers making it a second-order multiple. Similarly to the event in Figure 2-7 two different travelpaths with the same arrival time can be determined which are shown in Figure 2-8 (a) and (b). There is also a third possibility as indicated by

Figure 2-8 (c), which actually is not a second-order multiple but a first-order multiple. Now there are three events overlapping. Furthermore, when considering the reflection points, it can be concluded that the first-order multiple has the opposite polarity compared to that of the second-order multiples. Because the Marchenko method removes the artifact from Figure 2-8 (b), this contribution is subtracted from the initial estimation. The transmission losses of the first-order multiple are weaker than that of the second-order multiples, so the amplitudes of the first-order multiples will be stronger than those of the second-order multiples. When the artifact is removed this means that there is one event less that dampens the amplitude of the first-order multiple, hence its amplitude increases. When considering these events separately the minimization of the events is still in effect. Because the events are overlying each other and interacting the result is that energy is actually added instead of removed. This will cause problems for certain cost functions as will be shown later. Additional steps will be taken to circumvent these problems.

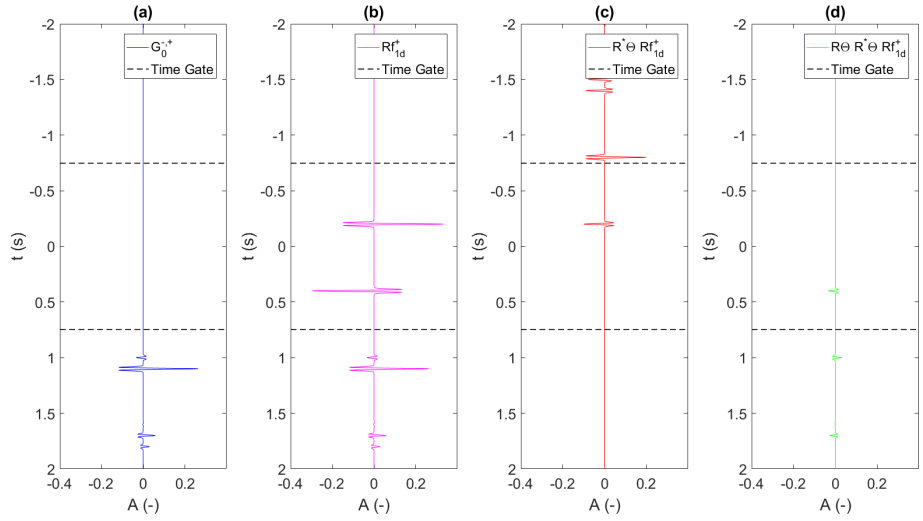

Figure 2-5: (a) Initial estimation of the upgoing Green's function obtained by convolving $\mathbf{f}_{1d}^{+}$ with the reflection series and muting all events before the first arrival. (b) Convolution of $\mathbf{f}_{1d}^{+}$ with the reflection series with no muting applied. (c) Convolution of the time-reversed reflection series with the events in between the time gate truncation times from (b). (d) Convolution of the reflection series with the events in between the time gate truncation times from (c). In (d) the events below the lower time gate truncation time and above the upper one are the first update to the upgoing Green's function and need to be added to the events in (a). All events are based on the model found inTable A-1 and have been convolved with a 30 Hz Ricker wavelet with a focal depth of 2000 m.

Similarly to the upgoing Green's function, the downgoing Green's function can also be described by its updates. There are some differences in the way these updates behave. In Figure 2-9 (a) the first estimation of the downgoing Green's function is shown, which is the time-reversed estimation of the first arrival of the focusing function of the first type from Figure 2-4 (b). Now according to Eq. (2-36) the first arrival needs to be convolved with the reflection series and this is shown in Figure 2-9 (b). This is the time-reversed version of the trace in Figure 2-5 (b). Again this is done so that the events will yield a causal downgoing

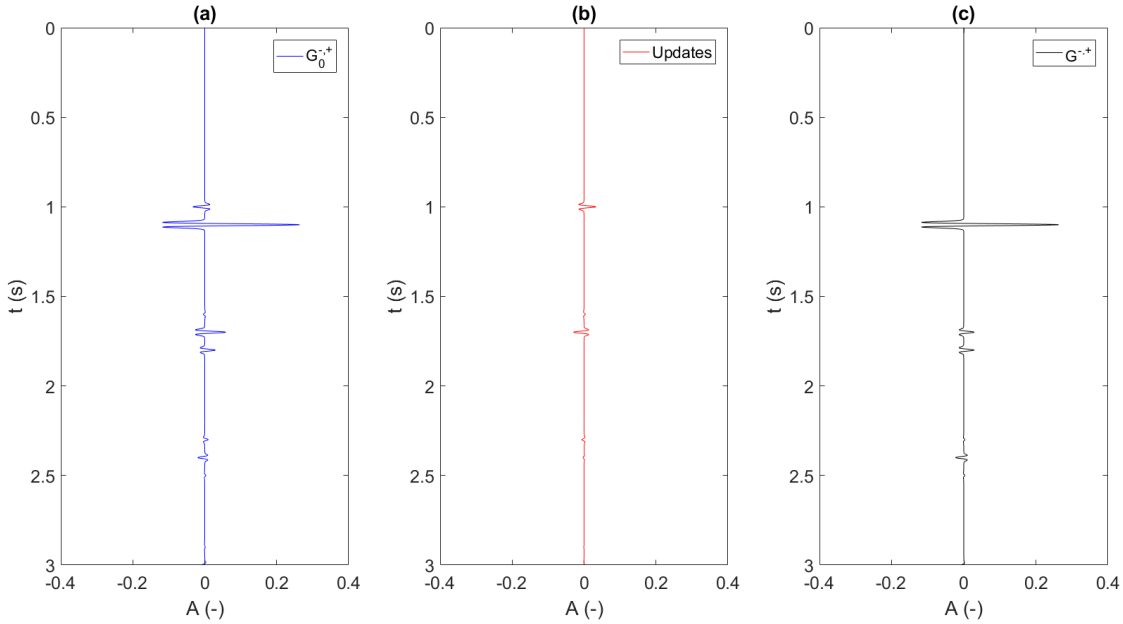

Figure 2-6: (a) Initial estimation of the upgoing Green's function, (b) updates of the upgoing Green's function and (c) final upgoing Green's function after 8 iterations. All events are based on the model found inTable A-1 and have been convolved with a 30 Hz Ricker wavelet with a focal depth of 2000 m.

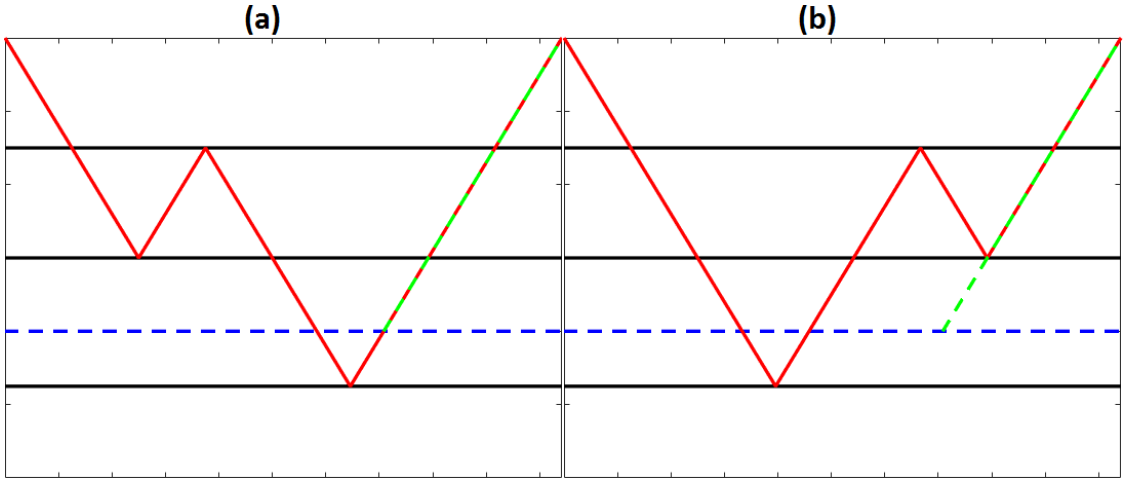

Figure 2-7: Schematic overview of reflection events with an internal first-order multiple in the medium of Table A-1 with a focal depth of 2000 meters and (a) a direct path from the focal depth to the receiver and (b) an indirect path from the focal depth to the receiver. The path of the wavefield is given in red, the focal depth in dashed dark blue and the redatuming from the receiver side in dashed green.

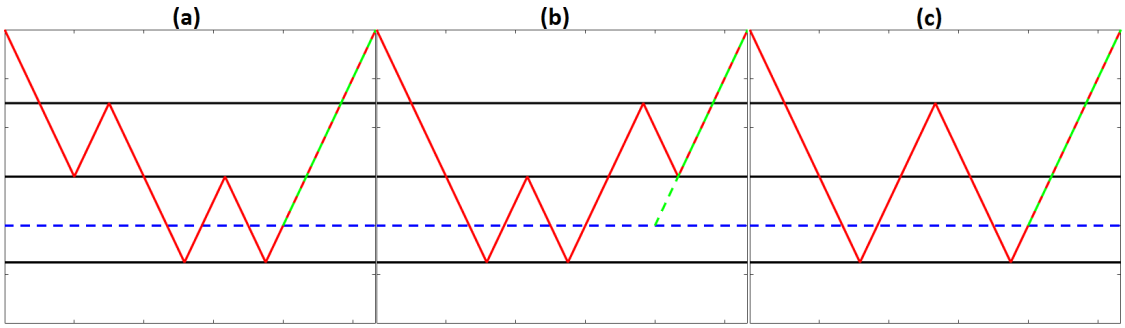

Figure 2-8: Schematic overview of reflection events with an internal second-order multiple in the medium of Table A-1 with a focal depth of 2000 meters and (a) a direct path from the focal depth to the receiver and (b) an indirect path from the focal depth to the receiver. (c) indicates the wavepath of a first order multiple that also overlaps in time with the events in (a) and (b). The path of the wavefield is given in red, the focal depth in dashed dark blue and the redatuming from the receiver side in dashed green.

Green's function. By applying Θ to the trace, convolving it with the time-reversed reflection series and time-reversing the result the trace in Figure 2-5 (c) is retrieved. If Ψ is applied to this trace the remaining events are the updates of the downgoing Green's function. According to Eq. (2-36), these updates need to be subtracted from the initial estimation instead of added. Applying the first update to the initial estimation will decrease the amplitude of the first arrival and at later times two close events with positive amplitudes will be introduced. In Figure 2-10 (a) the initial estimation of the downgoing Green's function is shown, with its updates shown in Figure 2-10 (b) and the final result after 8 iterations is shown in Figure 2-10 (c). In this figure, it can be seen that the updates do indeed dampen the first arrival partially and later events are added. Figure 2-6 and Figure 2-10 show the major difference between the way the up- and downgoing Green's functions are retrieved. As mentioned before, the upgoing Green's functions first estimation contains all the events as well as artifacts and subsequent updates remove the artifacts and adjust incorrect amplitudes. The downgoing Green's functions first estimation contains a single event, which is the first arrival and is very likely incorrectly scaled and subsequent updates add other events to the function. These differences are the reason that the downgoing Green's function cannot be used directly for the cost function, whereas the upgoing Green's function can.

2-3 Correction factor in 1D

Eq. (2-35) and (2-36) will produce a Green's function in the physical medium, provided that the reflection series and modeled first arrival are accurate enough. As explained in the previous section through the use of convolution and the time gate Θ, the Green's functions can be retrieved by updating the first estimate. For the sake of convenience, Eq. (2-35) and (2-36) are rewritten in 1D in order to make certain substitutions more straightforward:

$$\hat{G}^{-,+}(z_f,0,t) = \sum_{i=0}^{\infty} \hat{G}_i^{-,+}(z_f,0,t) \tag{2-37}$$

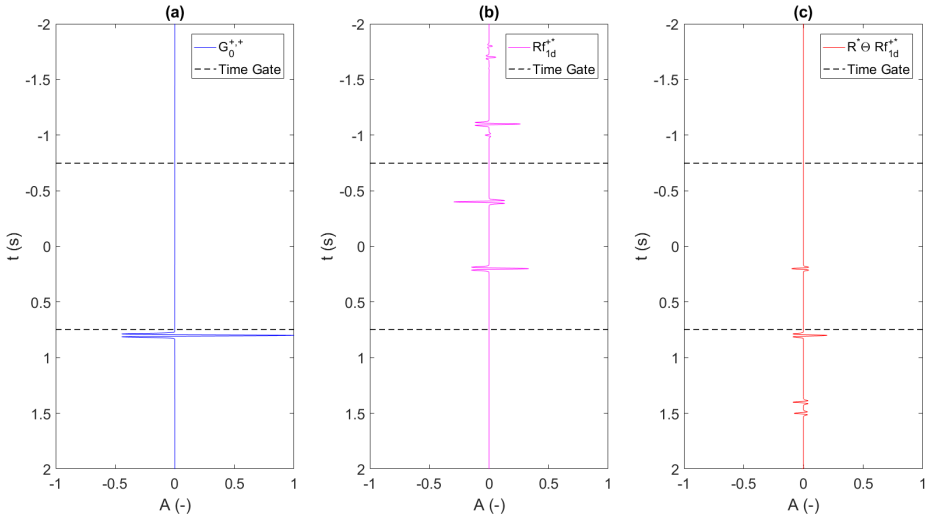

Figure 2-9: (a) Initial estimation of the downgoing Green's function obtained by time-reversing $\mathbf{f}_{1d}^{+}$. (b) Time-reversed convolution of $\mathbf{f}_{1d}^{+}$ with the reflection series with no muting applied. This result is the time-reversed version of the one found in Figure 2-5 (b). (c) Time-reversed convolution of the reflection series with the events in between the time gate truncation times from (b). In (c) the events below the lower time gate truncation time and above the upper one are the first update to the downgoing Green's function and need to be subtracted from the events in (a). All events are based on the model found inTable A-1 and have been convolved with a 30 Hz Ricker wavelet with a focal depth of 2000 m. All the events are time-reversed in order to get a causal downgoing Green's function

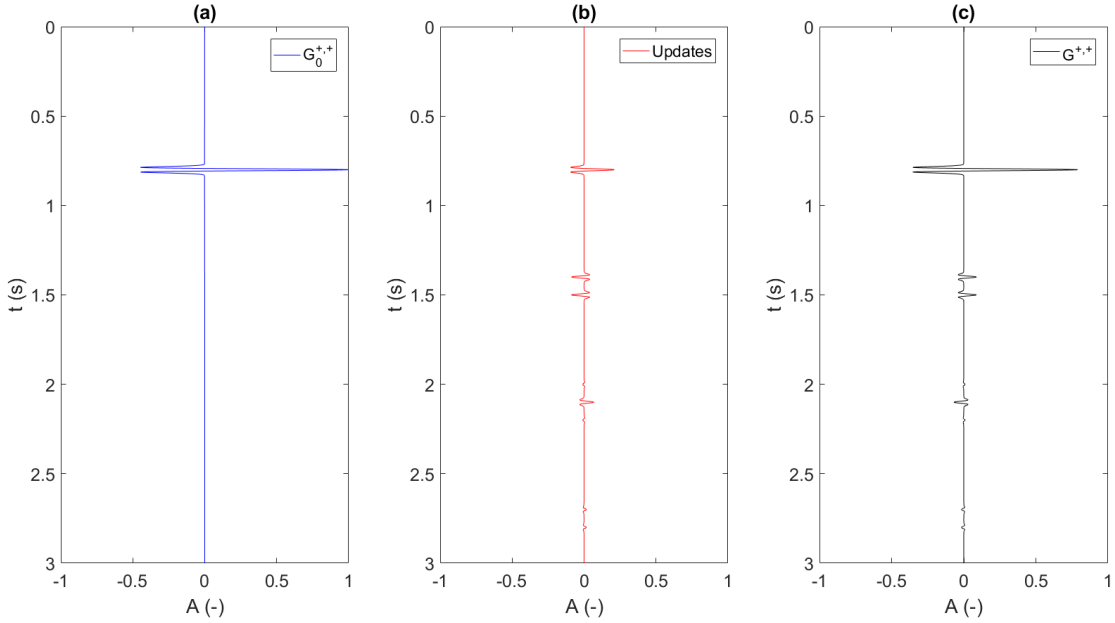

Figure 2-10: (a) Initial estimation of the downgoing Green's function, (b) updates of the downgoing Green's function and (c) final downgoing Green's function after 8 iterations. All events are based on the model found inTable A-1 and have been convolved with a 30 Hz Ricker wavelet with a focal depth of 2000 m.

$$\hat{G}_m^{+,+}(z_f,0,t) = \sum_{j=0}^{\infty} \hat{G}_{m,j}^{+,+}(z_f,0,t) \tag{2-38}$$

$$\hat{G}_d^{+,+}(z_f,0,t) = \hat{f}_{1d}^{+}(z_f,0,-t) + \sum_{k=0}^{\infty} \hat{G}_{d,k}^{+,+}(z_f,0,t) \tag{2-39}$$

Here, the Green's function that is recovered propagates from the surface, located at $z = 0$, to the focusing depth z_f in 1D. The downgoing Green's function is split into its direct arrival and its coda. Furthermore, the components in Eq. (2-38) and (2-39) have been time-reversed so that the resulting Green's function is causal. As a consequence of this choice, the direct arrival of the focusing function has to be time-reversed before it enters the equations as symbolized with the negative time symbol. The symbol $\hat{G}$ means that a wavelet has been convolved with the Green's function. The same can be done for any other wavefield. This is the same wavelet that was discussed earlier that is applied to the band-limited data and causes the shift in Θ. Assuming that the source wavelet of the reflection series has been deconvolved, the wavelet that is applied can be freely chosen. The components of the Eq. (2-37), (2-38) and (2-39) are:

$$\hat{G}_i^{-,+}(z_f,0,t) = \left\{\Psi(z_f)\,\mathcal{R}\Omega^i(z_f)\,\hat{f}_{1d}\right\}(0,z_f,t) \tag{2-40}$$

$$\hat{G}_{m,j}^{+,+}(z_f,0,t) = -\left\{\Psi_m(z_f)\,\mathcal{R}\Theta(z_f)\,\mathcal{R}^*\Omega^{*j}(z_f)\,\hat{f}_{1d}\right\}(0,z_f,-t) \tag{2-41}$$

$$\hat{G}_{d,k}^{+,+}(z_f,0,t) = -\left\{\Psi_d(z_f)\,\mathcal{R}\Theta(z_f)\,\mathcal{R}^*\Omega^{*k}(z_f)\,\hat{f}_{1d}\right\}(0,z_f,-t) \tag{2-42}$$

Two new time gates have been defined. Ψ_d filters out everything except the direct wave and Ψ_m that does the same thing as the regular Ψ filter except that it also filters out the direct arrival. These gates are used to split the downgoing wave into two seperate parts: the direct part and the coda. Also the operator $\Omega^* = \Theta\mathcal{R}\Theta\mathcal{R}^*$ is used. Thus again there is a series of summation but this time exclusively in 1D.

2-3-1 Scaling of first arrival

The previous equations can be rewritten in order to derive a cost function. Before this can be done, the amplitude of the first arrival has to be determined. As mentioned before, the first arrival can be estimated in several different ways, such as using receivers at the focal depth to measure it directly (Liu et al., 2016) or using a macro velocity model to model it. In this thesis the first arrival will always be modeled directly using synthetic models. This often means that the first arrival is modeled with an amplitude of 1 or another incorrect amplitude. This is because the modeled first arrival is computed using a smooth velocity model so transmission losses are not always exact. In order to determine the scaling factor of the first arrival so that

the Green's function has the correct amplitude, the following method is proposed. In 1D, the first arrival and its frequency transform can be defined as:

$$\hat{f}_{1d}^{+}(0,z_f,t) = a(z_f)\,\hat{W}(t+t_d(z_f)) \tag{2-43a}$$

$$\hat{f}_{1d}^{+}(0,z_f,\omega) = a(z_f)\,\hat{W}(\omega)\,exp(j\omega t_d(z_f)) \tag{2-43b}$$

Here, t_d is the arrival time of the direct wave at focal depth z_f, $a(z_f)$ is a scaling factor to compensate for transmission losses that occur while the waves are propagating through the medium and $\hat{W}(t+t_d)$ is a time reversed delta pulse occurring at time t_d which is then convolved with a wavelet. In the frequency domain, the shift associated with t_d transforms into the exponential $exp(j\omega t_d(z_f))$. An important point in Eq. (2-43a) is that a scaling factor is present. This is needed in order to make sure that the Green's functions are correctly scaled during their retrieval. This is due to the fact that at every boundary a wave passes by the impedance contrast causes a transmission loss. The factor $a(z_f)$ is the inverse of all these transmission losses and is therefore always equal or larger than 1. In case the exact background medium is known, the transmission losses can be calculated. In practice this is often not possible so in this case it is calculated independently of such a background model. In order to isolate the factor, the direct part of the downgoing Green's function is taken into account, in case that no rescaling was applied:

$$\hat{\xi}(z_f,0,t) = \hat{W}(t-t_d(z_f)) - \sum_{k=0}^{\infty}\left\{\Psi(z_f)\,\mathcal{R}\Theta(z_f)\,\mathcal{R}^{*}\Omega^{*k}(z_f)\,\hat{W}\right\}(t-t_d(z_f)) \tag{2-44}$$

This equation would contain the incorrect amplitudes, since there is no compensation for the transmission losses applied. In order to make this part of the Green's function correct, the scaling factor needs to be applied:

$$\hat{G}_d^{+,+}(z_f,0,t) = a(z_f)\,\hat{\xi}(z_f,0,t) \tag{2-45}$$

Eq. (2-24) states that the initial focusing function f_{1d}^{+} is the inverse of the direct arrival of the transmission response or the direct part of the downgoing Green's function $G_d^{+,+}$. The frequency transform is used and after convolution with the wavelet Eq. (2-24) can be written as:

$$\hat{W}(\omega) = f_{1d}^{+}(z_f,0,\omega)\,\hat{G}_d^{+,+}(z_f,0,\omega) \tag{2-46}$$

In this case the wavelet is centered at zero time. Note there is no wavelet applied over f_{1d}^{+} because that would produce a square of the wavelet on the left side of Eq. (2-46). Now Eq. (2-46) can be combined with Eq. (2-43b) (2-44) and (2-45):

$$\hat{W}(\omega) = a^2(z_f)\exp(j\omega t_d(z_f))\,\hat{\xi}(z_f,0,\omega) \tag{2-47}$$

Eq. (2-46) is assuming that the correctly scaled reflection series is used. In case this is not true or no preprocessing was applied, it can be assumed that the data has been incorrectly scaled

with an unknown source strength q, which is causing problems for the Marchenko scheme. The incorrect reflection series $\mathcal{R}$ and $\tilde{\mathcal{R}}$ are introduced that have been incorrectly scaled with this unknown source strength just like in Eq. (1-1):

$$\tilde{\mathcal{R}} = q \cdot \mathcal{R} \tag{2-48}$$

$$\tilde{\mathcal{R}}^* = q \cdot \mathcal{R}^* \tag{2-49}$$

The symbol $\tilde{R}$ indicates that the reflection series has been incorrectly scaled. In order to get the correct result the incorrect reflection series have to be multiplied with an unknown correction factor b as shown in Eq. (1-2)

$$\mathcal{R} = b \cdot \tilde{\mathcal{R}} \tag{2-50}$$

$$\mathcal{R}^* = b \cdot \tilde{\mathcal{R}}^* \tag{2-51}$$

Now in Eq. (2-44) the reflection series are replaced by substituting Eq. (2-50) and (2-51) to take the incorrect scaling into account.

$$\hat{\xi}\left(z_f, 0, t, b\right) = \hat{W}\left(t - t_d\left(z_f\right)\right) + \sum_{k=0}^{\infty} \hat{U}^+_{d,k}\left(z_f, 0, t\right) b^{2(k+1)} \tag{2-52}$$

with

$$\hat{U}^+_{d,k}\left(z_f, 0, t\right) = -\left\{\Psi_d\left(z_f\right) \tilde{\mathcal{R}} \Theta\left(z_f\right) \tilde{\mathcal{R}}^* \tilde{\Omega}^{*j}\left(z_f\right) W\right\}\left(0, z_f, -t\right) \tag{2-53}$$

where

$$\tilde{\Omega} = \boldsymbol{\Theta}\tilde{\mathbf{R}}^*\boldsymbol{\Theta}\tilde{\mathbf{R}} \tag{2-54a}$$
$$\tilde{\Omega}^* = \boldsymbol{\Theta}\tilde{\mathbf{R}}\boldsymbol{\Theta}\tilde{\mathbf{R}}^* \tag{2-54b}$$

The amount of times b is applied is equal to the amount of times $\tilde{\mathcal{R}}$ was applied. Eq. (2-47), (2-52) and (2-53) are combined to create an expression for the scaling of the direct wave:

$$a\left(z_f, b\right) = \sqrt{\left|\frac{\hat{W}\left(\omega\right)}{\hat{W}\left(\omega\right) + \exp\left(j\omega t_d\left(z_f\right)\right) \sum_{k=0}^{\infty} \hat{U}^+_{d,k}\left(z_f, 0, \omega\right) b^{2(k+1)}}\right|} \tag{2-55}$$

This equation allows for the calculation of the scaling factor $a(z_f, b)$ at any depth z_f in the 1D medium given that the correct value for b is known. In higher order dimensions the horizontal positions are also vital to obtain this factor.

2-3-2 Scaling with single-sided redatuming

Having retrieved the correct scaling of the first arrival, a cost function for single-sided scaling can be derived. This is based on the standard Marchenko scheme. The time-reversed first arrival functions as a redatuming operator that subtracts the direct path from the focal point to the physical receiver from the wavepath. This creates a so called virtual receiver at the focal point, its name indicates that the receiver is not physically there but it is computed using the equations. Certain multiples do not travel directly from the focal point and need to be removed from the Green's function as they become artifacts such as the event in Figure 2-7 (b). Eq. (2-37), (2-38), (2-40) and (2-41) are rewritten to take into account the incorrect scaling of the reflection series:

$$\hat{G}^{-,+}\left(z_f,0,t,b\right)=\sum_{i=0}^{\infty}\hat{U}_i^{-}\left(z_f,0,t\right)a\left(z_f,b\right)b^{1+2i} \tag{2-56}$$

$$\hat{G}_m^{+,+}\left(z_f,0,t,b\right)=\sum_{j=0}^{\infty}\hat{U}_{m,j}^{+}\left(z_f,0,t\right)a\left(z_f,b\right)b^{2(j+1)}, \tag{2-57}$$

where

$$\hat{U}_i^{-}\left(z_f,0,t\right)=\left\{\Psi_m\left(z_f\right)\tilde{\mathcal{R}}\tilde{\Omega}^{i}\left(z_f\right)\hat{W}\right\}\left(0,z_f,t+t_d\left(z_f\right)\right) \tag{2-58}$$

$$\hat{U}_{m,j}^{+}\left(z_f,0,t\right)=-\left\{\Psi_m\left(z_f\right)\tilde{\mathcal{R}}\Theta\left(z_f\right)\tilde{\mathcal{R}}^{*}\tilde{\Omega}^{*j}\left(z_f\right)\hat{W}\right\}\left(0,z_f,-t-t_d\left(z_f\right)\right) \tag{2-59}$$

Using these equations, the following objective function is proposed:

$$j_I\left(b\right)=\frac{|G^{-,+}\left(z_f,0,t,b\right)|_2}{|G_0^{-,+}\left(z_f,0,t,b\right)|_2} \tag{2-60}$$

where the L_2-norm is used and the denominator is defined as

$$\hat{G}_0^{-,+}\left(z_f,0,t,b\right)=\hat{U}_0^{-}\left(z_f,0,t\right)a\left(z_f,b\right)b \tag{2-61}$$

The idea behind this cost function is that if the series has been scaled correctly, the artifacts will be suppressed and the desired events will remain. In case the source strength q is too high, more artifacts will be introduced in Eq. (2-56) as seen in figure 1-1. In case the source strength q is too low, the opposite will happen and not enough energy will be removed from the artifacts. Therefore the minimum of Eq. (2-60) should be at the correct scaling factor b. This function is assumed to work when no reflector is present below the focal point. Because there are no reflections coming from below the focal point, there is no upgoing field and therefore the updated upgoing Green's function should approach 0.

For Eq. (2-60), it is assumed that there is no or very little overlap of physical events and redatumed artifacts in the time-space domain. This assumption relates directly to having no overlap of primaries and internal multiples, as is common to a variety of alternative internal

multiple elimination algorithms (Berkhout and Verschuur, 2005) and free-surface multiple elimination algorithms (Verschuur and Berkhout, 1997), (van Borselen et al., 2003). So Eq. (2-60) can be used to find b, however as stated before the function behaves optimally only if no reflectors are present below the focal point. As will be demonstrated, the function does not behave optimally in case these reflectors are present. The reason for this can be seen in Figure 2-7. As explained in section 2-2 the convolution with the time-reversed first arrival redatums from the physical receiver to the focal point. The event in Figure 2-7 (a) is a physical multiple in the Green's function but the event in Figure 2-7 (b) is an artifact and needs to be removed. These events arrive at the same time, so when the second event is removed the first event still remains. This was demonstrated by the events arriving at $1.7s$ in Figure 2-6 and Figure 2-7 in section 2-2. Even more problems arise when different order multiples are arriving at the same time as shown by the events in Figure 2-8, that arrives at $2.4s$ in Figure 2-6. In this case the updates actually increase the energy due to the interaction of the different events. This update works against the minimization of the upgoing Green's function and there are more updates behaving just like it. The relevance of this interaction is model dependent but it is present for most models, making it a serious problem in general heterogeneous media.

2-3-3 Scaling with double-sided redatuming

Because the first cost function is not functioning well in general heterogeneous media, another cost function is proposed that applies double-sided redatuming. This means that redatuming is applied at both the source and receiver side instead of only at the receiver side. The reason for this is shown in Figure 2-11. The redatuming that is also applied at the source side ensures that there is no consistent overlap between the physical events that should be preserved and non-physical events that should be removed. By applying this methodology, the problems that prevent the use of a focal point above the deepest reflector are avoided.

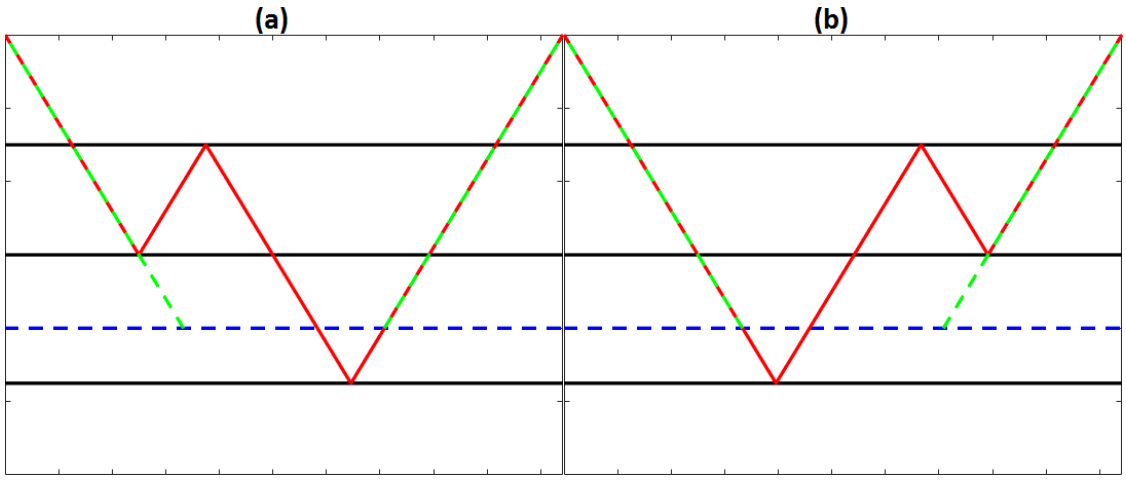

Figure 2-11: Schematic overview of reflection events with an internal multiple in a medium with a focal depth above the deepest reflector and (a) a direct path from the focal depth to the receiver and (b) an indirect path from the focal depth to the receiver. The path of the wavefield is given in red, the focal depth in dashed dark blue and the redatuming from the receiver side and source side in dashed green.

In order to apply double-sided redatuming and derive the cost function, equation 36 from

Wapenaar et al. (2014b) will be used in the frequency domain. This equation can be written in 1D as:

$$\hat{G}^{-,+}(z_f,0,\omega,b)=R_0(z_f,\omega,b)\left(\hat{G}_d^{+,+}(z_f,0,\omega,b)+\hat{G}_m^{+,+}(z_f,0,\omega,b)\right) \tag{2-62}$$

Here R_0 is the reflection series at focal depth z_f as if the medium above it were reflection free. The subscript 0 is used to define that this reflection series is defined in this truncated medium. This makes it different from the reflection series acquired at the surface which is used in the operators $\tilde{\mathcal{R}}$ and $\tilde{\mathcal{R}}^*$. $\hat{f}_{1d}^{+}$ can be applied to Eq. (2-62) and using the substitutions in Eq. (2-43b) and (2-46) the result can be rewritten after deconvolution of the wavelet as:

$$\begin{aligned}&\hat{G}^{-,+}(z_f,0,\omega\,b)\exp(j\omega t_d(z_f))\,a(z_f,b)=\\&\hat{R}_0(z_f,\omega,b)\times\left(1+\hat{W}^{-1}(\omega)\,\hat{G}_m^{+,+}(z_f,0,\omega,b)\exp(j\omega t_d(z_f))\,a(z_f,b)\right),\end{aligned} \tag{2-63}$$

where R_0 was convolved with the wavelet which yields $\hat{R}_0$. Because of this, the wavelet needs to be removed from the $\hat{G}_m^{+,+}$, which in this case is indicated by $\hat{W}^{-1}(\omega)$. The 1 in Eq. (2-63) is the result of the direct downgoing Green's function being multiplied by its inverse. The form of Eq. (2-63) is again a Fredholm integral of the second kind and can be solved for $\hat{R}_0$ using iterative substitution:

$$\begin{aligned}\hat{R}_0(z_f,\omega,b)=&\sum_{k=0}^{\infty}\left(-\hat{W}^{-1}(\omega)\exp(j\omega t_d(z_f))\,\hat{G}_m^{+,+}(z_f,0,\omega,b)\,a(z_f,b)\right)^k\times\\&\exp(j\omega t_d(z_f))\,\hat{G}^{-,+}(z_f,0,\omega,b)\,a(z_f,b)\end{aligned} \tag{2-64}$$

In this equation, it is apparent why the wavelet needed to be removed. Due to the power k the wavelet would be applied several times yielding an incorrect final result. From a physical interpretation of the individual terms, it can be seen that in the first term of the series, all physical reflections and artifacts are constructed. In subsequent terms only artifacts are being removed, similar to the series in Eq. (2-37). The first term can then be written out (by taking $k=0$) and taking the first terms of Eq. (2-56) and (2-57), yielding:

$$\hat{R}_{0,0}(z_f,\omega,b)=\exp(j\omega t_d(z_f))\,\hat{U}_0^{-}(z_f,0,\omega)\,a^2(z_f,b)\,b \tag{2-65}$$

Eq. (2-64) and (2-65) are combined to construct a double-sided cost function:

$$j_{II}(b)=\frac{\left|\hat{R}_0(z_f,t,b)\right|_2}{\left|\hat{R}_{0,0}(z_f,t,b)\right|_2} \tag{2-66}$$

In this cost function, the reflection series have been Fourier transformed back to the time domain. The function also depends non-linearly on b. However the computation of this function is more intensive than that of $j_I(b)$ in Eq. (2-60) due to the more complex nature. This cost function is much more robust against reflectors below the focal point than equation 2-60 however. Its one weakness is that this whole procedure is based on the redatuming of the events arriving at the receiver and source side. This means that if an internal multiple is coinciding in arrival time at the receivers with a physical primary, the procedure is not capable of separating these events. This will induce errors when one is trying to find the minimum (note that the equation for $j_I(b)$ has the same problem).

2-3-4 Alternative scaling with double-sided redatuming

While j_{II} is a robust cost function, it does require a large amount of focal points in order to correctly evaluate, when applied in 2D or 3D. Eq. (2-63) contains a simple multiplication in 1D but for higher order dimensions this multiplication transforms into an integral over all the focal points needed to create a full Green's function. This means that this integral will also be present in the Neumann series in Eq. (2-63). This would require an enormous amount of memory space and computing power to implement. Therefore, an alternative cost function using double-sided redatuming is introduced. To do this, the reciprocity theorem in Eq. (2-4a) is used. The two states in Figure 2-12 are used. In state A, a downgoing source is inserted at location $\mathbf{x}'_S$ which is just below the boundary $\partial\mathbb{D}_i$. The wavefield due to this source can be split into an upgoing and downgoing part such that $p_A^+ = G^{+,+}(\mathbf{x}, \mathbf{x}'_S, \omega)$ and $p_A^- = G^{-,+}(\mathbf{x}, \mathbf{x}'_S, \omega)$. The downgoing wavefield p_A^+ at the upper boundary $\partial\mathbb{D}_0$ is zero because of the reflection-free half-space above this boundary. In state B, the focusing function of the first type is substituted. At the lower boundary, it focuses downwards at the focal point $\mathbf{x}'_F$ such that $p_B^+ = \delta_H(\mathbf{x}_i - \mathbf{x}'_F)$. The medium is truncated so there is no reflection coming from below the boundary and therefore $p_B^- = f_1^-(\mathbf{x}, \mathbf{x}'_F, \omega) = 0$. At the upper boundary, the first type of focusing function is completely present such that $p_B^- = f_1^-(\mathbf{x}, \mathbf{x}'_F, \omega)$ and $p_B^+ = f_1^+(\mathbf{x}, \mathbf{x}'_F, \omega)$. These results are plugged into the reciprocity theorem of Eq. (2-4a) which results into:

$$\int_{\partial\mathbb{D}_0} f_1^+(\mathbf{x}, \mathbf{x}'_F, \omega) G^{-,+}(\mathbf{x}, \mathbf{x}'_S, \omega) d^2\mathbf{x} = G^{-,+}(\mathbf{x}'_F, \mathbf{x}'_S, \omega) \tag{2-67}$$

$G^{-,+}(\mathbf{x}'_F, \mathbf{x}'_S, \omega)$ in this case is the upgoing Green's function at depth as the result of a source at depth z_i. $G^{-,+}(\mathbf{x}, \mathbf{x}'_S, \omega)$ is the upgoing Green's function at the surface as the result of a source at depth. The latter can be rewritten using source-receiver reciprocity, meaning that the source and receiver positions can be exchanged while the result remains the same, resulting in the upgoing Green's function at depth as the result of a downgoing source at the surface. Thus when the source is located on the surface and all the waves are oriented downwards:

$$G^{-,+}(\mathbf{x}, \mathbf{x}'_S, \omega) = G^{-,+}(\mathbf{x}'_S, \mathbf{x}, \omega) \tag{2-68}$$

This is the upgoing Green's function retrieved by Eq. (2-35). This substitution can be used in Eq. (2-68):

$$\int_{\partial\mathbb{D}_0} f_1^+(\mathbf{x}, \mathbf{x}'_F, \omega) G^{-,+}(\mathbf{x}'_S, \mathbf{x}, \omega) d^2\mathbf{x} = G^{-,+}(\mathbf{x}'_F, \mathbf{x}'_S, \omega) \tag{2-69}$$

Finally the source and focal point are set to the same position $\mathbf{x}'_S = \mathbf{x}'_F$

$$\int_{\partial\mathbb{D}_0} f_1^+(\mathbf{x}, \mathbf{x}'_F, \omega) G^{-,+}(\mathbf{x}'_F, \mathbf{x}, \omega) d^2\mathbf{x} = G^{-,+}(\mathbf{x}'_F, \mathbf{x}'_F, \omega) \tag{2-70}$$

The focusing function and the upgoing Green's function can be recovered using the Marchenko scheme and be used to determine the upgoing response of the medium with respect to a downgoing source at the same position. It is similar to the reflection series that is defined by

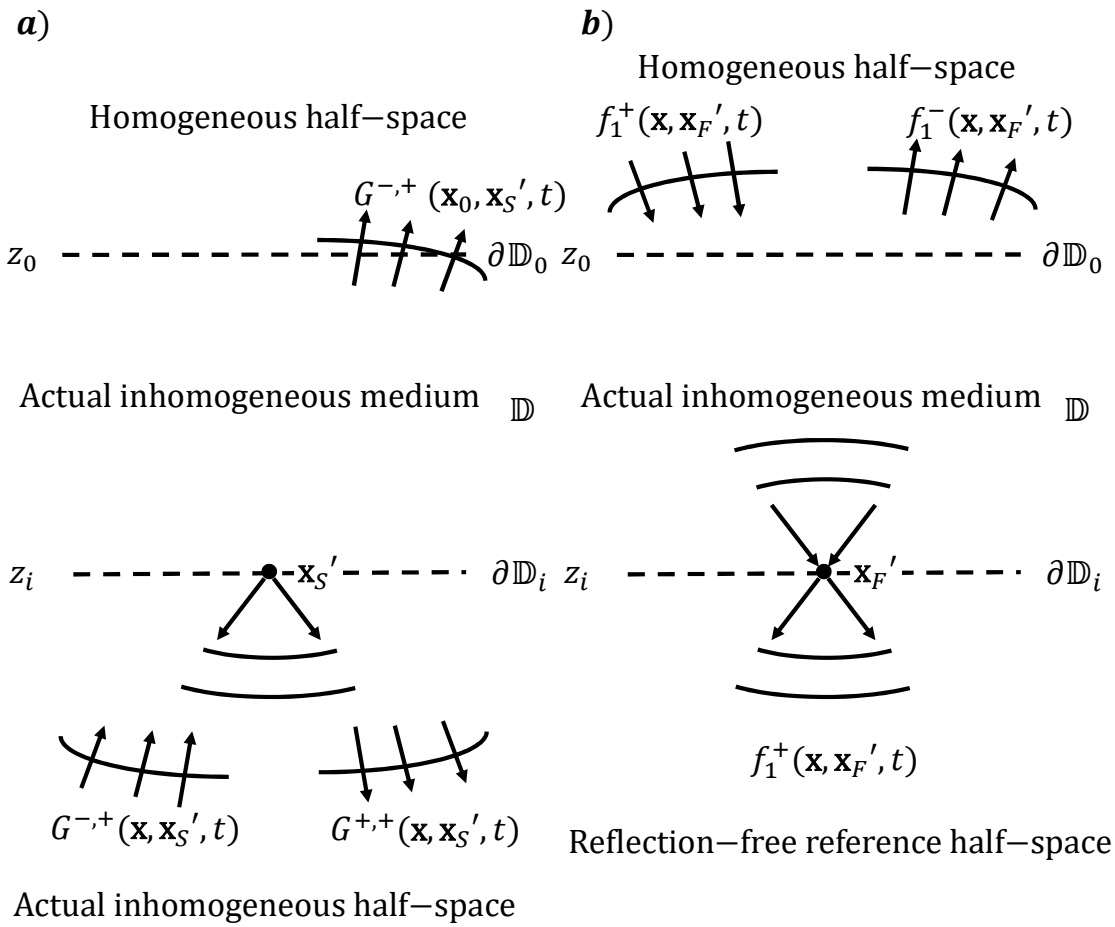

Figure 2-12: Two different states that can be used in the reciprocity theorems Eq. (2-4a) and (2-4b) (a) Physical medium containing all the reflections due to a simulated source at the focal depth z_i. (b) Truncated model with no reflection coming in from below depth z_i with a focal point at $\mathbf{x}_F'$. Modified after Wapenaar et al. (2014a).

Eq. (2-64) but defined by a different medium. R_0 is defined in a medium that is homogeneous above the focusing level and therefore no reflections are coming from above this level. $G^{-,+}$ in Eq. (2-70) is also operating at the same level, however the medium is the exact medium so reflections from above are still present. The difference with the upgoing Green's function $G^{-,+}(\mathbf{x}'_F, \mathbf{x}, \omega)$ is that in this case the source has been redatumed to the focal depth. This is the solution for the cost function problems that was presented in Figure 2-11. Because the physical medium is used, it is more likely that events will interfere with each other than if R_0 is used. However this happens only with very few events. Eq. (2-70) can be rewritten to 1D, where the integral becomes a simple multiplication

$$\hat{\hat{G}}^{-,+}(z_f, z_f, \omega) = \hat{f}_1^+(0, z_f, \omega)\hat{G}^{-,+}(z_f, 0, \omega) \tag{2-71}$$

Eq. (2-31) is used to write out a series for $\hat{f}_1^+$ in 1D. Similar to Eq. (2-56), the series can be written as a function of the scaling factors b and $a(z_f, b)$:

$$\hat{f}_1^+(0, z_f, t, b) = \sum_{k=0}^{\infty} \hat{v}_k^+(0, z_f, t)a(z_f, b)b^{2k} \tag{2-72}$$

The updates of the focusing function can be retrieved with a function similar to Eq. (2-58):

$$\hat{v}_k^+(0, z_f, t) = \left\{\Omega^k(z_f)\hat{W}\right\}(0, z_f, t) \tag{2-73}$$

By substituting these equations into Eq. (2-71) and by taking the first term of both series, the first term of the physical response $\hat{G}^{-,+}$ can be retrieved:

$$\hat{\hat{G}}_0^{-,+}(z_f, z_f, \omega, b) = \hat{U}_0^-(z_f, 0, \omega)exp(j\omega t_d(z_f))\hat{W}(\omega)a^2(z_f, b)b \tag{2-74}$$

This is actually the same equation as Eq. (2-65) with the exception of one extra wavelet applied. The wavelet can be removed with a deconvolution step, but this is not strictly necessary. A third cost function is proposed that is very similar to Eq. (2-66)

$$j_{III}(b) = \frac{\left|\hat{\hat{G}}^{-,+}(z_f, z_f, t, b)\right|_2}{\left|\hat{\hat{G}}_0^{-,+}(z_f, z_f, t, b)\right|_2} \tag{2-75}$$

This cost function contains more events, however it is computationally a lot faster and it does not require a deconvolution which is a nice feature. These properties are especially important when the higher order dimensions are considered.

2-4 Correction factor in 2D/3D

In this section the cost functions from the previous sections are extended to 2D and 3D. This section will be brief in comparison with the previous as a lot of observations are very similar. First the Green's function retrieval scheme is shown in the higher order dimensions with the correction factors included similar to Eq. (2-56) and (2-57) but expressed in the frequency domain

$$\hat{G}^{-,+}\left(\mathbf{x}'_F,\mathbf{x}_R,\omega,b\right)=\sum_{i=0}^{\infty}\hat{U}_i^{-}\left(\mathbf{x}'_F,\mathbf{x}_R,\omega\right)a\left(\mathbf{x}'_F,b\right)b^{1+2i} \tag{2-76}$$

$$\hat{G}_m^{+,+}\left(\mathbf{x}'_F,\mathbf{x}_R,\omega,b\right)=\sum_{j=0}^{\infty}\hat{U}_{m,j}^{+}\left(\mathbf{x}'_F,\mathbf{x}_R,\omega\right)a\left(\mathbf{x}'_F,b\right)b^{2(j+1)} \tag{2-77}$$

$$\hat{G}_d^{+,+}\left(\mathbf{x}'_F,\mathbf{x}_R,\omega,b\right)=\hat{f}_{1d}^{+*}\left(\mathbf{x}_R,\mathbf{x}'_F,\omega,b\right)+\sum_{k=0}^{\infty}\hat{U}_{d,k}^{+}\left(\mathbf{x}'_F,\mathbf{x}_R,\omega\right)a\left(\mathbf{x}'_F,b\right)b^{2(j+1)} \tag{2-78}$$

In this equation $\mathbf{x}'_F$ denotes a focal point somewhere in the medium and $\mathbf{x}_R$ is at a location on the acquisition surface where the reflection series is recorded. Depending on whether the medium is in 2D or 3D $\mathbf{x}=(x,z)$ or $\mathbf{x}=(x,y,z)$.

2-4-1 Scaling the first arrival

In higher order dimensions, the first arrival is not a single trace but rather an entire wave which is defined as $\hat{D}(\mathbf{x}_R,\mathbf{x}'_F,\omega)$. This arrival can be calculated from the velocity model and after scaling it is assumed to be related to the first arrival of $\hat{f}_{1d}^{+}$

$$\hat{f}_{1d}^{+}\left(\mathbf{x}_R,\mathbf{x}'_F,\omega,b\right)\approx a\left(\mathbf{x}'_F,b\right)\hat{D}(\mathbf{x}_R,\mathbf{x}'_F,\omega) \tag{2-79}$$

It should be pointed out that it is assumed that $a(\mathbf{x}'_F,b)$ is a scalar and not angle dependent. The impact of this assumption needs to be further examined when the cost functions are implemented in 2D and 3D. In the scope of this study only the scalar case is considered. In the future the idea might be extended to take into account these angle-dependent effects. The first arrival can be modeled using the wavelet $\hat{W}(\omega)$ that was used before. If this is done, then once again f_{1d}^{+} and $G_d^{+,+}$ are each others direct inverse which has the important fundamental property in higher order dimensions

$$\int_{\partial\mathbb{D}_0}\hat{G}_d^{+,+}\left(\mathbf{x}'_F,\mathbf{x}_R,\omega,b\right)\hat{f}_{1d}^{+}\left(\mathbf{x}_R,\mathbf{x}'_F,\omega,b\right)d^2\mathbf{x}_R=|\hat{W}(\omega)|^2 \tag{2-80}$$

The result of this property is the squared autospectrum of the wavelet, which is the result of the wavelets that are applied over both $\hat{G}_d^{+,+}$ and $\hat{f}_{1d}^{+}$. When Eq. (2-78) and (2-79) are substituted into Eq. (2-80) the scaling factor $a(\mathbf{x}'_F,b)$ can be found

$$\hat{\hat{t}}_L(\mathbf{x}'_F,\omega)a^2(\mathbf{x}'_F,b)=|\hat{W}(\omega)|^2 \tag{2-81}$$

where

$$\begin{aligned}\hat{\hat{t}}_L(\mathbf{x}'_F,\omega)=&\int_{\partial\mathbb{D}_0}\hat{D}^*\left(\mathbf{x}_R,\mathbf{x}'_F,\omega,b\right)\hat{D}\left(\mathbf{x}_R,\mathbf{x}'_F,\omega,b\right)d^2\mathbf{x}_R+\\&\int_{\partial\mathbb{D}_0}\sum_{k=0}^{\infty}\hat{U}^+_{d,k}\left(\mathbf{x}'_F,\mathbf{x}_R,\omega\right)b^{2(j+1)}\hat{D}\left(\mathbf{x}_R,\mathbf{x}'_F,\omega,b\right)d^2\mathbf{x}_R\end{aligned} \tag{2-82}$$

Then by rewriting Eq. (2-81) the scaling factor for higher order dimensions is given as

$$a(\mathbf{x}'_F,b)=\sqrt{\left|\frac{|\hat{W}(\omega)|^2}{\hat{\hat{t}}_L(\mathbf{x}'_F,\omega)}\right|} \tag{2-83}$$

2-4-2 Cost functions

The first type of cost function that only uses redatuming at the receiver side is the same as the one found in Eq. (2-60) with the exception that the Green's functions are evaluated in higher order dimensions according to Eq. (2-76)

$$J_I\left(b\right)=\frac{|G^{-,+}\left(\mathbf{x}'_F,\mathbf{x}_R,\omega,b\right)|_2}{|G_0^{-,+}\left(\mathbf{x}'_F,\mathbf{x}_R,\omega,b\right)|_2}, \tag{2-84}$$

where

$$\hat{G}_0^{-,+}\left(\mathbf{x}'_F,\mathbf{x}_R,\omega,b\right)=\hat{U}_0^-\left(\mathbf{x}'_F,\mathbf{x}_R,\omega\right)a\left(\mathbf{x}'_F,b\right) \tag{2-85}$$

The J_I indicates that the cost function is in either 2D or 3D and j_I indicates it is in 1D. This is again a cost function that only works well below the deepest reflector. Thus the other cost functions are required to account for reflectors below the focal point. A 2D/3D expansion of the second type of cost function j_{II} would be most robust, however it is very computationally expensive. As explained before this would require an integral over the focal points to be applied several times resulting in very high memory cost. Thus the third type of focusing function j_{III} is extended to the higher order dimensions instead. For this reason Eq. (2-70) is repeated which is already in the higher dimensions

$$\hat{\hat{G}}^{-,+}(\mathbf{x}'_F,\mathbf{x}'_F,\omega)=\int_{\partial\mathbb{D}_0}\hat{f}_1^+(\mathbf{x},\mathbf{x}'_F,\omega)\hat{G}^{-,+}(\mathbf{x}'_F,\mathbf{x},\omega)d^2\mathbf{x} \tag{2-86}$$

and the first term of the series in Eq. (2-86) can be obtained by using the first terms of $\hat{G}^{-,+}$ and $\hat{f}_1^+$:

$$\hat{\tilde{G}}_0^{-,+}(\mathbf{x}'_F, \mathbf{x}'_F, \omega) = \int_{\partial\mathbb{D}_0} \hat{D}\left(\mathbf{x}, \mathbf{x}'_F, \omega, b\right) a^2(\mathbf{x}'_F, b) b \hat{U}_0^-\left(\mathbf{x}'_F, \mathbf{x}, \omega\right) d^2\mathbf{x} \tag{2-87}$$

Finally the following cost function can be defined in 2D and 3D:

$$J_{III}(b) = \frac{\left|\hat{\tilde{G}}^{-,+}(\mathbf{x}'_F, \mathbf{x}'_F, t)\right|_2}{\left|\hat{\tilde{G}}_0^{-,+}(\mathbf{x}'_F, \mathbf{x}'_F, t)\right|_2} \tag{2-88}$$

This cost function is able to handle focal positions that are located above the deepest reflector in higher order dimensions. In the following chapter its behavior and that of the other cost functions will be demonstrated.

Chapter 3

Cost function results in 1D

This chapter will focus mainly on the results achieved by the cost functions and the reasons why the cost functions do or do not function properly. Several different models have been tested with the cost functions. All of these models have the free-surface multiples removed from the data, which is a requirement for the scheme that has been developed here. The first model that is used is the model in Table A-1. This is a simple model with strong reflectors throughout the entire model and a constant velocity. Variations of this model have also been tested and unless noted otherwise the results are similar to the results from this model. The weak model in Table A-2 is very similar to the simple model, but the lowest reflector has a much weaker contrast than the reflectors above it. And finally the artifact model from Table A-3 is considered. This model has been specifically developed to have overlapping reflection events, which will disrupt the calculation of the cost functions. In Figure 3-1 the reflection series for all of the models are shown, which were generated with a Ricker wavelet of 30 Hz. The reflection series in Figure 3-1 (a) and (b) have the same arrival times. In Figure 3-1 (b), later events have much weaker amplitudes than the latet events in Figure 3-1 (a), to the point where they are no longer visible on the trace anymore. The reflection series in Figure 3-1 (c) for the artifact model has regular intervals between all the events.

3-1 Scaling of the first arrival

First, the scaling of the first arrival is considered in order to account for transmission losses. As seen in the previous chapter, the phase of the first arrival is modeled from the velocity model and its amplitude is set to 1. While it is not impossible that this is the actual amplitude of the first arrival, it is highly unlikely. The only case where this is possible is if there are no reflectors present in the overburden, so that there are no transmission losses. Using Eq. (2-55) the transmission losses can be compensated for, in case the correct source strength $q = 1$ is known or the correction factor b has been applied. In Figure 3-2 $a(z_f)$ has been plotted for all three of the models, with the layer contrast locations indicated in green. For every model, the scaling factor starts out at a value of 1. This is because in this modeling only transmission

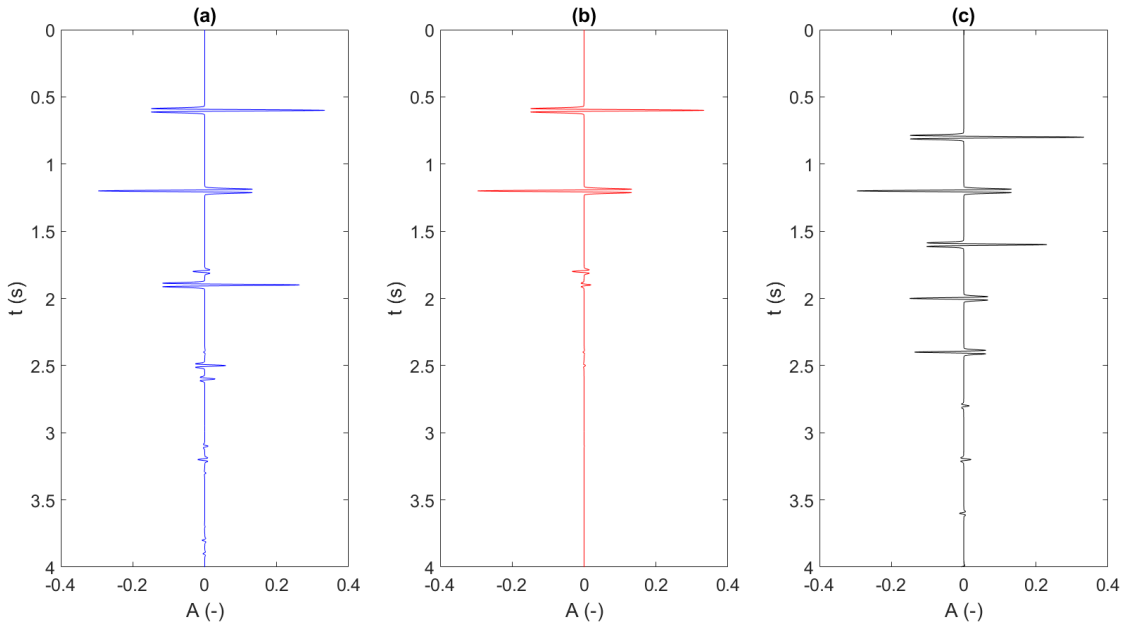

Figure 3-1: Reflection series without surface multiples retrieved at the surface for (a) the simple model in Table A-1, (b) the weak model in Table A-2 and (c) the artifact model in Table A-3. All of these series have been generated with a 30 Hz Ricker wavelet.

losses due to the reflectors are considered and the medium itself is considered to be lossless. At deeper depths, below boundaries, the factor increases in strength to account for the losses from transmission of one layer to the next. In Figure 3-2 (b) the final contrast is very weak so the value of $a(z_f)$ does not change much. At the depth of a layer contrast, the factor starts to behave erratically and takes a strong dip. This can be explained by the plots in Figure 3-3. In Figure 3-3 (a), the modeled first arrival and time gate truncation times are correct and do not interfere with each other, but in Figure 3-3 (b) where the convolution of the reflection series and the first arrival is shown the time gate truncation times overlies part of the event. When the muting is applied, part of this event will be preserved and another part will be muted out. Thus, an incomplete signal is left which causes problems when further convolutions are applied which is visible in Figure 3-3 (c). Here the muted signal from Figure 3-3 (b) has been convolved with the time-reversed reflection series. The events are not complete pulses but rather parts of it, which will cause incorrect values for $a(z_f)$. In order to prevent this from occurring the truncation times of Θ can be shifted to avoid overlap with the events. In case there is an overlap, the limits is shifted both backwards and forwards and the value for $a(z_f)$ above and below the layer contrast are both determined. Depending on the shift that was needed, a transition value is calculated using a cosine function. After applying this methodology, the result of Figure 3-2 is improved to that in Figure 3-4. In this figure the transition is less erratic. The final change in $a(z_f)$ for the weak model in Figure 3-4 (b) is not noticeable on this scale. Applying this methodology has removed the erratic behavior from the jumps. Going forward this methodology will be applied to $a(z_f)$ whenever it is located near a layer contrast.

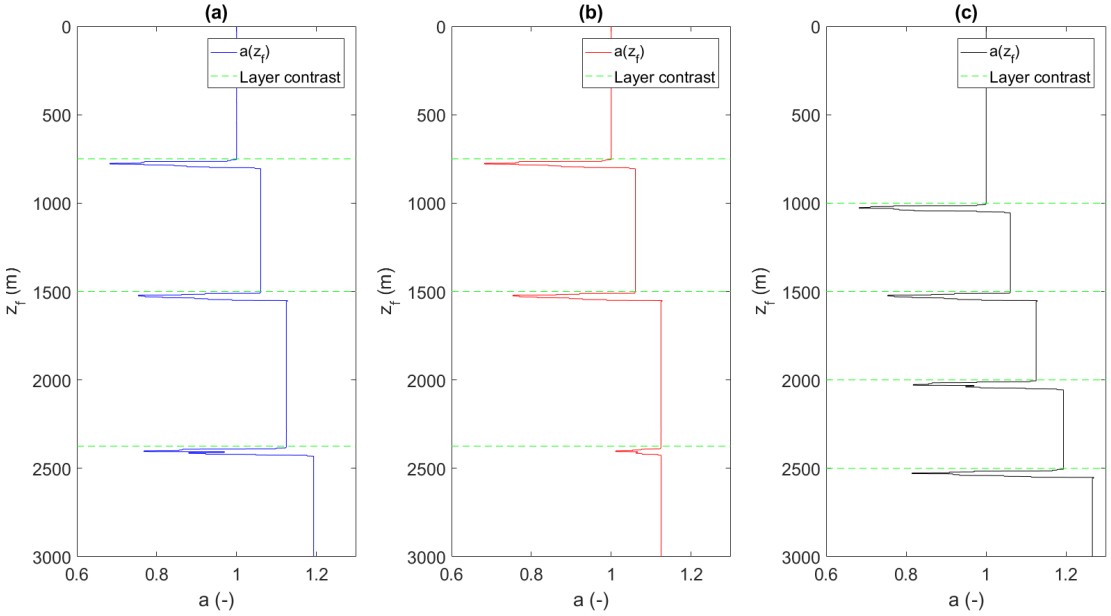

Figure 3-2: Scaling factor $a(z_f)$ for the transmission losses at every 1 meter depth for (a) the simple model in Table A-1, (b) the weak model in Table A-2 and (c) the artifact model in Table A-3. The locations of the layer contrasts have been indicated in dashed green.

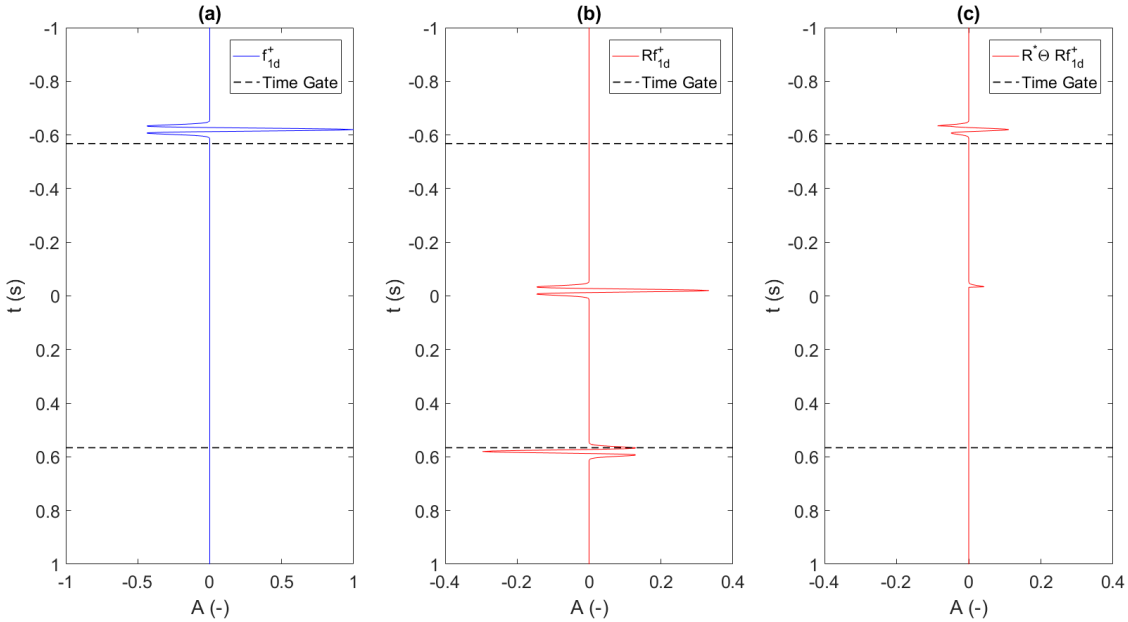

Figure 3-3: (a) Modeled first arrival of the downgoing focusing function of the first type. (b) Convolution of the reflection series and the trace in (a). (c) Convolution of the time-reversed reflection series with the events in (b) after the muting window Θ has been applied. All of these events were generated using the simple model in Table A-1 at a focal depth of 1520 meters using a 30 Hz Ricker wavelet. The time gate truncation times are indicated in dashed black. Note that the time gate truncation time is overlying part of an event in (b) and that the events in (c) are distorted.

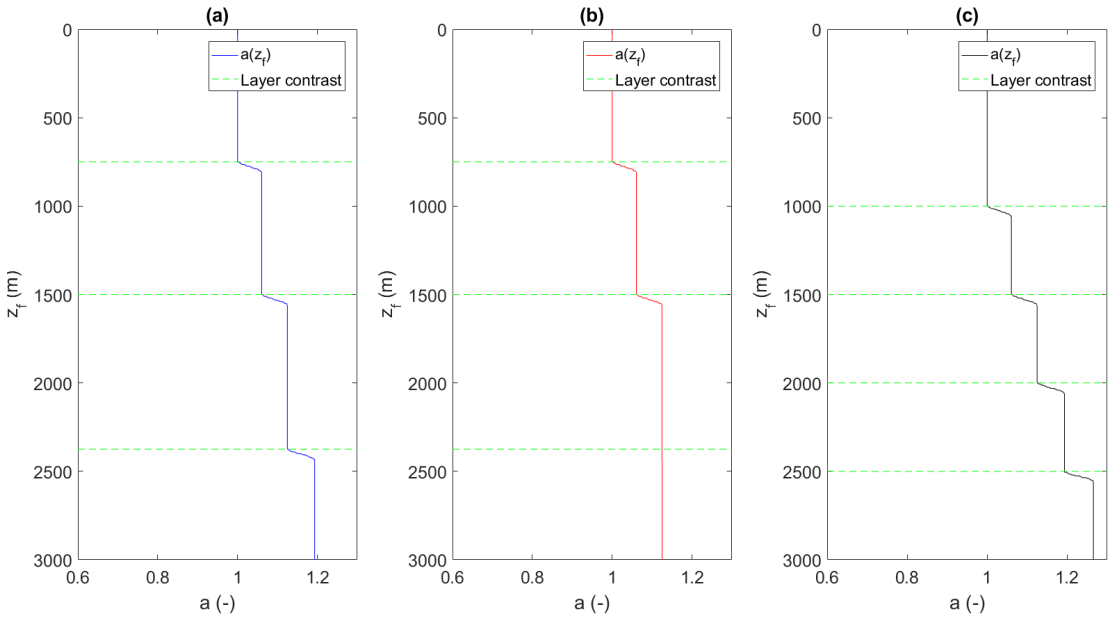

Figure 3-4: Scaling factor $a(z_f)$ for the transmission losses at every 1 meter depth for (a) the simple model in Table A-1, (b) the weak model in Table A-2 and (c) the artifact model in Table A-3. The transition over layer contrasts is smoothed using a cosine function. The locations of the layer contrasts have been indicated in dashed green.

3-2 Single-sided redatuming cost function

The cost function j_I from Eq. (2-60) is considered first. The simplest situation in which every cost function should work is when the focal point is located below the deepest reflector in a medium. The simple model from Table A-1 is considered first and a focal depth of 2700 meters is used to avoid any problems with the interference of events. The value of q is set to 1 so that the reflection series is correct and the value that should be recovered for b is also 1. Figure 3-5 shows that in this case the minimum has a very strong dip and recovers the correct value of $b = 1$ for the blue line. This strong dip is due to the fact that the upgoing Green's function below the deepest reflector should be zero so the difference between the initial and final estimation is very strong. The strong dip around the correct value for b is also because of this. In case b is incorrect, there will be events in the final trace instead of the empty trace. This contrast is much weaker and therefore the cost increases quickly. In case the reflection series has been scaled incorrectly, the minimum is also found at the correct value for b. The minima are comparable to the one found for $q = 1$, again because the upgoing Green's function should be zero. The values for the cost are equal or less to 1 or when the value of b is too low. This is due to the fact that the weaker the reflection series, the less amount of energy is removed from the initial estimation. So if the value for b is very low, almost nothing is removed and the cost function approaches the value of 1. This can be seen in Figure 3-6, where the solid blue line indicates the correct value for b and the final estimation of the upgoing Green's function in Figure 3-6 (c) is indeed zero here. Each of the lines in this figure has been normalized with the L_2-norm of the initial trace i.e. $|G_0^{-,+}|_2$. This is the same normalization that is used for the cost function and ensures that all the initial estimates are equal. This makes it easier to distinguish what effect incorrect updates have. The dashed red

line in Figure 3-6 shows what happens if the value for b is too low. The updates are much weaker than those for the correct value for b as can be seen in Figure 3-6 (b) and therefore the difference between the final and initial estimation is much smaller, resulting in a higher cost. The L_2-norm uses squares so calculating the cost always results in a positive value. The cost decreases when the value of b goes from too low to the correct value and increases again when the value of b increases. This can be gathered from the dotted black lines in Figure 3-6 where the correction factor for b is too high and therefore the updates are too strong, so they do not remove the events but rather flip the polarity. Because of the squares in the L_2-norm the polarity does not matter and the final value for the cost is positive. In case the value for b is set even higher more energy is added to the events with reversed polarity, which causes the energy in the final estimation to greatly increase. This energy can become greater than that of the original estimate, which is why the value of the cost becomes greater than 1. Figure 3-7 shows the results for the weak model and Figure 3-8 does this for the artifact model. For both models the correct values for b are recovered and the shape of the cost curve is similar to that of the cost curve for the simple model. There are some differences in the value of the cost. Figure 3-7 has an even lower value of the minimum for the weak model and the slope of the cost for higher b is more gentle, while the artifact model has a much higher minimum as Figure 3-8 shows and has a much steeper slope for higher values of b. This is just a model dependent difference and not a fundamental property of the cost function. All of the models do have a clear minimum at the correct values, which is the desired result.

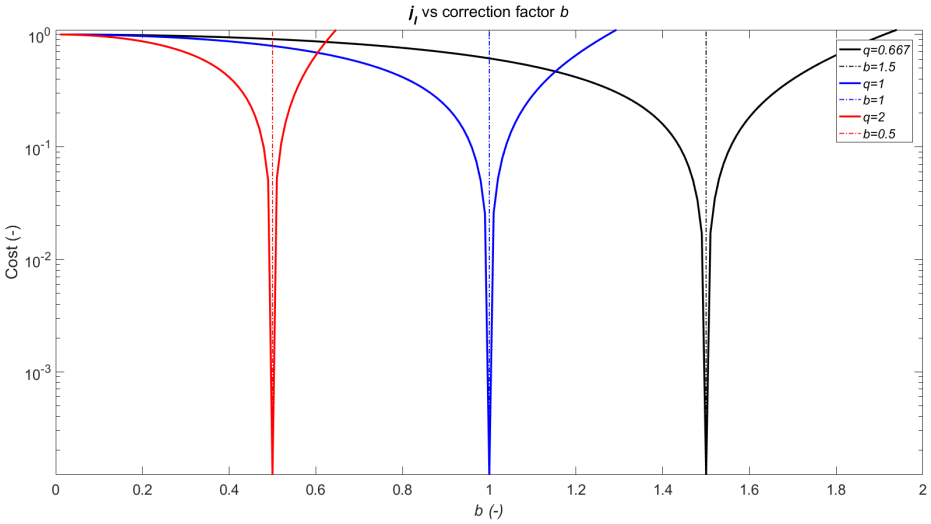

Figure 3-5: Cost function j_I using Eq. (2-60) for the simple model in Table A-1 at a focal depth of 2700 meters with a source strength q of (black) $\frac{2}{3}$, (blue) 1 and (red) 2. The location of the correct value of b is indicated by the close-dashed vertical lines. The y-axis is logarithmic.

In case there are reflectors present below the focal point, the upgoing Green's function is not equal to zero, so potential problems can arise. The focal depth is changed to a depth of 2200 meters, which for all three of the models is above the deepest reflector. The simple model is considered first and the result is shown in Figure 3-9. In this case, incorrect values for b are recovered by a significant margin as the minimum of the curves are clearly at a different location than the correct values indicated by the vertical lines. As explained in the

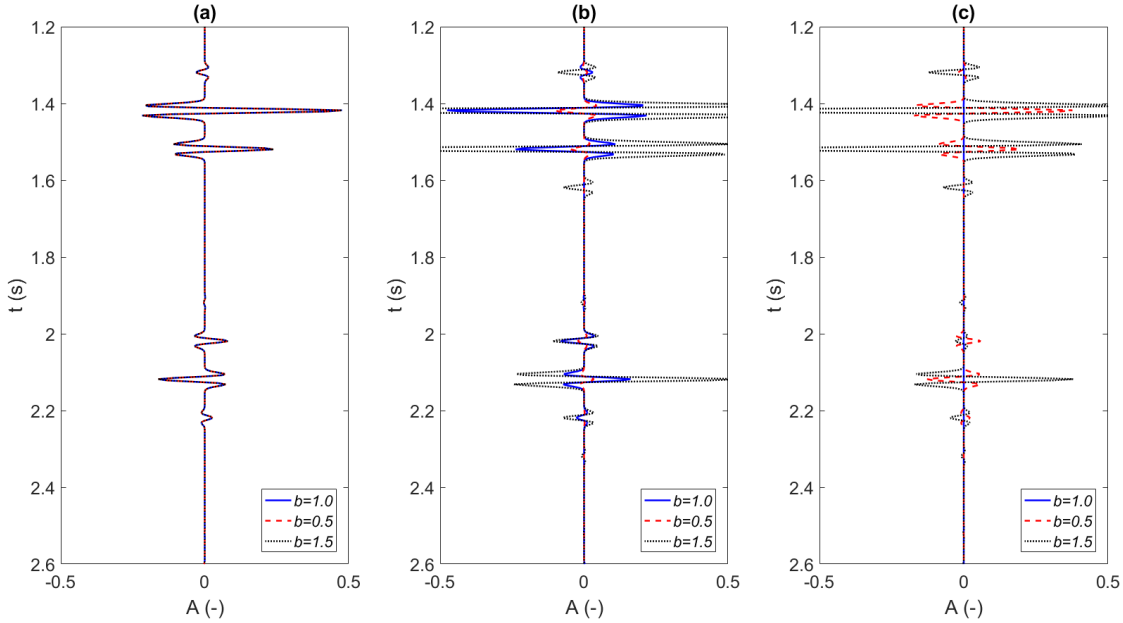

Figure 3-6: (a) Initial estimation of the upgoing Green's function, (b) updates of the upgoing Green's function and (c) final upgoing Green's function after 8 iterations for a correction factor b of (solid blue) 1, (dashed red) 0.5 and (dotted black) 1.5. All events are based on the model found inTable A-1 and have been convolved with a 30 Hz Ricker wavelet with a focal depth of 2700 m and have been normalized with $|G_0^{-,+}|_2$ of the relevant reflection series.

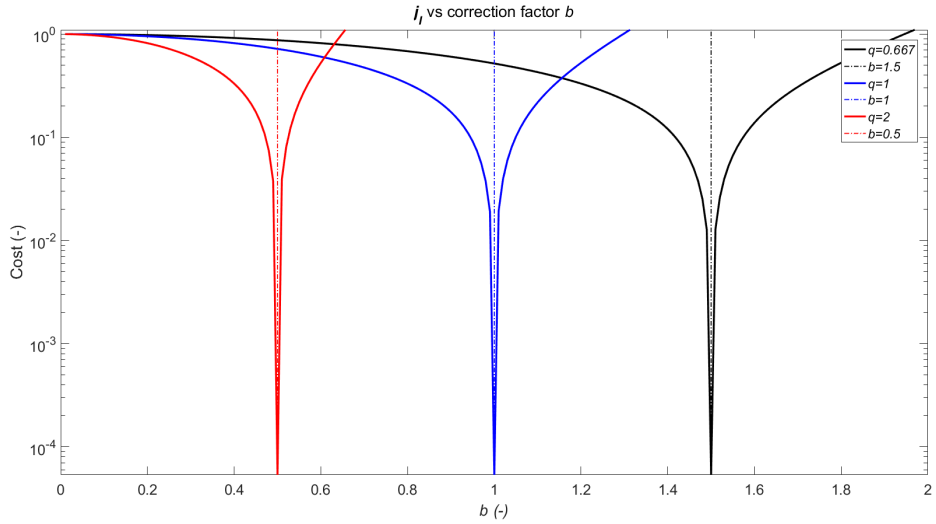

Figure 3-7: Cost function j_I using Eq. (2-60) for the weak model in Table A-2 at a focal depth of 2700 meters with a source strength q of (black) $\frac{2}{3}$, (blue) 1 and (red) 2. The location of the correct value of b is indicated by the close-dashed vertical lines. The y-axis is logarithmic.

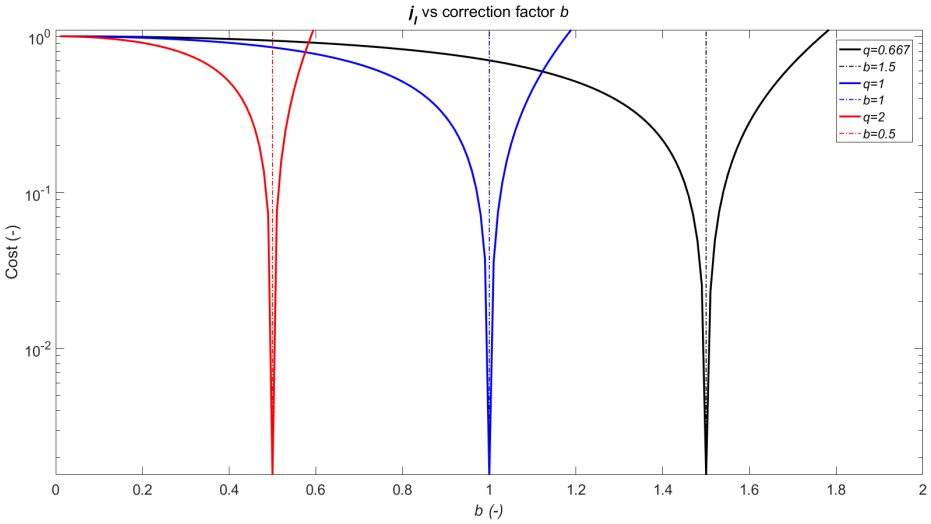

Figure 3-8: Cost function j_I using Eq. (2-60) for the artifact model in Table A-3 at a focal depth of 2700 meters with a source strength q of (black) $\frac{2}{3}$, (blue) 1 and (red) 2. The location of the correct value of b is indicated by the close-dashed vertical lines. The y-axis is logarithmic.

previous chapter, the cost function j_I is not good at handling strong reflectors below the focal point. The reason for this, as explained in Figure 2-7 and Figure 2-11, is that physical events overlap in time with the events that will create artifacts and the updates cannot separate these events. Figure 3-10 shows the upgoing Green's function for a source strength of $q = 1$ (which corresponds to the blue line from Figure 3-9). The dashed red line is the correct value for b and does remove the artifacts. A value of 1.2 used for b is very close to the actual minimum that was found, but it does still contain incorrect events. There is very little difference between the two lines, with some very subtle differences that can be found in Figure 3-10 (c), this is also visible in Figure 3-9. The value of the minimum is very close to 1 and can only be made apparent by using a logarithmic scale. This is due to the fact that the internal multiples that are muted have very weak amplitudes compared to the stronger reflections as can be seen in Figure 3-10. The curve itself is also much smoother. Because of these small differences, the cost function has its minimum at the wrong value of b. These differences are caused by two things. The fact that an artifact and physical event overlap and the overlap of higher-order multiples with lower-order multiples. In the first case, as demonstrated by the events in Figure 2-7, one artifact is removed from the initial estimation and one physical event remains. However, if the source strength is estimated too high, the amplitude of the update that should only remove the artifact also removes the physical event. In case this happens for multiple events the final trace contains less energy for a too high value of b than in case the correct value of b is used. An example of this can be seen in Figure 3-10 at around $1.6s$. The effect of this can be seen in Figure 3-9, which clearly shows that in every case b is estimated too high, not too low. The second case is demonstrated by the events in Figure 2-8. The higher-order multiples have the opposite polarity of the lower-order multiples and they overlap in time. When one of these higher-order multiples is an artifact and is removed, it causes the amplitude of the combined event to go up, because this event does not oppose the amplitude of the lower-order multiple. Because these effects are caused by different-order multiples, the

impact is much weaker than the first problem. An example of this problem is the event at $2.3s$ in Figure 3-10. These problems do not mean that j_I does not work at all for reflectors below the focal point. In case the reflectors are very weak such as for the weak model in Table A-2 the function does recover acceptable values for b as can be seen in Figure 3-11. The minima are still less pronounced and the curves are more smooth compared to the case when the focal point is located below the deepest reflector. Figure 3-12 shows that in case of a very weak low reflector, most of the events become so weak that they do not significantly contribute anymore. The reason for these small amplitudes is that the multiples lose more energy every time they hit this weak reflector. The problematic events are still present but their impact is much weaker and the cost function is more accurate. However, the method will never work as well as the case that the focal point is located below the deepest reflector. In case of the artifact model in Table A-3 the function clearly does not work. In this case not only do physical events overlap with artifacts, they also overlap with other physical events. From these results, it can be concluded that while the first cost function j_I does work if the focal point is located above the deepest reflector in case of a general model like the simple model from Table A-1. The cost function is not as robust as one would desire. In case of a model like the artifact model from Table A-3, it is better not to apply the Marchenko scheme if the source strength is unknown. The results of the cost function prove as much as the value of b is indicated to be 0 which would not apply any updates. This states that in this case one should not apply the Marchenko method at all and in case the reflection series is assumed to be scaled incorrectly this is actually good advice. The result states that in this case it would be better to apply conventional methods.

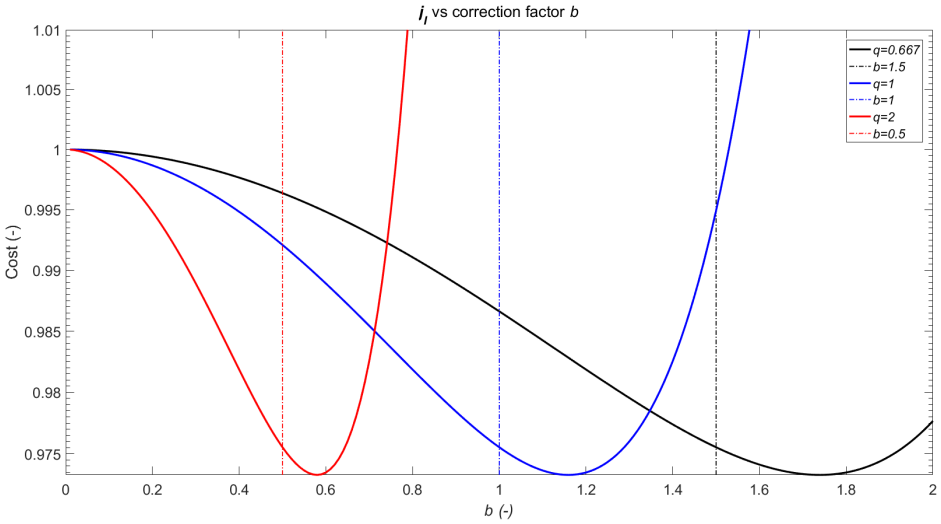

Figure 3-9: Cost function j_I using Eq. (2-60) for the simple model in Table A-1 at a focal depth of 2200 meters with a source strength q of (black) $\frac{2}{3}$, (blue) 1 and (red) 2. The location of the correct value of b is indicated by the close-dashed vertical lines. The y-axis is logarithmic.

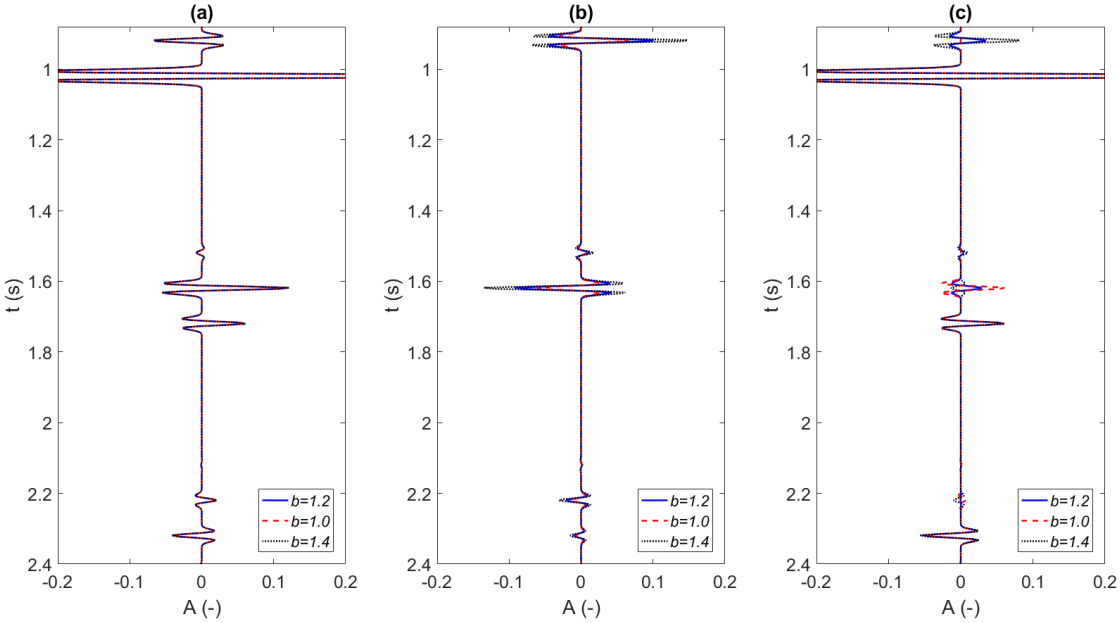

Figure 3-10: (a) Initial estimation of the upgoing Green's function, (b) updates of the upgoing Green's function and (c) final upgoing Green's function after 8 iterations for a correction factor b of (solid blue) 1.2, (dashed red) 1.0 and (dotted black) 1.4. All events are based on the model found inTable A-1 and have been convolved with a 30 Hz Ricker wavelet with a focal depth of 2200 m and have been normalized with $|G_0^{-,+}|_2$ of the relevant reflection series.

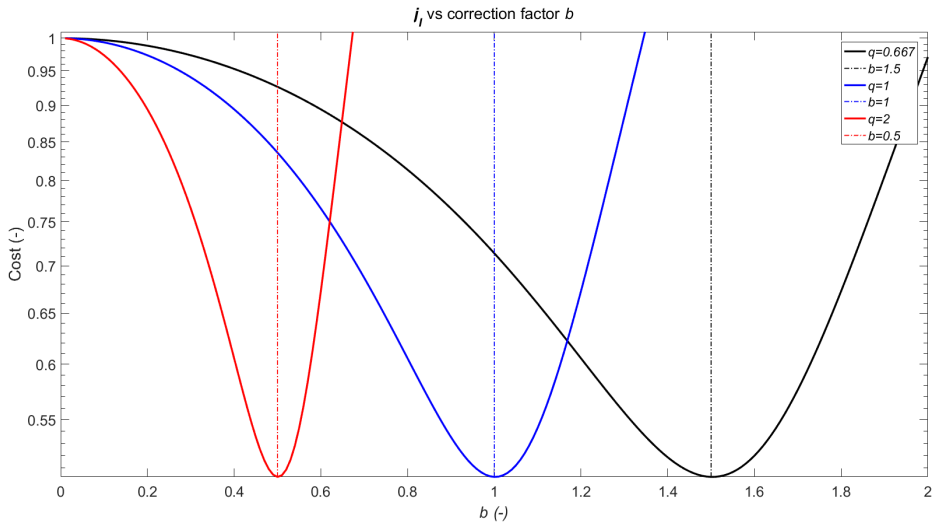

Figure 3-11: Cost function j_I using Eq. (2-60) for the weak model in Table A-2 at a focal depth of 2200 meters with a source strength q of (black) $\frac{2}{3}$, (blue) 1 and (red) 2. The location of the correct value of b is indicated by the close-dashed vertical lines. The y-axis is logarithmic.

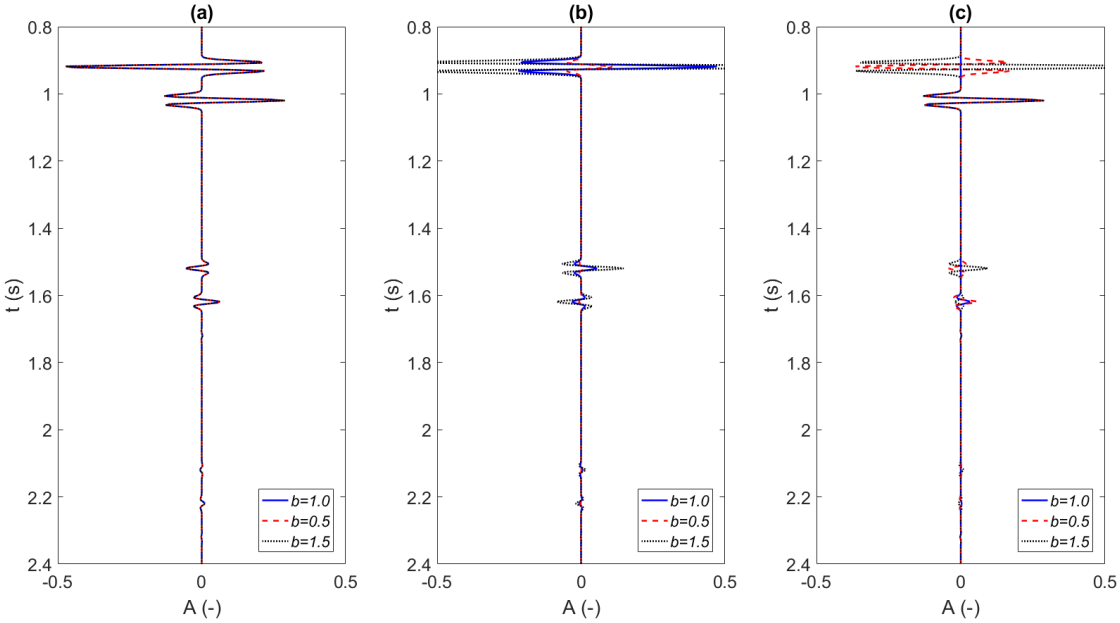

Figure 3-12: (a) Initial estimation of the upgoing Green's function, (b) updates of the upgoing Green's function and (c) final upgoing Green's function after 8 iterations for a correction factor b of (solid blue) 1.0, (dashed red) 0.5 and (dotted black) 1.5. All events are based on the model found inTable A-2 and have been convolved with a 30 Hz Ricker wavelet with a focal depth of 2200 m and have been normalized with $|G_0^{-,+}|_2$ of the relevant reflection series.

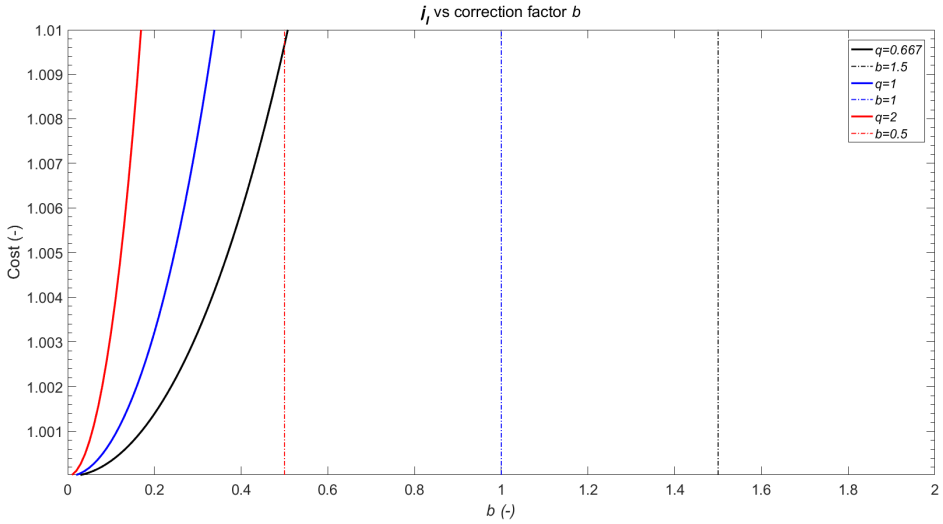

Figure 3-13: Cost function j_I using Eq. (2-60) for the artifact model in Table A-3 at a focal depth of 2200 meters with a source strength q of (black) $\frac{2}{3}$, (blue) 1 and (red) 2. The location of the correct value of b is indicated by the close-dashed vertical lines. The y-axis is logarithmic.

3-3 Double-sided redatuming cost function

In this section, the second cost function j_{II} from Eq. (2-66) is considered. This cost function should be able to improve upon the results of the first cost function j_I for the simple model. In case of the artifact model from Table A-3, the same problems are to be expected. Figure 3-14 shows the results in case the focal point is located below the focal point for the second cost function, similarly as how Figure 3-5 did this for the first cost function. The results are similar to the ones found for the first cost function. The differences are due to the fact that in this case the energy of the truncated reflection series is minimized while for the first cost function the energy of the upgoing Green's function was minimized. When studying Figure 3-15 (a) the initial estimation contains incorrect events that all need to be removed. These estimates have been normalized with the L_2-norm of the first estimate of the truncated reflection series $|R_{0,0}|_2$. This is done to make the comparison between the different scaling factors easier to interpret. When the correct value for b is used, the updates remove these events and the result is an empty trace. In case of an incorrect value of b, the updates behave similar for the truncated reflection series to those of the upgoing Green's function. As mentioned before the upgoing Green's function has an initial estimate, which contains all the physical events and artifacts. Subsequent updates remove the artifacts. The downgoing Green's function contains a single first arrival initially and subsequent updates add the other physical events and adjust the amplitude of the first arrival. The use of this updated downgoing Green's function helps to remove the artifacts present in the truncated reflection series. In case the acquired reflection series has been scaled too weakly, the amplitude of these events will be too weak. In case the acquired reflection series is scaled too strong, the amplitudes of the updates will be too strong. Because the truncated reflection series is retrieved by a frequency domain multiplication of the upgoing and downgoing Green's function, both of these behaviors are affecting the final result. Especially in case the value used for b is too large, a lot of artifacts are enhanced which clearly distort the final result. The results for the weak and artifact model for the second cost function in Figure 3-16 and Figure 3-17 are also very similar to those for the first cost function in Figure 3-7 and Figure 3-8. This shows that the second type of cost function is as robust for focal points below the deepest reflector as the first type of cost function for all of the models.

The second cost function should be able to handle the problems that the first cost function has if the focal point is located above the deepest reflector. It is applied to the simple model at a focal depth of 2200 meters and the results are shown in Figure 3-18. The minimum is not very pronounced and the cost function is smoother than if the focal point is located below the deepest reflector. However the cost function does find the correct values of b for each of the incorrect source strengths q. This is an improvement over the first cost function and makes the application of this cost function more effective. This is the first cost function that does not require all events to be removed from the initial estimation as is shown in Figure 3-19. In case b is underestimated, these events are not removed, although the physical event is estimated at the correct value. In case b is overestimated, the truncated reflection series introduces a lot of very strong artifacts. However the physical event is still estimated correctly. The weak model produces similar results in Figure 3-20 but with stronger minima. The second cost function also works for this model and is not inferior to the first cost function. Finally the artifact model in Figure 3-21 does not produce the correct results. This is due to the unavoidable overlap of events in time which makes the construction of the truncated reflection response different. This can be seen in Figure 3-22 (a) where the events are at regular intervals. There

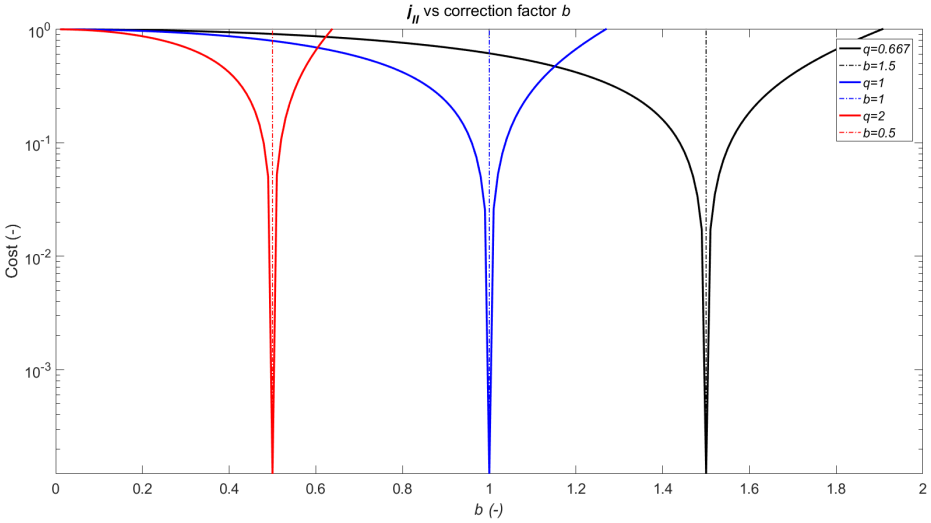

Figure 3-14: Cost function j_{II} using Eq. (2-66) for the simple model in Table A-1 at a focal depth of 2700 meters with a source strength q of (black) $\frac{2}{3}$, (blue) 1 and (red) 2. The location of the correct value of b is indicated by the close-dashed vertical lines. The y-axis is logarithmic.

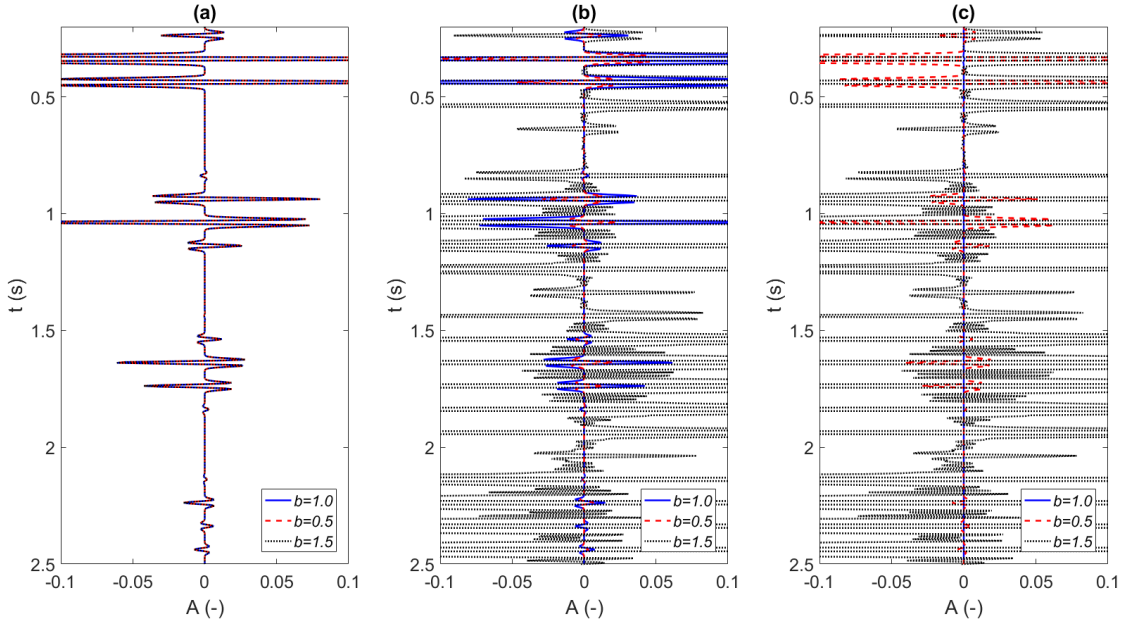

Figure 3-15: (a) Initial estimation of the truncated reflection series, (b) updates of the truncated reflection series and (c) final truncated reflection series after 8 iterations for a correction factor b of (solid blue) 1, (dashed red) 0.5 and (dotted black) 1.5. All events are based on the model found inTable A-1 and have been convolved with a 30 Hz Ricker wavelet with a focal depth of 2700 m and have been normalized with $|R_{0,0}|_2$ of the relevant reflection series.

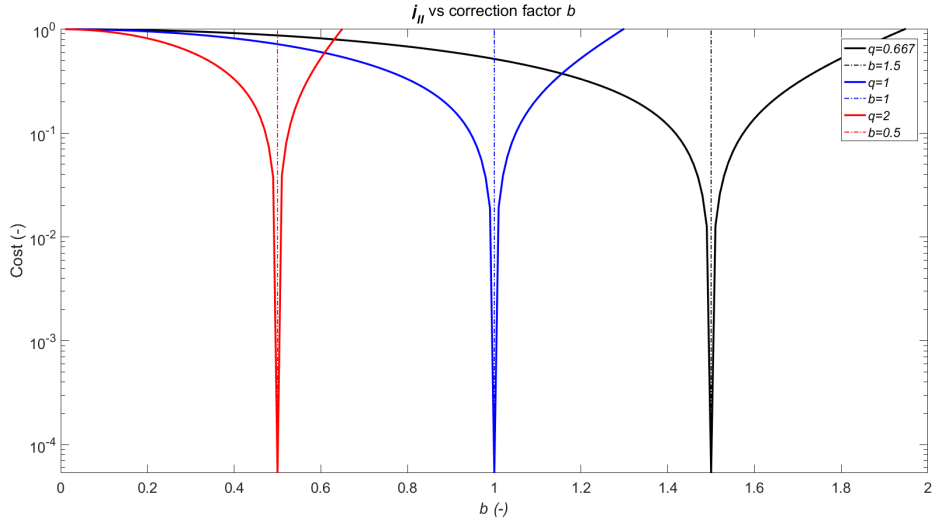

Figure 3-16: Cost function j_{II} using Eq. (2-66) for the weak model in Table A-2 at a focal depth of 2700 meters with a source strength q of (black) $\frac{2}{3}$, (blue) 1 and (red) 2. The location of the correct value of b is indicated by the close-dashed vertical lines. The y-axis is logarithmic.

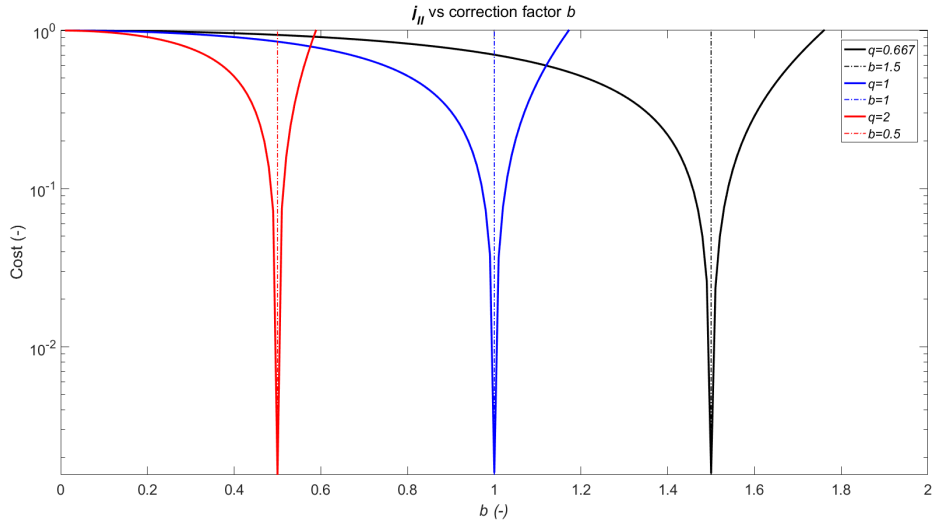

Figure 3-17: Cost function j_{II} using Eq. (2-66) for the artifact model in Table A-3 at a focal depth of 2700 meters with a source strength q of (black) $\frac{2}{3}$, (blue) 1 and (red) 2. The location of the correct value of b is indicated by the close-dashed vertical lines. The y-axis is logarithmic.

are also multiples overlapping with physical primaries and other multiples. Thus when updates are applied to these events they either increase or decrease the amplitude. A good example of this is the first event that gets a very strong update, that increases the amplitude in case of the correct value of b. If b is estimated too low, this update is much weaker and as such the cost function value will be lower. The updates are still correct but it is no longer minimizing the trace because of the interfering events. As a result, for the correct value of b, the energy in the trace can be higher than for the correct b because the physical events are no longer dampened by artifacts that have the opposite polarity. This is similar to the reason that the first cost function does not work above the deepest reflector: The overlap of artifacts and physical events. However, in case of the artifact model this is a fundamental problem that cannot be solved by the second cost function. A reflection series with a lot of overlapping events is therefore very hard to tackle using the cost functions, unless the focal point is below the deepest reflector. In case the source strength q is not known for such a model, it is best not to apply the Marchenko scheme or to determine the source strength in a different way. It should be noted that conditions like this are very unlikely to occur in real media.

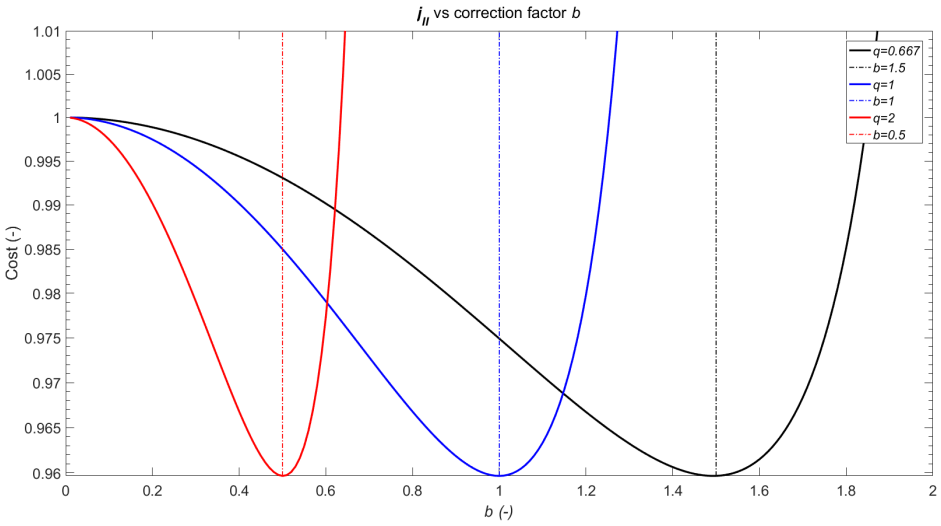

Figure 3-18: Cost function j_{II} using Eq. (2-66) for the simple model in Table A-1 at a focal depth of 2200 meters with a source strength q of (black) $\frac{2}{3}$, (blue) 1 and (red) 2. The location of the correct value of b is indicated by the close-dashed vertical lines. The y-axis is logarithmic.

3-4 Alternative double-sided redatuming cost function

The third cost function j_{III} from Eq. (2-75) is similar to the second cost function j_{II} in the way that it can handle reflectors below the focal point. It is not as computationally intensive as the second cost function. In 1D this is not a real problem but the computational cost increases greatly in 2D and 3D. First and foremost, the focal point below the deepest reflector is considered. As Figure 3-23, Figure 3-24 and Figure 3-25 show, the result is very similar to the ones found for the previous two cost functions. The minimum is found with a very strong dip at the correct value of b. This shows that for every cost function the correct value

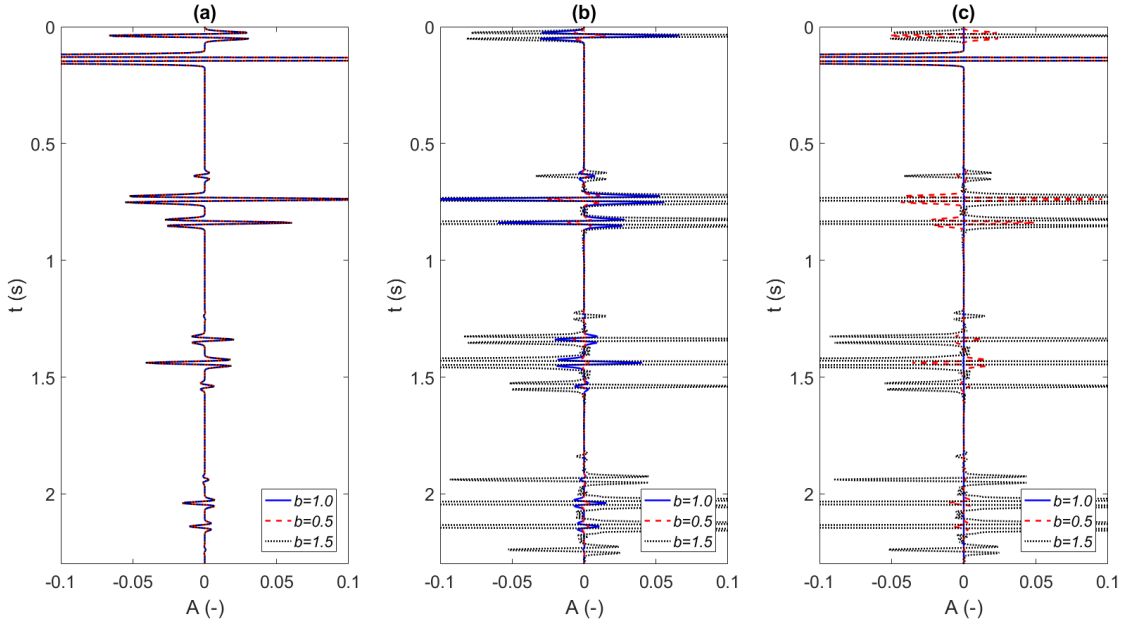

Figure 3-19: (a) Initial estimation of the truncated reflection series, (b) updates of the truncated reflection series and (c) final truncated reflection series after 8 iterations for a correction factor b of (solid blue) 1, (dashed red) 0.5 and (dotted black) 1.5. All events are based on the model found inTable A-1 and have been convolved with a 30 Hz Ricker wavelet with a focal depth of 2200 m and have been normalized with $|R_{0,0}|_2$ of the relevant reflection series.

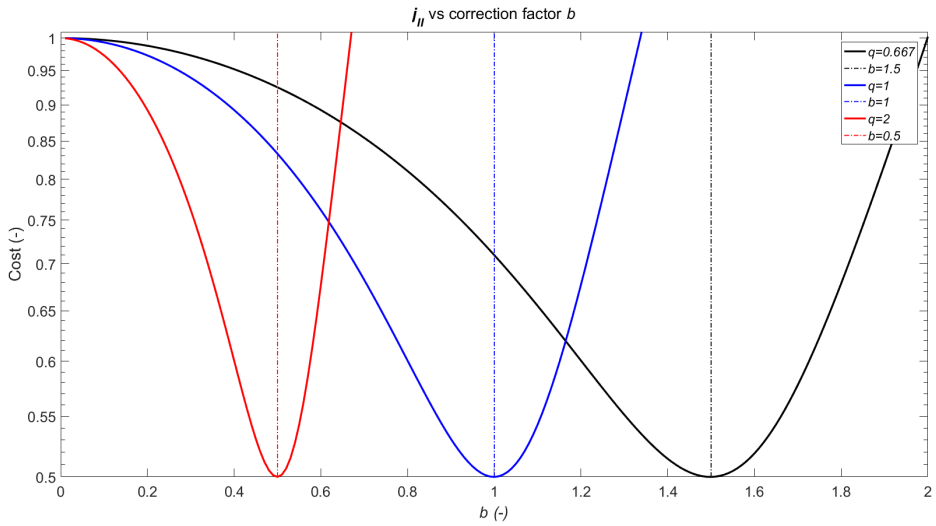

Figure 3-20: Cost function j_{II} using Eq. (2-66) for the weak model in Table A-2 at a focal depth of 2200 meters with a source strength q of (black) $\frac{2}{3}$, (blue) 1 and (red) 2. The location of the correct value of b is indicated by the close-dashed vertical lines. The y-axis is logarithmic.

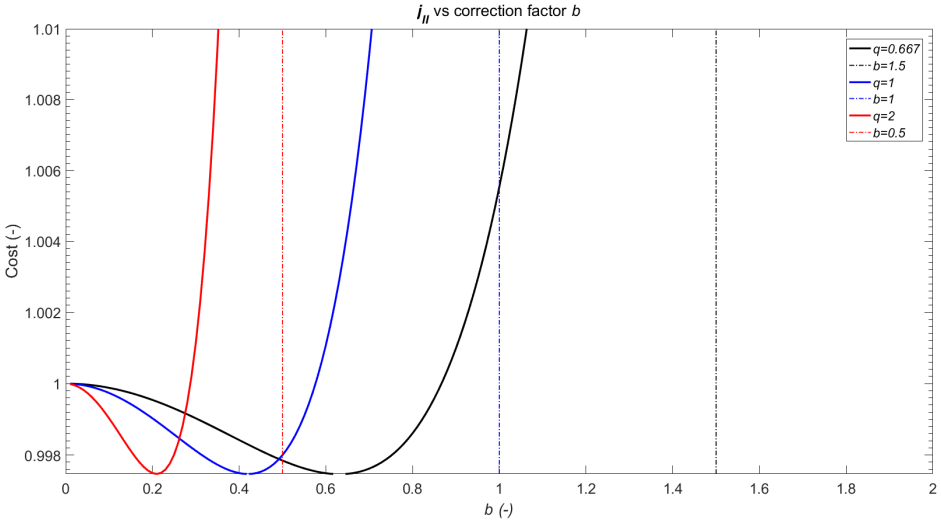

Figure 3-21: Cost function j_{II} using Eq. (2-66) for the artifact model in Table A-3 at a focal depth of 2200 meters with a source strength q of (black) $\frac{2}{3}$, (blue) 1 and (red) 2. The location of the correct value of b is indicated by the close-dashed vertical lines. The y-axis is logarithmic.

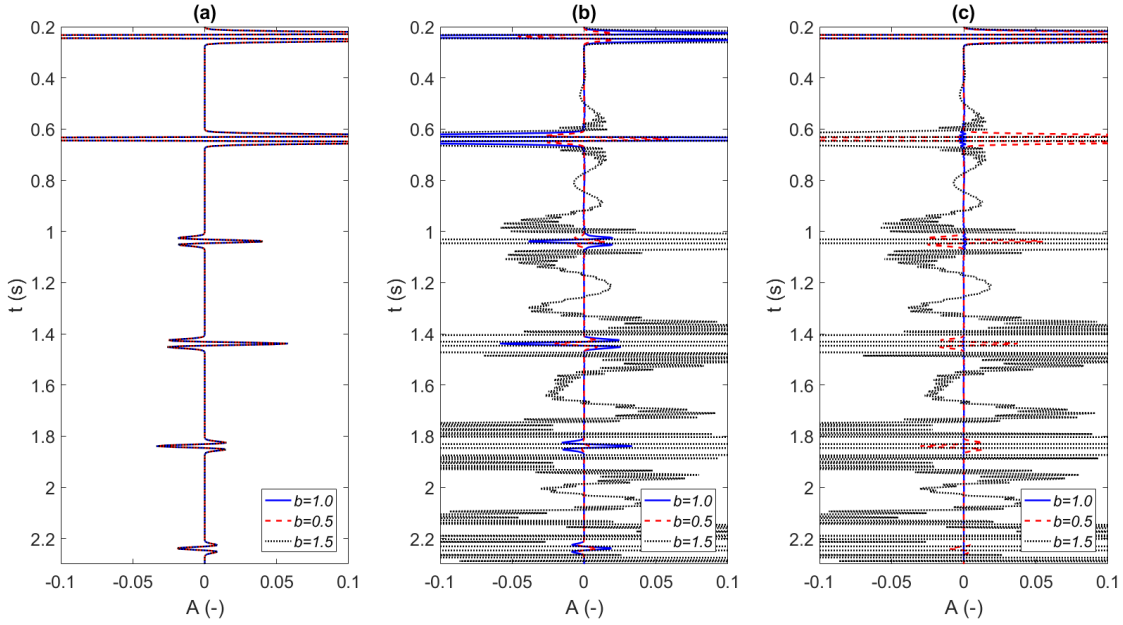

Figure 3-22: (a) Initial estimation of the truncated reflection series, (b) updates of the truncated reflection series and (c) final truncated reflection series after 8 iterations for a correction factor b of (solid blue) 1, (dashed red) 0.5 and (dotted black) 1.5. All events are based on the model found inTable A-3 and have been convolved with a 30 Hz Ricker wavelet with a focal depth of 2200 m and have been normalized with $|R_{0,0}|_2$ of the relevant reflection series.

for b can be recovered if the focal point is below the deepest reflector. This is the ideal case that works for all three of the models. The energy of the physical response $G^{-,+}$ that is used minimizes in a similar way as the energy of the upgoing Green's function that was used for the first cost function. The difference is that in this case the source is also redatumed to the focal depth. This response is shown in Figure 3-26, where the blue line indicates that the correct value of b was applied which results in the correct trace with no events. In case the source strength is underestimated, the updates do not remove enough energy. In case the source strength is overestimated, too much energy is removed as indicated by the dashed red line and dotted black line, respectively. In these figures the event contains a single wavelet and not two wavelets convolved with each other. For these plots, the wavelet was deconvolved once to make the events more clearly separated. This is a purely cosmetic reason and does not seem to change the results of the cost function.

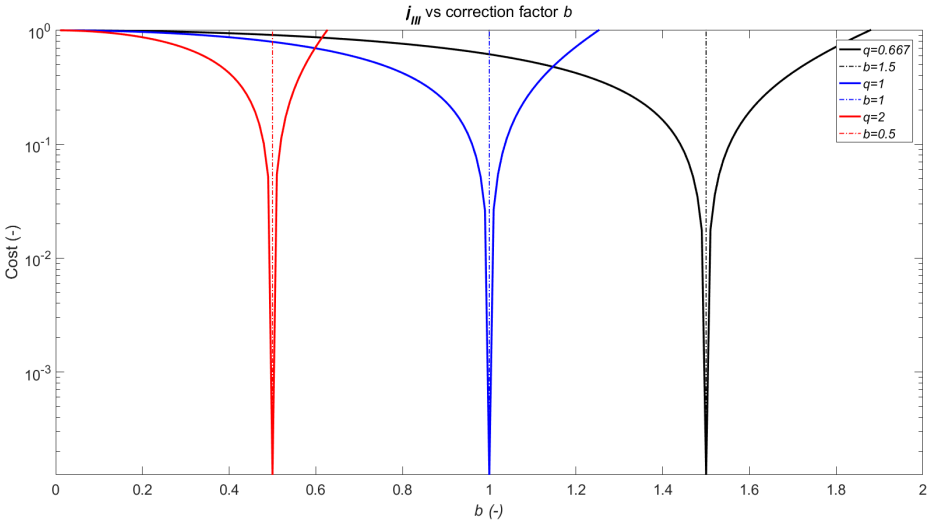

Figure 3-23: Cost function j_{III} using Eq. (2-75) for the simple model in Table A-1 at a focal depth of 2700 meters with a source strength q of (black) $\frac{2}{3}$, (blue) 1 and (red) 2. The location of the correct value of b is indicated by the close-dashed vertical lines. The y-axis is logarithmic.

In case the focal point is moved above the deepest reflector, the results are different. For the simple model as shown in Figure 3-27 the minima are once again smooth and less pronounced. However, their locations are not exactly correct. In each case the correction factor b is underestimated. It is a very small difference of 0.01 in all of these cases. To see if this has any significant influence, this correction factor is tested. In Figure 3-28 (a) the Green's function for the simple model in Table A-1 is plotted for the correct reflection response. In Figure 3-28 (b) the same Green's function is plotted but the reflection series was given an incorrect source strength of $q = 2$. The correction factor of $b = 0.49$ that was recovered in Figure 3-27 was used to compensate for this. When looking at these Green's functions, there is no visible difference. In Figure 3-28 (c) the difference between these two functions is shown which reveals that there are some amplitude differences. These differences are several orders of magnitude lower than the actual amplitude of the events and only a single very weak artifact is introduced. This very weak difference shows that the recovered correction factors are within the range of accuracy that is desired. However this is still a consistent problem with this model

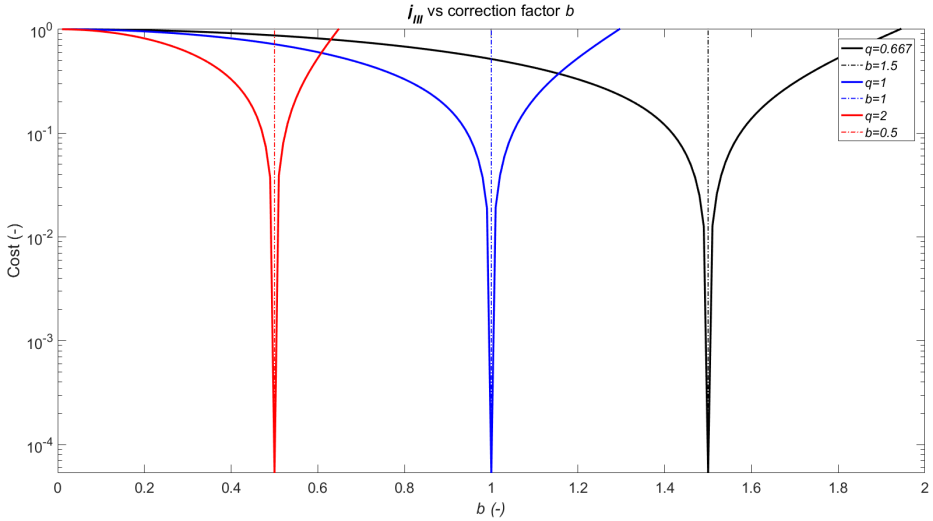

Figure 3-24: Cost function j_{III} using Eq. (2-75) for the weak model in Table A-2 at a focal depth of 2700 meters with a source strength q of (black) $\frac{2}{3}$, (blue) 1 and (red) 2. The location of the correct value of b is indicated by the close-dashed vertical lines. The y-axis is logarithmic.

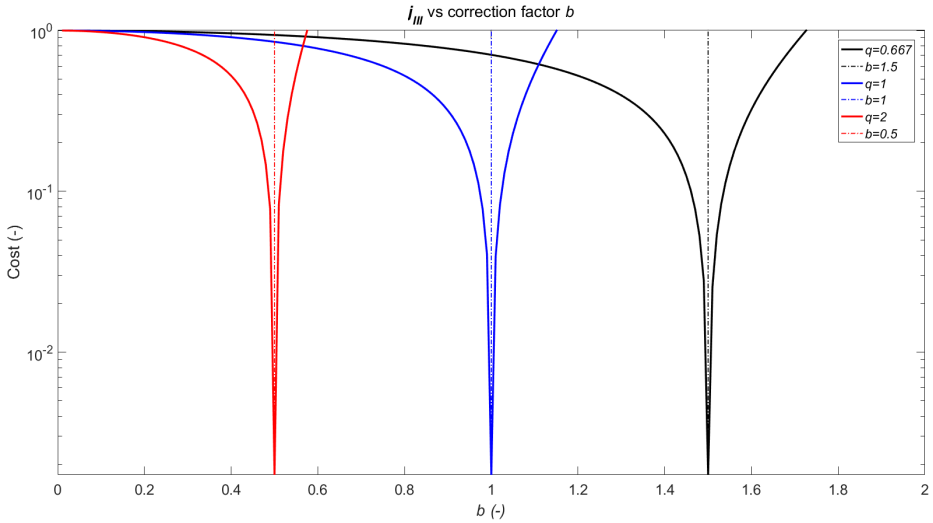

Figure 3-25: Cost function j_{III} using Eq. (2-75) for the artifact model in Table A-3 at a focal depth of 2700 meters with a source strength q of (black) $\frac{2}{3}$, (blue) 1 and (red) 2. The location of the correct value of b is indicated by the close-dashed vertical lines. The y-axis is logarithmic.

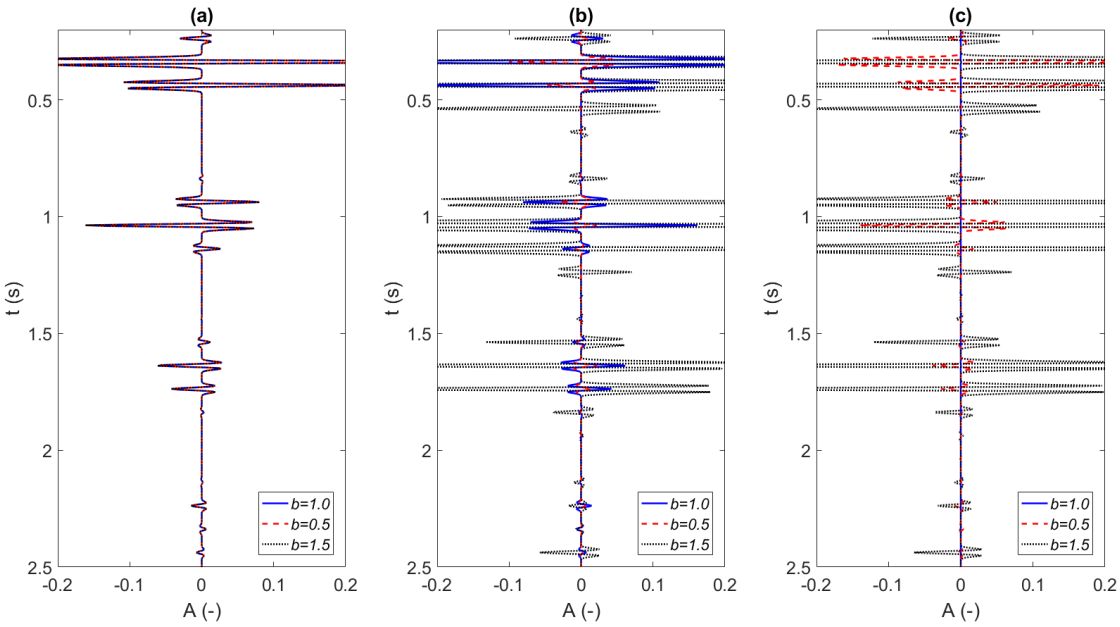

Figure 3-26: (a) Initial estimation of the physical response, (b) updates of the physical response and (c) final physical response after 8 iterations for a correction factor b of (solid blue) 1, (dashed red) 0.5 and (dotted black) 1.5. All events are based on the model found inTable A-1 and have been convolved with a 30 Hz Ricker wavelet with a focal depth of 2700 m and have been normalized with $|G_0^{-,+}|_2$ of the relevant reflection series.

and other models like it. This is related to the case of higher-order multiples overlapping with artifacts such as the one shown in Figure 2-8. The third cost function is still operating in the physical medium, unlike the second cost function that operated in a medium with a reflection-free half-space above the focal depth. The second cost function avoids problems of overlapping events completely, while the third cost function is still affected by some of these events. These higher-order multiples do have very low amplitudes compared to lower-order multiples so their effect is limited in significance. In Figure 3-29 the construction of the physical response is shown. The initial estimation of the physical response contains several events but not all events that have updates are removed, such as the event at $1.4s$ which is enhanced rather than suppressed. This error is due to the overlap of multiple events with artifacts. The other problems that j_I had is completely removed, because for the third cost function the events in Figure 2-7 both need to be removed. So the updates in case of incorrect scaling can no longer suppress the event more than in case the updates are computed using the correct value of b. In case of the weak model, the results are better and acceptable estimates of b are recovered using the cost function, as shown in Figure 3-30. When considering the construction of the physical response as shown in Figure 3-31, the events on the trace are much weaker when compared to the response in Figure 3-29 and some events are not visible because they have very weak amplitudes. Due to this, the events where multiples overlap with artifacts are less significant for the calculation of the cost function. Finally, the artifact model does still cause problems as shown in Figure 3-32. Compared to the results from the previous cost functions in Figure 3-13 and Figure 3-17 the actual results are closer to the correct values of b and are all located at a higher value of b than 0. Still the error is very significant. This

shows that the artifact model cannot be handled by any of the cost functions if the focal point is above the deepest reflector. This shift in the cost function is due to the interaction of the overlapping multiples and artifacts and is highly model-dependent. In Figure 3-33 the physical response construction shows the problem. The events are all overlapping in time causing the comparison between the final and intial estimation to be much smaller and therefore the entire cost function shifts. This is only the case for this specific type of model and can be avoided by locating the focal position below the deepest reflector.

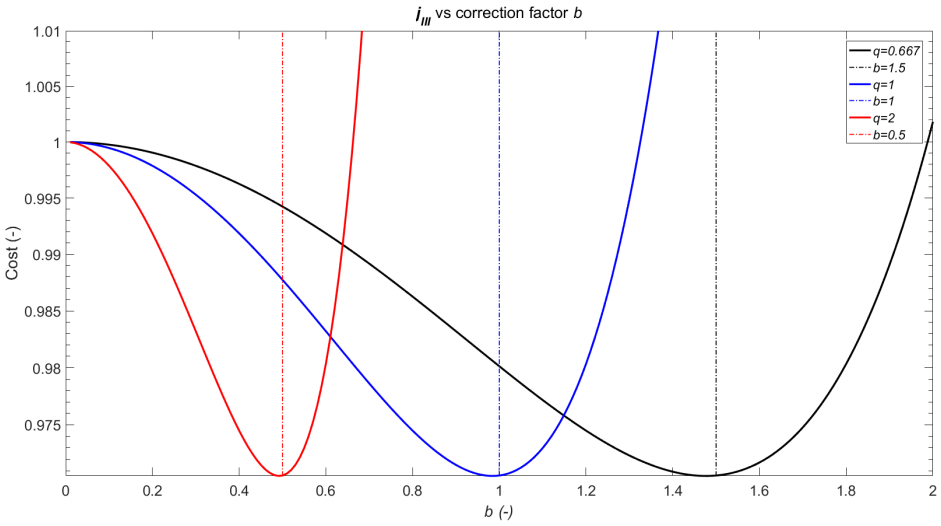

Figure 3-27: Cost function j_{III} using Eq. (2-75) for the simple model in Table A-1 at a focal depth of 2200 meters with a source strength q of (black) $\frac{2}{3}$, (blue) 1 and (red) 2. The location of the correct value of b is indicated by the close-dashed vertical lines. The y-axis is logarithmic.

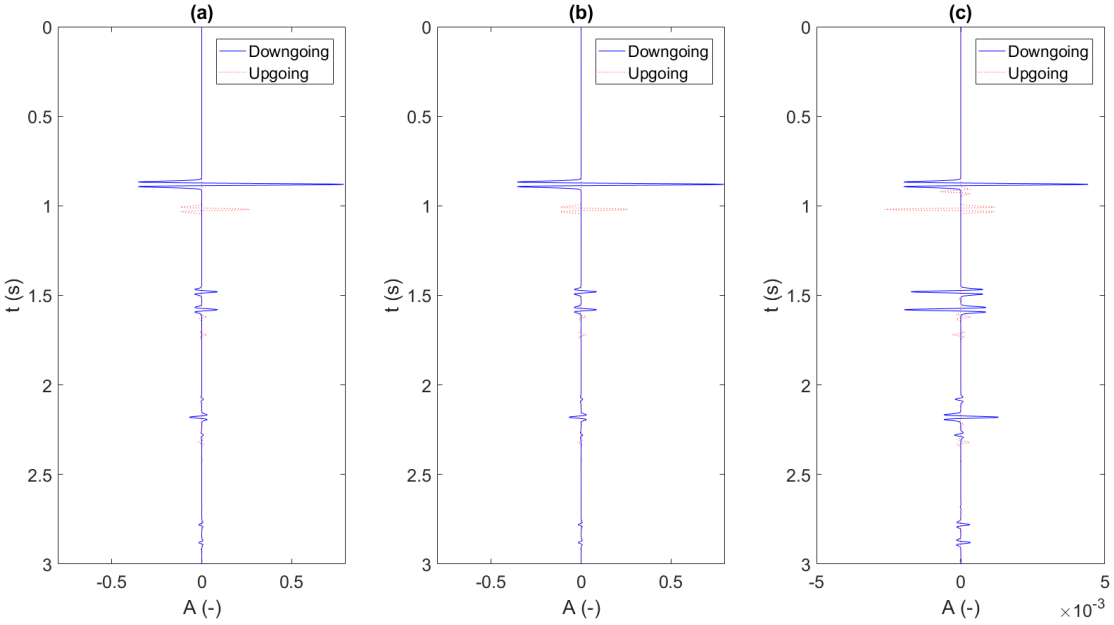

Figure 3-28: (a) Green's functions using the correct source strength of $q = 1$ and correction factor $b = 1$, (b) Green's functions using the incorrect source strength of $q = 2$ and correction factor $b = 0.49$ and (c) difference between the events in (b) and (a). All events are based on the model found inTable A-1 and have been convolved with a 30 Hz Ricker wavelet with a focal depth of 2200 m . Notice that the amplitudes of (c) are much weaker than the events in (a) and (b)

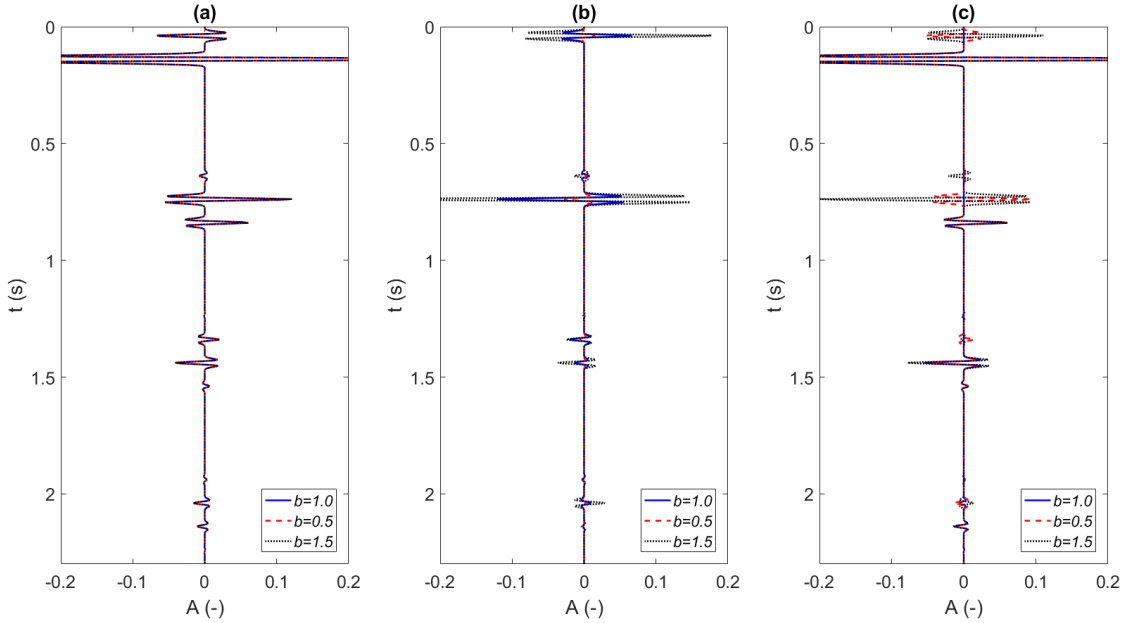

Figure 3-29: (a) Initial estimation of the physical response, (b) updates of the physical response and (c) final physical response after 8 iterations for a correction factor b of (solid blue) 1, (dashed red) 0.5 and (dotted black) 1.5. All events are based on the model found inTable A-1 and have been convolved with a 30 Hz Ricker wavelet with a focal depth of 2200 m and have been normalized with $|G_0^{-,+}|_2$ of the relevant reflection series.

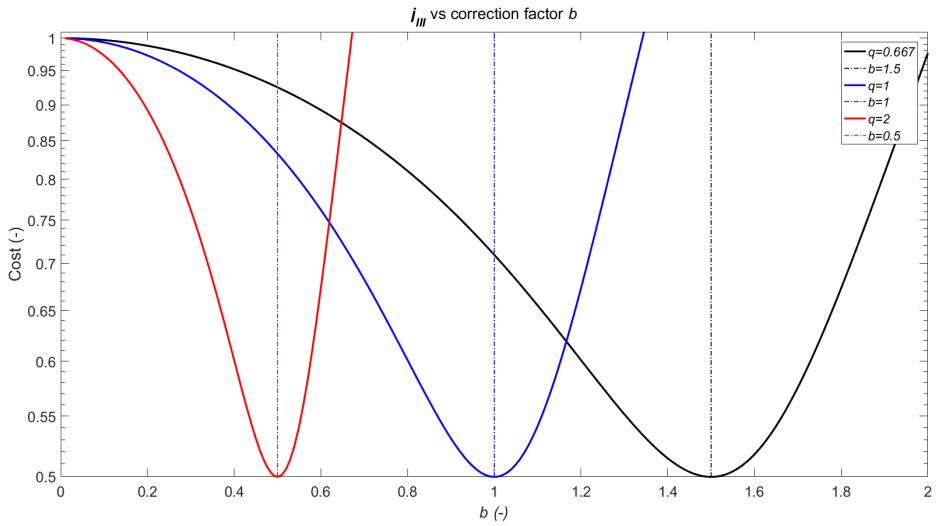

Figure 3-30: Cost function j_{III} using Eq. (2-75) for the weak model in Table A-2 at a focal depth of 2200 meters with a source strength q of (black) $\frac{2}{3}$, (blue) 1 and (red) 2. The location of the correct value of b is indicated by the close-dashed vertical lines. The y-axis is logarithmic.

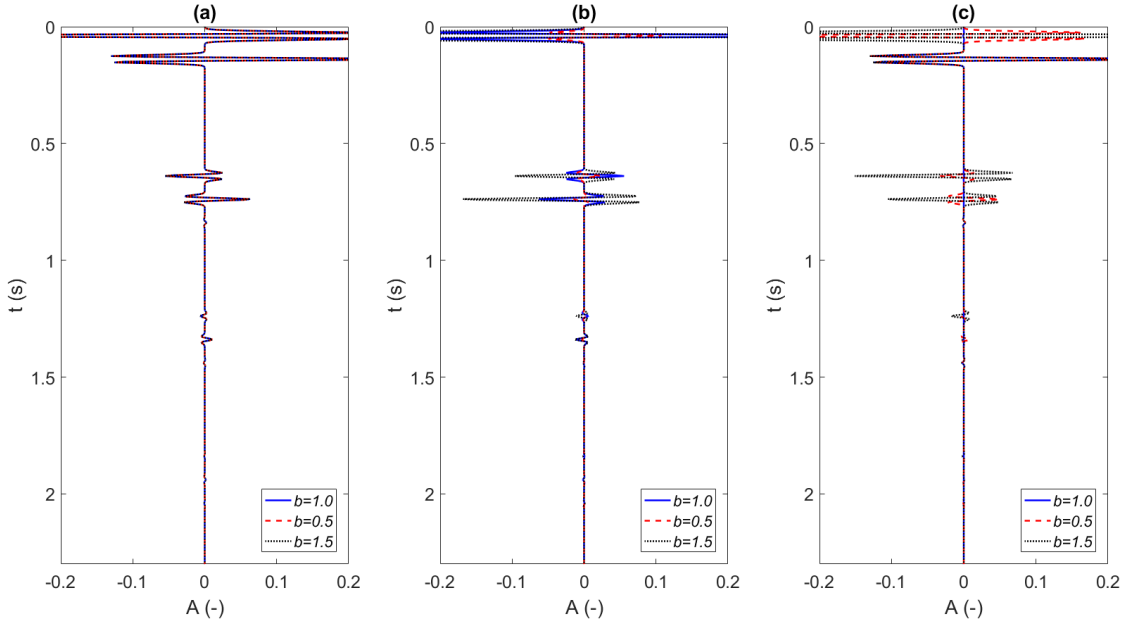

Figure 3-31: (a) Initial estimation of the physical response, (b) updates of the physical response and (c) final physical response after 8 iterations for a correction factor b of (solid blue) 1, (dashed red) 0.5 and (dotted black) 1.5. All events are based on the model found inTable A-2 and have been convolved with a 30 Hz Ricker wavelet with a focal depth of 2200 m and have been normalized with $|G_0^{-,+}|_2$ of the relevant reflection series.

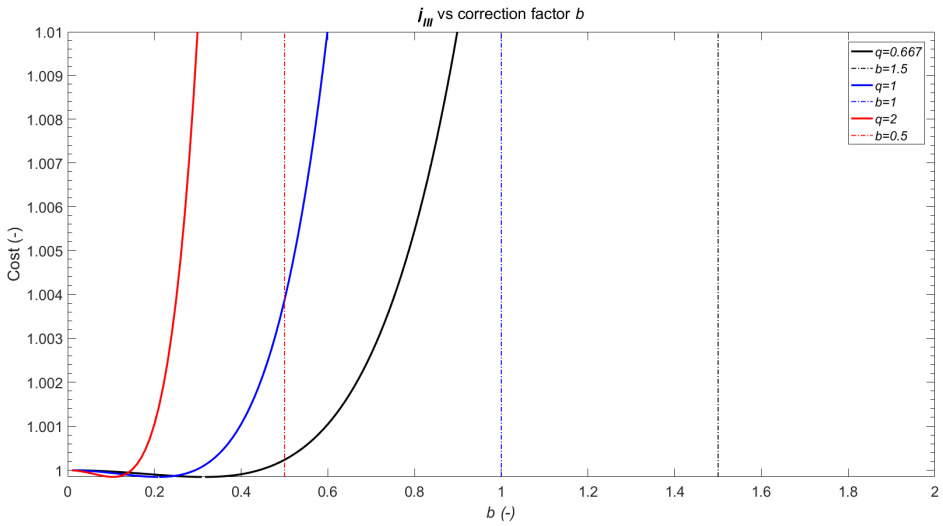

Figure 3-32: Cost function j_{III} using Eq. (2-75) for the artifact model in Table A-3 at a focal depth of 2200 meters with a source strength q of (black) $\frac{2}{3}$, (blue) 1 and (red) 2. The location of the correct value of b is indicated by the close-dashed vertical lines. The y-axis is logarithmic.

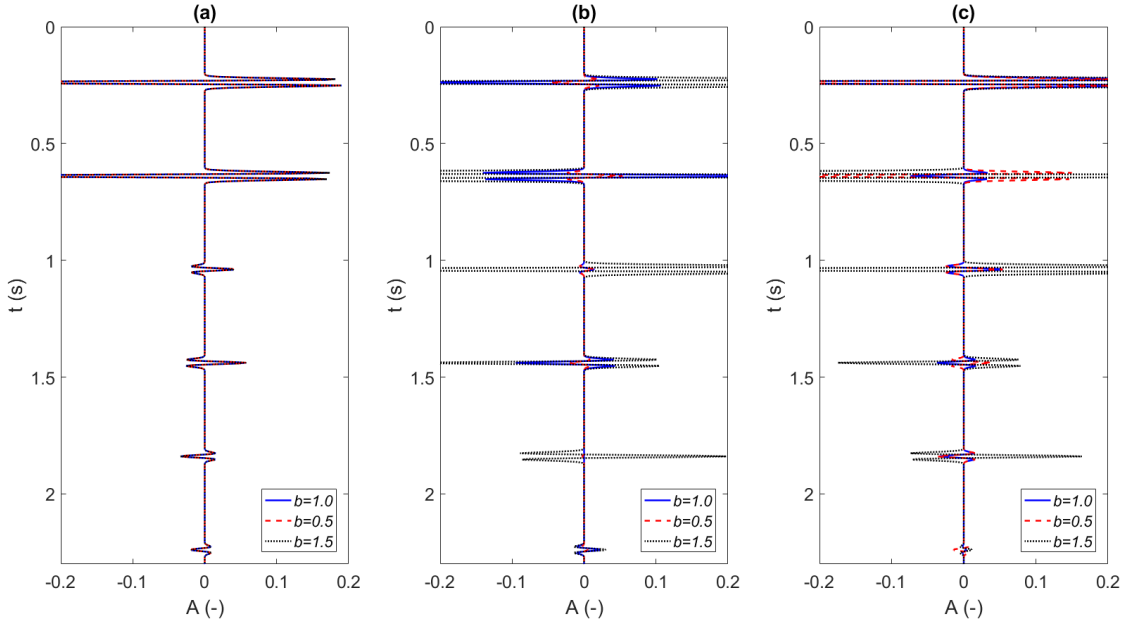

Figure 3-33: (a) Initial estimation of the physical response, (b) updates of the physical response and (c) final physical response after 8 iterations for a correction factor b of (solid blue) 1, (dashed red) 0.5 and (dotted black) 1.5. All events are based on the model found inTable A-3 and have been convolved with a 30 Hz Ricker wavelet with a focal depth of 2200 m and have been normalized with $|G_0^{-,+}|_2$ of the relevant reflection series.

Chapter 4

Conclusion and Discussion

It has been shown how the iterative Marchenko scheme can be derived, which allows for the retrieval of Green's functions at a focal point in the subsurface, as if there was a receiver at that focal point. A reflection response at the surface and an estimation of the first arrival at the focal point are required for this method. It has also been shown how the Marchenko scheme can be used to derive several cost functions. These cost functions are able to retrieve a correction factor b which can correct a reflection response that has been scaled with an unknown source strength q. Along with the correction factor b, a scaling factor $a(\mathbf{x}'_f, b)$ can be retrieved, which corrects the amplitudes of the retrieved Green's functions. The three cost functions were first derived in 1D. The first cost function j_I is based on the minimization of the upgoing Green's function. The first estimate of the upgoing Green's function contains all the physical events and artifacts. Subsequent updates remove the artifacts leading to an upgoing Green's function which contains less events and therefore less energy. The first cost function only retrieves the correct value of b if the focal point is located below the deepest reflector. If the focal point is above the deepest reflector, physical events and artifacts can overlap in time and create problems, affecting the minimization of the first cost function. The second cost function j_{II} is introduced because of this. It minimizes a truncated and redatumed reflection response that operates in a medium that contains no reflectors above the focal point. Both the source and receiver are redatumed to the focal position. j_{II} works well above and below the deepest reflector. This cost function is computationally expensive to implement however, especially in 2D and 3D. The more efficient third cost function j_{III} was therefore introduced. Just like j_{II}, the third cost function redatums the source and receiver to the focal point. Unlike j_{II}, j_{III} operates in the physical medium which contains all the reflectors above the focal point. Once again the upgoing Green's function is minimized. Because of the double-sided redatuming, which is applied to compute j_{III}, the problems with the overlap of physical events and artifacts are greatly reduced, but not completely removed. While the estimates of b are not exactly correct, the approximation of the values is very close. A lot of problems that j_I has are suppressed in j_{III} and the implementation is much more computationally efficient compared to j_{II}. All of these results have been shown on a variety of models in 1D. In 1D, the capabilities of all the cost functions have been shown and it has been concluded that the cost function j_{II} is the superior one of the three. It can handle reflectors above and below the

focal point. The one scenario where it fails is when physical events are overlapping in time with each other. Although this is a serious problem when applying these cost functions in practice, it is assumed to be an acceptable limitation. This limitation is also embedded in a variety of external multiple-elimination schemes that have been proven to work on field data. Two of the three cost functions have been extended to 2D and 3D. In order to distinguish the dimensionality of the cost functions a lowercase j was used for the 1D cost function and an uppercase J for 2D and 3D cost functions. The first cost function J_I is again very straightforward to derive but suffers from the same problems in 2D and 3D as in 1D. The third cost function J_{III} is more difficult to implement in 2D and 3D than in 1D, but it is still a much more efficient function than the extension of j_{II} would be. Again it is an improvement over J_I, however it also can still suffer from overlapping events. Because of the more complex nature of the 2D and 3D models, it is expected that there is less potential overlap of physical events with other physical events and with artifacts. Potentially the methods could yield better results because of this. However, there are also various effects in 2D and 3D that do not play a role in 1D. In the current implementation in 2D and 3D, the assumption is made that $a(\mathbf{x}'_f, b)$ is a scalar and angle-independent. In practice this assumption might not suffice and the accuracy of this assumption should be tested on 2D and 3D data.
The main problem when applying the cost functions to real data is the fact that there are always reflectors below the focal point. In practical cases where the methodology could be applied (for example, complex overburdens or salt bodies), it is not uncommon for the reflectors below the focal point to be much weaker than those located in the overburden. It has been shown that in such a case the approximation of b yields a more accurate estimation. In theory, b is not dependent on the location of the focal point in the subsurface. However in practice the effective value of b is likely to be depth-dependent due to attenuation, incorrect processing of amplitudes and other factors that are not accounted for by the current theory. The severity of these effects can vary, so determing b at every depth is not always necessary. The best practice would be to determine b at several depths and use interpolation to determine b at the depths in between. If b varies strongly then finer sampling of b is necessary. Unlike b, $a(\mathbf{x}'_f, b)$ is always dependent on the location in the subsurface, so this factor has to be determined at every individual focal point in theory too. The scaling factor $a(\mathbf{x}'_f, b)$ is difficult to retrieve when the focal point is located near a layer contrast, which can be overcome by using a shift in the time gate that is used in the Marchenko scheme. Furthermore, just like $a(\mathbf{x}'_f, b)$, b is assumed to be a scalar. If the source signature of the field data is not completely known, b has to be extended to take multiple parameters into account, instead of the single parameter that is considered in this thesis. If more parameters need to be estimated, the computation is more extensive. Also if only approximations of the parameters can be retrieved, this may lead to deterioration, rather than improvement, of the reflection response. As such the study in this thesis should be considered to be a first attempt to apply such corrections. Sufficient care should be taken into account when these methods are applied in practice. The validity of the derived cost functions has been proven. These cost functions could be expanded upon to make the implementation of the Marchenko method to real data easier and more effective in the future. It would be best to derive a cost function that similarly to j_{II} can handle reflectors below the focal point, but is more efficient to apply in 2D and 3D. Perhaps not a single function could be minimized, but two or more to get a more solid base for determining the value of b.

Bibliography

Amundsen, L. (2001). Elimination of free-surface related multiples without need of the source wavelet. *Geophysics*, 66(1):327–341.

Amundsen, L. and Robertsson, J. O. (2014). Wave equation processing using finite-difference propagators, part 1: Wavefield dissection and imaging of marine multicomponent seismic data. *Geophysics*, 79(6):T287–T300.

Berkhout, A. and Verschuur, D. (2005). Removal of internal multiples with the common-focus-point (cfp) approach: Part 1 explanation of the theory. *Geophysics*, 70(3):V45–V60.

Broggini, F. and Snieder, R. (2012). Connection of scattering principles: A visual and mathematical tour. *European Journal of Physics*, 33(3):593.

Fleury, C. (2012). *Wave propagation in complex media, scattering theory, and application to seismic imaging*. Colorado School of Mines.

Liu, Y., van der Neut, J., Arntsen, B., and Wapenaar, K. (2016). Combination of surface and borehole seismic data for robust target-oriented imaging. *Geophysical Journal International*, 205(2):758–775.

McMechan, G. (1983). Migration by extrapolation of time-dependent boundary values. *Geophysical Prospecting*, 31(3):413–420.

Oristaglio, M. L. (1989). An inverse scattering formula that uses all the data. *Inverse Problems*, 5(6):1097.

Singh, S., Snieder, R., Behura, J., van der Neut, J., Wapenaar, K., and Slob, E. (2015). Marchenko imaging: Imaging with primaries, internal multiples, and free-surface multiples. *Geophysics*, 80(5):S165–S174.

Stakgold, I. and Holst, M. J. (2011). *Green's functions and boundary value problems*, volume 99. John Wiley & Sons.

van Borselen, R., Fookes, G., and Brittan, J. (2003). Target-oriented adaptive subtraction in data-driven multiple removal. *The Leading Edge*, 22(4):340–343.

van der Neut, J., Vasconcelos, I., and Wapenaar, K. (2015a). On green's function retrieval by iterative substitution of the coupled marchenko equations. *Geophysical Journal International*, 203(2):792–813.

van der Neut, J., Wapenaar, K., Thorbecke, J., Slob, E., et al. (2015b). Practical challenges in adaptive marchenko imaging. In *2015 SEG Annual Meeting*. Society of Exploration Geophysicists.

Verschuur, D. and Berkhout, A. (1997). Estimation of multiple scattering by iterative inversion, part ii: Practical aspects and examples. *Geophysics*, 62(5):1596–1611.

Verschuur, D. J., Berkhout, A., and Wapenaar, C. (1992). Adaptive surface-related multiple elimination. *Geophysics*, 57(9):1166–1177.

Wapenaar, C. and Grimbergen, J. (1996). Reciprocity theorems for one-way wavefields. *Geophysical Journal International*, 127(1):169–177.

Wapenaar, K. and Fokkema, J. (2006). Green's function representations for seismic interferometry. *Geophysics*, 71(4):SI33–SI46.

Wapenaar, K., Thorbecke, J., and van der Neut, J. (2016). A single-sided homogeneous green's function representation for holographic imaging, inverse scattering, time-reversal acoustics and interferometric green's function retrieval. *Geophysical Journal International*, 205(1):531–535.

Wapenaar, K., Thorbecke, J., van der Neut, J., Broggini, F., Slob, E., and Snieder, R. (2014a). Green's function retrieval from reflection data, in absence of a receiver at the virtual source position. *The Journal of the Acoustical Society of America*, 135(5):2847–2861.

Wapenaar, K., Thorbecke, J., Van Der Neut, J., Broggini, F., Slob, E., and Snieder, R. (2014b). Marchenko imaging. *Geophysics*, 79(3):WA39–WA57.

Yilmaz, Ö. (2001). *Seismic data analysis*, volume 1. Society of exploration geophysicists Tulsa.

Zhan, G., Dai, W., Zhou, M., Luo, Y., and Schuster, G. T. (2014). Generalized diffraction-stack migration and filtering of coherent noise. *Geophysical Prospecting*, 62(3):427–442.

Appendix A

Models

$z_{top}(m)$	$z_{bottom}(m)$	c (m/s)	$\rho(kg/m^3)$
0	750	2500	1000
750	1500	2500	2000
1500	2375	2500	1000
2375	3000	2500	2000

Table A-1: Velocity and density distribution for the simple model

$z_{top}(m)$	$z_{bottom}(m)$	c (m/s)	$\rho(kg/m^3)$
0	750	2500	1000
750	1500	2500	2000
1500	2375	2500	1000
2375	3000	2500	1050

Table A-2: Velocity and density distribution for the weak model

$z_{top}(m)$	$z_{bottom}(m)$	c (m/s)	$\rho(kg/m^3)$
0	1000	2500	1000
1000	1500	2500	2000
1500	2000	2500	1000
2000	2500	2500	2000
2500	3000	2500	1000

Table A-3: Velocity and density distribution for the artifact model